UNIVERSIDADE FEDERAL DO CEARÁ
CENTRO DE TECNOLOGIA
DEPARTAMENTO DE ENGENHARIA METALÚRGICA E DE MATERIAIS
PROGRAMA DE PÓS-GRADUAÇÃO EM ENGENHARIA E CIÊNCIA DE MATERIAIS

MAURÍCIO DE SOUSA PEREIRA

APPLICATION OF OXIDE NANOPARTICLES OBTAINED BY PROTEIC SOL-GEL AND MECHANICAL ALLOYING IN THIRD GENERATION SOLAR CELLS

FORTALEZA

2017

MAURÍCIO DE SOUSA PEREIRA

APPLICATION OF OXIDE NANOPARTICLES OBTAINED BY PROTEIC SOL-GEL AND MECHANICAL ALLOYING IN THIRD GENERATION SOLAR CELLS

Doctoral Thesis submitted to the Graduate Program in Materials Science and Engineering of the Federal University of Ceará in partial fulfillment of the requirements for the degree of Doctor in Materials Science and Engineering. Concentration area: Physical and Mechanical Properties of Materials.

Advisor: Prof. Dr. Igor Frota de Vasconcelos

FORTALEZA

2017

Dados Internacionais de Catalogação na Publicação
Universidade Federal do Ceará
Biblioteca Universitária
Gerada automaticamente pelo módulo Catalog, mediante os dados fornecidos pelo(a) autor(a)

P493a

Pereira, Maurício de Sousa.
Application of oxide nanoparticles obtained by proteic sol-gel and mechanical alloying in third generation solar cells / Maurício de Sousa Pereira. – 2017.
130 f.: il. color.

Tese(doutorado) - Universidade Federal do Ceará, Centro de Tecnologia, Programa de Pós-Graduação em Engenharia e Ciência de Materiais, Fortaleza, 2017.
Orientação: Prof. Dr. Igor Frota de Vasconcelos

1. Células Solares Sensibilizadas por Corantes. 2. Células solares orgânicas. 3. P3HT:PCBM. 4. Eficiência. 5. Estabilidade. I. Título.

CDD 620.11

MAURÍCIO DE SOUSA PEREIRA

APPLICATION OF OXIDE NANOPARTICLES OBTAINED BY PROTEIC SOL-GEL AND MECHANICAL ALLOYING IN THIRD GENERATION SOLAR CELLS

Doctoral Thesis submitted to the Graduate Program in Materials Science and Engineering of the Federal University of Ceará in partial fulfillment of the requirements for the degree of Doctor in Materials Science and Engineering. Concentration area: Physical and Mechanical Properties of Materials.

Approval date: 01/August/2017

THESIS COMMITTEE

Prof. Dr. Igor Frota de Vasconcelos (Advisor)
Universidade Federal do Ceará (UFC)

Prof. Dr. Lucimara Stolz Roman
Universidade Federal do Paraná (UFPR)

Prof. Dr. Alexandre Magno Rodrigues Teixeira
Universidade Regional do Cariri (URCA)

Dr. Francisco Anderson de Sousa Lima
Departamento de Eletrônica Orgânica (CSEM Brasil)

Prof. Dr. Eduardo Bedê Barros
Universidade Federal do Ceará (UFC)

To my wife Silvana for her unconditional help,

to my daughter Anah Sophie,

to my mother for her encouragement

and to my father (in memoriam).

ACKNOWLEDGEMENTS

I am extremely grateful to Prof. Igor Frota de Vasconcelos (my advisor) for his generosity in giving me so many opportunities to learn, apply new knowledge and to participate in many new projects. Also by always willing to discuss new ideas and results and for trusting me by giving me autonomy and responsibilities which helped me develop new skills that are being very useful in my career.

I would like to express my very deep gratitude to my friend Francisco Anderson de Sousa Lima who have helped me during this journey.

I would like to express my very deep gratitude to ICN2 on behalf of the Dr. Monica Lira-Cantu for allowing me to use its impressive infrastructure to develop part this study and for the logistical support offered in Barcelona.

I would like to thank to Prof. Eduardo Bedê Barros and to PhD student Rodrigo Q. Almeida from the Physics Department for the valuable collaboration and by the AFM analysis.

I would like to thank to Prof. Paulo de Tarso Cavalcante Freire and to PhD student Cristino B. Silva from the Physics Department for the valuable collaboration and by FTIR analysis.

I would like to thank to Prof. Manoel Ribeiro da Silva of Universidade Federal de Itajubá and Prof. André Avelino Pasa of Universidade Federal de Santa Catarina for their valuable collaboration in providing the magnetic measurements.

I would like to thank CSEM Brasil on behalf of the Dr. Diego Bagnis for the infrastructure used to develop part this study.

I would like to thank Central Analítica of UFC for their valuable collaboration in the SEM analysis and in the availability for the use of its equipment.

I would like to thank the members of the committee Prof. Lucimara Stolz Roman,

Prof. Alexandre Magno Rodrigues Teixeira, Dr. Francisco Anderson de Sousa Lima, and Prof. Eduardo Bedê Barros for their valuable time.

I also would like to thank to my friends who have helped me during this journey. Thiago S. Ribeiro, Francisco Iran S. Lima, Gilvane Sampaio, Luís Paulo Santos and Kleyton J. Camelo of the Graduate Program in Materials Science and Engineering are very much appreciated for their help and support and for the very interesting discussions.

I would like to thank CNPq and FUNCAP for the financial support, without which I would not have been able to finish this work. I also would like to thank UFC and the Graduate Program in Materials Science and Engineering for the opportunity to pursue a doctorate degree.

ABSTRACT

The development of new energy technologies is crucial to climate stability and security in the planet. Considering the current energy consumption on a global scale it becomes evident the need to develop new alternative energy sources, especially those that are preferentially renewable, clean and economical. Among the renewable energy sources currently used, solar energy is an attractive source because it is abundant and free of CO_2. Photovoltaic solar cells are just one of several ways to harness solar energy, converting it directly into electricity. Currently, traditional solar technologies have been used to a limited degree in energy production because of the high costs. However, third-generation solar cells offer a potential route for large-scale solar energy deployment because they utilize materials that are abundant in nature and low cost production technologies. Commonly called excitonic solar cells, third generation photovoltaic devices encompass a wide variety of solar cells such as dye-sensitized solar cells and organic solar cells. Both offer a technically and economically reliable alternative to the current concept of photovoltaic devices based on p-n junctions. In this doctoral thesis, nanoparticles of semiconductor oxides and spinel ferrites produced by protein sol-gel and mechanical alloying were applied to dye-sensitized and organic solar cells in order to improve their efficiency and stability. Prior to their application, the nanoparticles had their thermal, structural, optical and magnetic properties characterized. Solar cells efficiency was evaluated by electrical characterization methods such as current–voltage curves and external quantum efficiency measurements, and their stability, when applicable, was studied by accelerated and real outdoor degradation tests. Nanoparticles of semiconductor SnO_2 produced by the proteic sol-gel method were successfully applied as photoanodes in dye-sensitized solar cells. The results confirmed the formation of spherical nanoparticles of rutile SnO_2 with an optical absorption band in the ultraviolet region near the visible light range. The performance of the cells was found to be in line with results in the literature. Moreover, nanoparticles of Fe-doped SnO_2 diluted magnetic seminconductor and $CoFe_2O_4$ spinel ferrite produced by mechanical alloying and proteic sol-gel, respectively, were applied as dopants in the active layer of organic solar cells. An improvement on photovoltaic parameters that may lead to better cell efficiency and stability was observed for devices with doped active layers. The results are indications that the addition of magnetic oxide nanoparticles in the active layer of organic solar cells has the potential to contribute to the extension of lifetime and improvement of efficiency and stability of these devices.

Keywords: Dye-Sensitized Solar Cells, Organic solar cells, P3HT:PCBM, Efficiency, Stability.

RESUMO

O desenvolvimento de novas tecnologias energéticas é crucial para a estabilidade do clima e segurança do planeta. Considerando o consumo energético atual em escala global torna-se evidente a necessidade do desenvolvimento de novas fontes alternativas de energia, especialmente aquelas que são preferencialmente renováveis, limpas e econômicas. Entre as fontes de energias renováveis usadas atualmente, a energia solar é uma fonte atraente pois é abundante e livre de CO_2. Células solares fotovoltaicas são uma das várias maneiras de aproveitar a energia solar, convertendo-a diretamente em eletricidade. Atualmente, as tecnologias solares tradicionais têm sido utilizadas num grau limitado na produção de energia devido aos custos elevados. Todavia, as células solares de terceira geração oferecem uma rota potencial para implantação de energia solar em larga escala, pois utilizam materiais abundantes na natureza e tecnologias de produção de baixo custo. Comumente denominadas células solares excitônicas, dispositivos fotovoltaicos de terceira geração englobam uma grande variedade de células solares tais como células solares sensibilizadas por corante e células solares orgânicas. Ambas apresentam uma alternativa técnica e economicamente confiável ao conceito atual de dispositivos fotovoltaicos baseados em junção p-n. Nesta tese de doutorado, nanoparticulas de óxidos semicondutores e ferritas com estrutura espinélio produzidos por sol-gel proteico e moagem mecânica foram aplicadas em células solares sensibilzadas por corante e orgânicas com o intuito de melhorar sua eficiência e estabilidade. Antes da sua aplicação, as nanopartículas tiveram suas propriedades térmicas, estruturais, ópticas e magnéticas caracterizadas. A eficiência das células solares foi avaliada por meio de métodos de caracterização elétrica como a curva corrente-voltagem e eficiência quântica externa enquanto sua estabilidade, quando foi o caso, foi estudada por testes de degradação acelerada e em condições ambientais. Nanopartículas de SnO_2 semicondutor produzidas pelo método sol-gel proteico foram usadas com sucesso como fotoanodo em células solares sensibilizadas por corante. Os resultados obtidos confirmaram a formação de nanopartículas esféricas de SnO_2 com estrutura rutílio com banda de absorção óptica na região do ultravioleta próximo da faixa de luz visível. O desempenho das células obtidas foi consistente com a literatura. Além disso, nanopartículas de óxido semicondutor magnético diluído SnO_2 dopado com Fe e ferrita espinélio $CoFe_2O_4$ produzidas por moagem mecânica e sol-gel proteico, respectivamente, foram aplicadas como dopantes na camada ativa de células solares orgânicas. Foi observada uma melhora dos parâmetros fotovoltaicos que pode levar a uma melhor eficiência e estabilidade dos dispositivos com camada ativa dopada. Esses resultados indicam qua a adição de nanopartículas de óxidos magnéticos na camada ativa de células solares orgânicas tem o potencial de contribuir para a extensão do tempo de vida e melhoria da eficiência e estabilidade desses dispositivos.

Palavras-chave: Células Solares Sensibilizadas por Corantes, Células solares orgânicas, P3HT:PCBM, Eficiência, Estabilidade.

LIST OF FIGURES

LIST OF TABLES

LIST OF SYMBOLS AND ABBREVIATIONS

AM	Air mass
AFM	Atomic force microscopy
η_{A}	Absorption efficiency
BHJ	Bulk heterojunction
k_B	Boltzmann constant
V_{bi}	Built-in potential
CO_2	Carbon dioxide
$CoFe_2O_4$	Cobalt ferrite
CdTe	Cadmium teluride
CIGS	Copper indium gallium selenide
CT	Charge transfer
J×V	Curve current voltage
η_{CS}	Charge separation efficiency
η_{CC}	Charge collection efficiency
H_c	Coercive field
C-AFM	Conductive atomic force microscopy
ϵ	Dielectric permittivity
DSSC	Dye sensitized solar cell
DSC	Differential scanning calorimetry
D–A	Donor acceptor interface
L_{D}	Difusion lenght
ETL	Electron transport layer
EQE	External quantum efficiency

XSC	Excitonic solar cell
η_{ED}	Exciton diffusion efficiency
Fe/SnO_2	Ferro doped tin oxide
FTIR	Fourier transformed infrared
FTO	Fluorine doped tin oxide
FF	Fill factor
HOMO	Highest occupied molecular orbital
HTL	Hole transport layer
ICN2	Catalan Institute of Nanoscience and Nanotechnology
ICSD	Inorganic Crystal Structure Database
IPCE	Incident photon-to-current conversion efficiency
ITO/Ag/ITO	Indium-doped tin oxide/silver/indium-doped tin oxide multilayer
ISOS	International summit on OPV stability
ITO	Indium doped tin oxide
LED	Ligth emitted diode
LUMO	Lower unoccupied molecular orbital
MoO_3	Molybdenum oxide
M_r	Remanent magnetization
M_s	Saturation magnetization
P_{max}	Maximum power density
V_{max}	Maximum open circuit voltage
J_{max}	Maximum short circuit current density
MNPs	Magnetic nanoparticles
N719	Di-tetrabutylammonium cis-bis(isothiocyanato)bis(2,2'-bipyridyl-4,4'-dicarboxylato) ruthenium(II)
N3	Cis-Bis(isothiocyanato) bis(2,2'-bipyridyl-4,4'-dicarboxylato ruthenium(II)
NP	Nanoparticles
OLED	Organic ligth emitted diode
O-DMS	Oxide diluted magnetic semiconductors

OPV	Organic photovoltaic
OSCs	Organic solar cell
V_{oc}	Open circuit voltage
ONPs	Oxide nanoparticles
P3HT	Poly(3-hexylthiophene-2,5-diyl) regioregular
PCBM	[6,6]-phenyl-C_{61}-butyric acid methyl ester
PEDOT:PSS	Poly(3,4-ethylenedioxythiophene) polystyrene sulfonate
PET	Polyethylene
PV	Photovoltaics
PL	Photoluminescence
η	Power conversion efficiency
J_{ph}	Photocurrent density
E_{ph}	Photon energy
RTFM	Room temperature ferromagnetism
R2R	Roll-to-roll
SAED	Selected area of electron diffraction
SEM	Scanning electron microscopy
SFNPs	Spinel ferrite nanopaticles
J_0	Saturation current density
R_s	Series resistance
R_{sh}	Shunt resistance
J_{sc}	Short circuit current density
T_{80}	Period of time when device has decayed 20% from initial measurement
TiO_2	Titanium oxide
SnO_2	Tin oxide
TCO	Transparent conductive oxide
TEM	Transmission electron microscopy
TGA	Thermogravimetric analysis
TMO	Transition metal oxide

TM	Transition metal
UV-Vis	Ultraviolet–visible spectroscopy
V_2O_5	Vanadium pentoxide
XRD	X-ray diffraction
ZnO	Zinc oxide

CONTENTS

1. INTRODUCTION AND OBJECTIVES

Third generation solar cells are solution processed solar cells based on semiconducting organic macromolecules, inorganic nanoparticles or hybrids with excellent potential for large-scale solar electricity generation. Usually, they are also called excitonic solar cells (XSC) due to its charge generation mechanism based on to the formation of excitons. These photovoltaic devices encompass a wide variety of solar cells, such as dye-sensitized solar cells (DSSCs) and organic solar cells (OSCs). Recently, DSSCs and OSCs have drawn much attention because they offer a possibility of low cost fabrication (solution based printing) together with other attractive features like flexibility.

DSSCs are unique compared with almost all other kinds of solar cells in that electron transport, light absorption and hole transport are each handled by different materials in the cell. OSCs is a type of photovoltaic that uses organic electronics, a branch of electronics that deals with conductive organic polymers or small organic molecules, for light absorption and charge transport to produce electricity from sunlight by the photovoltaic effect.

Common to most of these devices are their maturity with respect to novel materials and high performance. The attention is also directed to their manufacture, which include some peculiar features such as lightness, flexibility, transparency and ease of production by processing techniques in solution. The organic modules exhibit these characteristics due, in part, to the high coefficient of absorption of the organic semiconductors, which allows the development of devices with layers of only few nanometers of thickness. In addition to the possibility of manufacturing very thin devices, the solubility of the organic molecules in organic solvents enables their processability by low cost techniques such as roll-to-roll or by printing production.

Power conversion efficiency of organic solar cell strongly depends on the phase morphology. The inclusion of small heavy metal nanoparticles (NPs) in the active layer can have an effect on the film morphology, the donor-acceptor intermixing scales, and the degree of crystallinity as well as crystal orientation, which in the end has an impact on the conductivity and therefore on the performance of the final device. Thus, a complex interplay between these factors will make the prediction of a potential positive effect of the efficiency of OSCs very difficult. Moreover, a very large number of different small heavy metal NPs are available and could be added to OSCs.

It has been reported, that there are two possible ways, how doping with oxide nanoparticles (ONPs) improves photovoltaic characteristics: on one hand, is a coercive electric field, due to dipole interactions from ONPs dispersed in bulk heterojunction (BHJ) layer show potential to strengthen the performance of BHJ polymer-fullerene OSCs. On the other hand it is spin-orbit coupling which increases the efficiency of the exciton intersystem crossing process in the device, and thus extends efficient lifetime.

1.1 Objectives

The general objective of this work is to synthesize, characterize, and apply different oxide nanoparticles such as SnO_2, Fe-doped SnO_2 and $CoFe_2O_4$ in dye-sensitized and organic solar cells. This objective can be split into the following specific objectives:

1. Synthesis of oxide nanoparticles by proteic sol-gel and mechanical alloying. These synthesis techniques were selected due to their low-cost with the possibility to be carried out at low temperature;

2. Characterization of the oxide nanoparticles using different characterization techniques, such as thermogravimetric analysis, differential scanning calorimetry, atomic force microscopy, transmission electron microscopy, ultraviolet-visible spectroscopy, X-ray diffraction, Mössbauer spectroscopy, vibrating sample magnetometry and Fourier-transformed infrared spectroscopy;

3. Application of oxide nanoparticles in solar cells. SnO_2 nanoparticles produced by proteic sol-gel were applied as photoanodes in DSSCs while mechanically alloyed Fe-doped SnO_2 and proteic sol-gel $CoFe_2O_4$ nanoparticles were applied as dopants to the active layers of OSCs;

4. Characterization of the cells in terms of their power conversion efficiency and stability. The efficiency was evaluated by electrical characterization methods such as current–voltage curves and external quantum efficiency measurements, and the stability by accelerated or real outdoor degradation tests.

1.2 Outline

This thesis work is organized in the following way:

Chapter 2 reviews the literature in the field of solar cells, with special attention to the third genaration solar cells and to the application of oxides semiconductors as component parts of these devices. This chapter was written in a way to provide the reader with a basic knowledge of the subjects and help achieve a full understanding of the results presented in later chapters.

Chapter 3 presents results and analysis on the structural, morphological and optical properties of SnO_2 nanoparticles obtained by proteic sol-gel method and their application in dye-sensitized solar cells. This was been published in the Journal of Sol-Gel Science and Technology (DOI: 10.1007/s10971-017-4488-7).

Chapter 4 presents results and analysis on the application of mechanically alloyed Fe-doped SnO_2 nanoparticles in organic solar cells with enhanced stability. This chapter was published in Optical Materials 64 (2017) 548-556.

Chapter 5 presents results and analysis on the application of nanostructured $CoFe_2O_4$ as doping of the active layer in OSCs. An article is being prepared for publication.

Conclusions, as well as suggestions for future work, are summarized in chapter 6.

2. THIRD GENERATION SOLAR CELLS

2.1 Global energy landscape

Currently, the patterns of energy production are based on fossil sources (oil, coal, natural gas). The reduction of fossil fuel reserves in the world is a warning for the need to develop alternative energy sources that are preferentially renewable, clean and economical. Interest in these alternative energy sources has increased as a result of rising energy demand and climate change. Several sources of renewable energy are being developed, such as biomass, hydro, wind, geothermal and solar. Among these sources, solar energy is an attractive source as it is abundant and free of CO_2 [1, 2]. Figure 2.1 shows the energy consumption of different sources in global scale reported by International Energy Agency in 2016 [3].

Figure 2.1: Energy consumption from different sources in global scale. *Other* – includes geothermal, solar, wind, heat, etc.

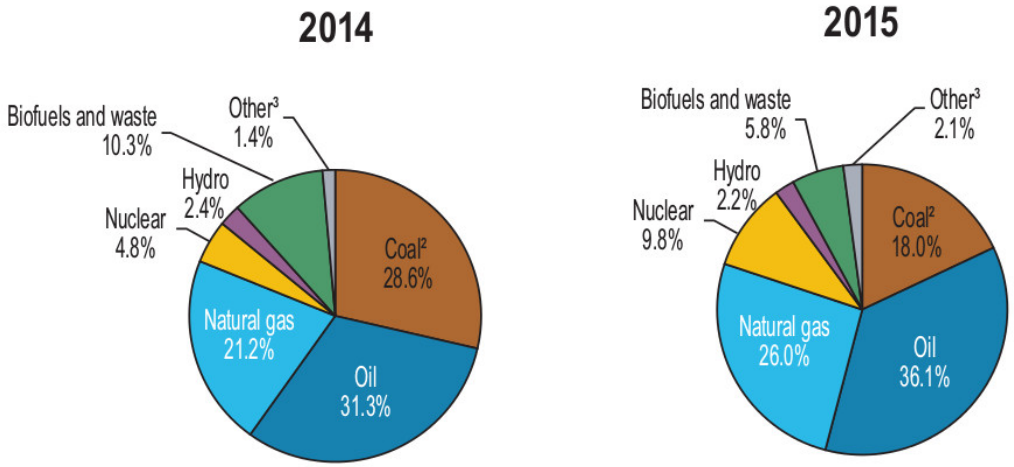

Source: International Energy Agency [3].

Nanotechnology has implemented substantial advances in an attempt to attenuate the energy crisis. In this sense, some parameters have been taken into account in the attempt to introduce new technologies based on the conversion of solar energy. Such parameters include: development of new materials, low cost of the materials employed, use of less aggressive materials to the environment, high reproducibility, easy manufacturing and direct use of sunlight without diffusion losses.

Current photovoltaic technologies can be classified by generations, based on the materials and production techniques used for their fabrication. First generation solar cells are mainly based on crystalline silicon [4]. These types of solar cells are made of a single junction for extracting energy from photons and their efficiency is close to the maximum theoretical efficiency of $\sim$ 33 % [5, 6]. The highest research power energy efficiency reported for these photovoltaic (PV) cells is 20 %. However the industrial-grade cell efficiency is limited to 15-18 % [7]. A drawback of this kind of PV cells is that purification of silicon is a cost demanding task that requires high temperature processing.

Second generation solar cells are based on amorphous silicon [8], copper indium gallium diselenide (CIGS) [9], cadmium telturide (CdTe) [10], etc. These are less efficient but less expensive cells, and were of great interest in the 1990's and early this century. Thin film solar cells are designed in such a way that less material is required which results in low cost manufacturing process.

Third generation solar cells uses organic materials such as small molecules or polymers. These cells include polymer solar cells [11–13], dye-sensitized solar cells [14–16] and small molecule solar cells [17], among others. They are also called excitonic solar cells (XSC) due to its charge generation mechanism based on to the formation of excitons. A new class of thin film solar cells currently under investigation are perovskite solar cells [18] and show huge potential with record efficiencies beyond 20% [19] on very small areas. Polymer solar cells or plastic solar cells, on the other hand, offer several advantages such as a simple, quick and inexpensive large-scale production and use of materials that are readily available and potentially inexpensive. Polymer solar cells can be fabricated with well-known industrial roll-to-roll (R2R) [20] and screen-printing [21] technologies.

2.2 Excitons

Excitons are quasi-particles that form when Coulomb-interacting electrons and holes in semiconductors are bound into pair states. The term exciton can encompass a wide variety of states with very different structures and behaviors. Electron and hole, which are coulombically bound in an exciton, can be separated when their binding energy is overcome. Being electron-hole pairs, excitons carry no charge, which means that they do not contribute to electrical conduction. They do carry excitation energy, however, and their mobility therefore is responsible for energy transport processes [22, 23].

Excitons are usually distinguished in two classes: Frenkel excitons [24] and Wannier-Mott excitons [25]. The Wannier-Mott exciton is a loosely bound e-h pair; the strongly bound Frenkel exciton is practically localized within one monomer, and the constituent electron and hole lose their identity [26]. Figure 2.2 shows a schematic overview of the exciton formation by the absorption of the light in inorganic and organic semiconductors.

Physically, the distinction originates from the competition between two energy scales: the electron-hole coupling and the rates for electron and hole hopping between different molecules or atoms. The hopping rates allow the electrons and holes to move individually between different molecules in the solid or aggregate. This charge hopping arises from the overlap between the electron and hole orbitals on neighboring molecules. If the Coulomb coupling between electrons and holes can be neglected, this leads to freely moving electrons and holes, that may conduct electricity. The Coulomb interaction between electron and hole competes with their possibility to move independently through the system and if the interaction is strong enough it gives rise to bound electron-hole states, which appear as discrete levels below the continuum of ionized states in which electron and hole are essentially free. In fact, if the Coulomb attraction by far exceeds the hopping rates, the binding between electron and hole becomes too strong for them to separate and they always occupy the same molecule or atom [26, 28, 29].

Many technological applications envisioned for organic electronic materials, such as organic photovoltaics (OPV) and organic light-emitting diodes (OLED), involve the absorption and emission of light. The photophysical behavior of these materials is governed

Figure 2.2: Schematic overview of the exciton formation by the absorption of the light in inorganic and organic semiconductors.

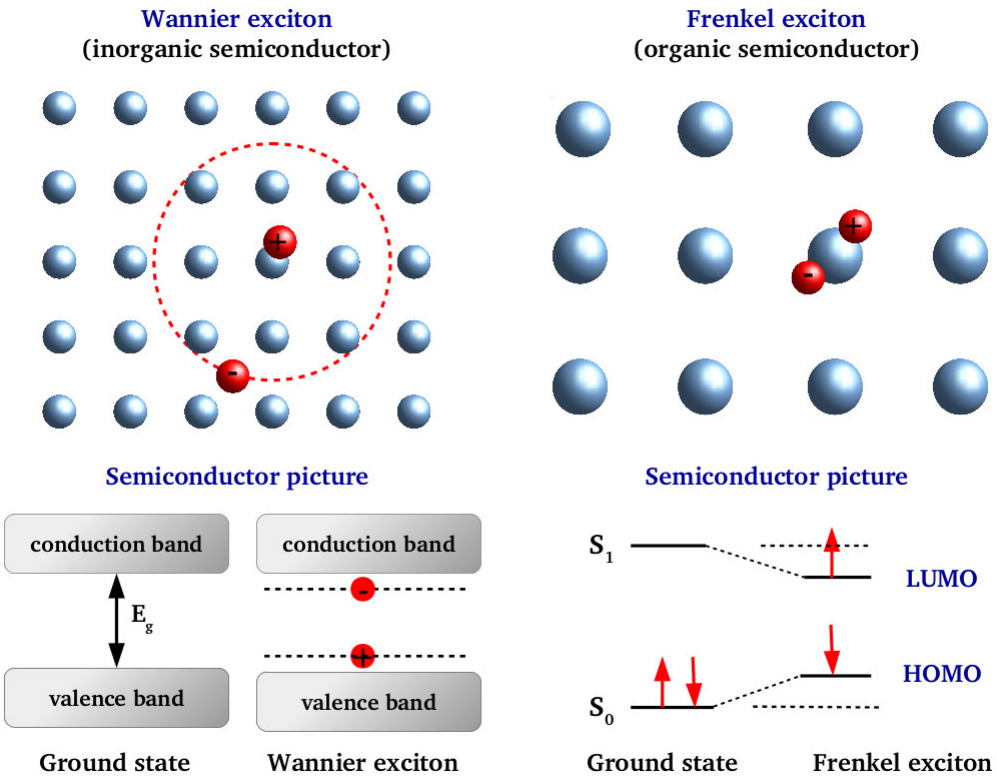

Source: Adapted from POPE AND SWENBERG (1999) [27].

by the structure and dynamics of their low-lying electronic states [23].

Figure 2.3 shows an schematic overview of the exciton formation in a molecule. An isolated molecule in its ground state has two spin-paired electrons residing in its highest occupied molecular orbital (HOMO). The promotion of an electron into the lowest unoccupied molecular orbital (LUMO) leaves a hole in the HOMO, resulting in an excited singlet or triplet state, depending on the electron's spin state [23].

The excited state in excitonic solar cells is a highly localized and slightly bound Frenkel exciton. Their energetics and transport are central to solar energy processes. The separation of the exciton into a free electron and free hole is the source of usable electrical energy in third generation solar cells. The diffusion of excitons to an engineered interface that can subsequently split them into electrons and holes remains a central challenge in many photovoltaic applications.

Figure 2.3: Schematic overview of the exciton formation in a molecule.

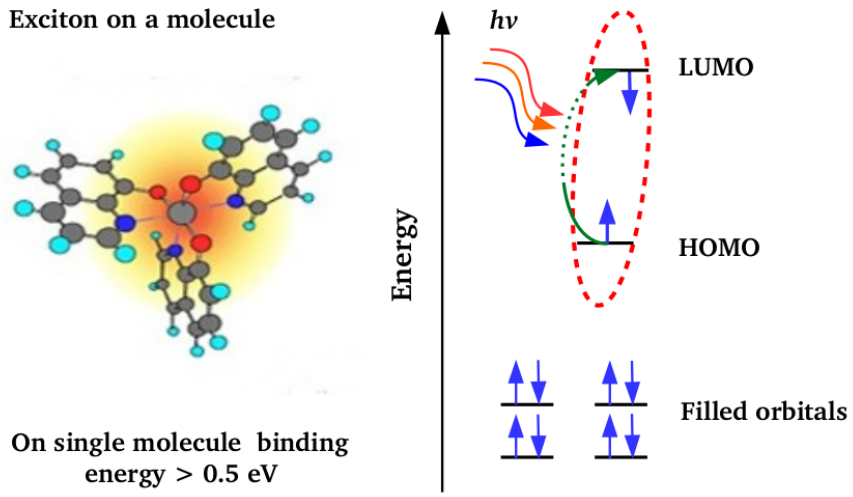

Source: RLE Center for Excitonics, Massachusetts Institute of Technology [30].

2.2.1 Singlet and triplet excitons

The ground state of the majority of organic molecules is electrically neutral and has net spin zero. A molecule can be excited when one electron from the HOMO is promoted to the LUMO, for instance by absorption of a photon. However, with respect to excitons that are created through charge injection, light absorption in organic semiconductors yields only singlet excitons and thus triplet excitons can only be formed through intersystem crossing [31, 32].

Photons do not show strong coupling to electronic spins because electromagnetic radiation does not carry any torque. The electron spin is an angular momentum that must be conserved. Thus the assistance of spin-orbit coupling is required to enable singlet to triplet transitions [31–33]. Triplet excitons are expected to have longer diffusion length than singlets due to their much longer lifetime. The triplet excitons slowly decay to the ground state since they lie in an energy state that is too low for dissociation [34]. Thus, intersystem crossing does not generally contribute to charge generation and may be viewed as a (delayed) recombination mechanism [35].

Figure 2.4 presents possible transitions between electronic states of an isolated molecule. In the figure, (1) represents the absorption of a photon that brings a molecule from the ground state S_0 to the first singlet excited state S_1; (transitions to higher singlet excited states are also possible). The transition (2) results in the emission of light and is called fluorescence. Triplet excited state T_1 can be created via the intersystem crossing (4). The radiative transition (6) is called phosphorescence.

Figure 2.4: Singlet and triplet states in a state diagram. The energies of singlet (S_0 and S_1) and triplet (T_1 and T_n) states are scaled vertically. Absorption (1), fluorescence (2), intersystem crossing (4), phosphorescence (5), nonradiative transitions (3 and 6) and photoinduced absorption (7) are presented as arrows.

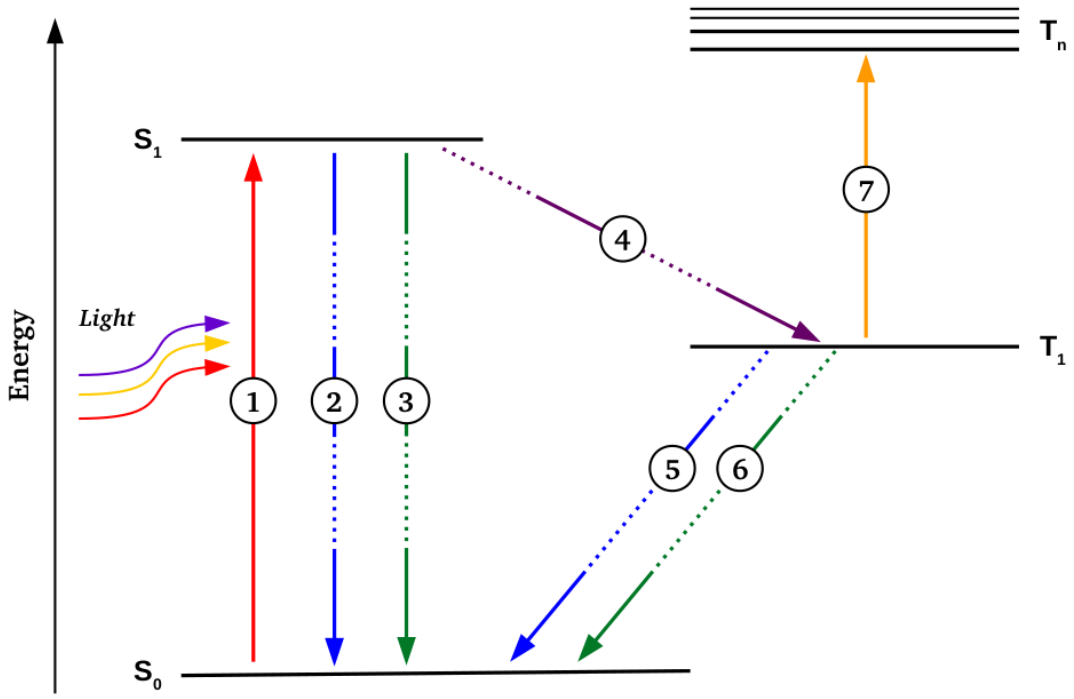

Source: Adapted from MIKHNENKO et al. (2015) [31] and KÖHLER AND BÄSSLER (2009) [32].

Fluorescence and/or phosphorescence can be also referred as photoluminescence (PL) when these transitions are initiated by absorption of a photon. The non-radiative transi-

tions (3) and (6) compete with fluorescence and phosphorescence. In organic materials, the energy stored in triplet states is not available for light emission because most of the triplet states decay non-radiatively. And finally, the transition (7) is the absorption of a photon that brings state T_1 to higher triplet excited states T_n.

Phosphorescence, (radiative decay) of the triplet excited state to the singlet ground state, is notoriously difficult to detect unless the emitter contains heavy atoms that enhance spin–orbit coupling. The latter ensures first that any primarily generated singlet states convert to triplets, and, more importantly, that the spin-forbidden $T_1 \rightarrow S_0$ transition becomes partially allowed and so acquires intensity [32].

2.2.2 Exciton diffusion

Organic solar cells are based on a bulk heterojunction (BHJ) architecture that can be achieved by mixing two solutions of organic semiconductors with different electronegativities and subsequently spinning a film [11]. Their operation requires the photoexcited state in one material to diffuse until it reaches the interface to the other material, where dissociation takes place provided the energy gained exceeds the exciton binding energy [36]. For this to happen it is necessary that the size of the phase separation between the two materials be on the same length scale than the exciton diffusion length.

The ability of photoexcited exciton states to diffuse spatially provides the basis for many of their useful properties, especially in photovoltaics [23]. The exciton diffusion length can be estimated by the relation [23, 31, 35]:

$$L_{\mathrm{D}} = \sqrt{6\, D\, \tau}, \tag{2.1}$$

where D is the exciton diffusion coefficient and τ is the exciton lifetime.

In many organic semiconductors the singlet exciton diffusion length is of the order of 3-6 nm [36–38], while the triplet diffusion length has been reported in a wide range from 10 to 100 nm [39, 40]. Therefore, it has been conjectured that a possibly larger diffusion length of triplet excitons compared to singlets may be of advantage for solar cells.

2.3 Characterization

2.3.1 J× V curve

A solar cell is usually characterized by photovoltaic parameters obtained from a J×V characteristic curve like the one shown in Fig. 2.5.

Figure 2.5: J×V characteristic curve of a solar cell.

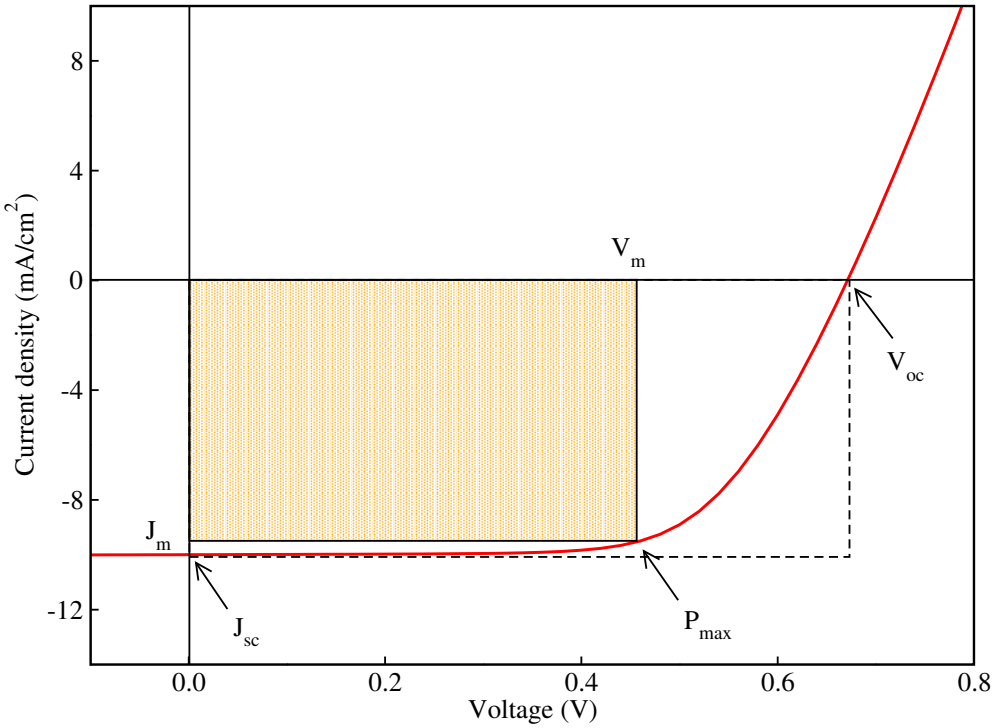

Source: Own author.

In general, the photovoltaic parameters are defined as:

- Open circuit voltage (V_{oc}): is the maximum voltage that a solar cell is capable of supplying; that is the voltage without any load applied.

- Short-circuit current density (J_{sc}): is the maximum current density flowing through a solar cell under conditions of a zero resistance load; a free flow or zero volt potential drop across the cell.

- Fill factor (FF): is essentially a measure of quality of the solar cell. It is calculated by comparing the maximum power to the theoretical power that would be output at both the open circuit voltage and short-circuit current density together. The FF can assume values between 0 and 1 and is obtained by the relation:

$$\mathrm{FF} = \frac{J_m V_m}{J_{sc} V_{oc}} \tag{2.2}$$

  where $P_m = J_m V_m$ is obtained as the product of the photocurrent and photovoltage at the voltage where the power output of the cell is maximum.

- Power conversion efficiency (η): is given as they ratio of the maximum power delivered by the device (P_m) to the incident power (P_{in}) of the light source:

$$\eta = \frac{P_m}{P_{in}} = \frac{J_{sc} V_{oc} \times FF}{P_{in}}. \tag{2.3}$$

  P_{in} is taken as the product of the irradiance of the incident light, measured in $\mathrm{W/m^2}$, with the surface area of the solar cell.

2.3.2 Equivalent Circuit Model

Figure 2.6 depicts the widely used equivalent circuit solar cell model. The behavior of the $J \times V$ curve of the solar cell can be decomposed into four constituent parts: photocurrent source, diode, series resistor, and shunt resistor.

The photocurrent source is simply the result of converting absorbed photons to free charges by the solar cell; the diode represents electron-hole recombination at the p-n junction; the series resistor accounts for the internal resistance of the cell to current flow; and the shunt resistor models leakage current through the cells. Mathematically this model is represented by the relationship [41–43]:

$$J = J_0 \left[\exp\left(\frac{e(V - JR_s)}{n k_B T} \right) - 1 \right] + \frac{V - JR_s}{R_{sh}} - J_{ph} \tag{2.4}$$

where J_0 is the reverse bias saturation current density, J_{ph} is the photocurrent density, e

is the elementary charge, R_s is the series resistance, n is the diode ideality factor, k_B is the Boltzmann constant, T is the temperature, and R_{sh} is the shunt resistance.

Figure 2.6: Traditional model of an equivalent circuit for a solar cell.

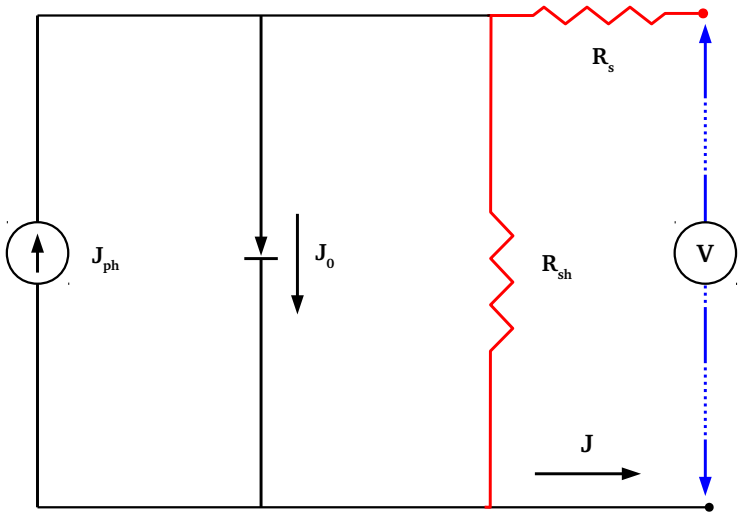

Source: Adapted from HAINS et al. (2010) [42].

In cells with low leakage currents, $R_{sh} \gg R_s$, and the equation simplifies to:

$$J = J_0 \left[\exp\left(\frac{e(V - JR_s)}{nk_BT} \right) - 1 \right] - J_{ph}. \tag{2.5}$$

When R_S is negligible, eq. 2.5 can be rearranged at open circuit to yield [43, 44]:

$$V_{oc} = \frac{nk_BT}{e} \ln\left(\frac{J_{sc}}{J_0} + 1 \right). \tag{2.6}$$

Ideally J_{sc} increases linearly with light intensity I, V_{oc} increases with $\ln(I)$, and the FF is independent of I. Thus, maximum power ideally increases as $\ln(I)$. Power losses are minimized as the values of series and shunt resistances approach the ideal values of $R_s = 0$ and $R_{sh} \to \infty$ [43, 44].

The series resistance arises from the resistance of the cell material to current flow, particularly through the surface to the contacts, and from resistive contacts. Series resistance is a major problem at high current densities, for instance under concentrated light. The parallel or shunt resistance arises form leakage of current through the cell, around the edges of the device and between contacts of different polarity.

A high value of R_s does not affect V_{oc} but reduces J_{sc} and FF. High R_s may result from low charge carrier mobilities and barriers to charge extraction at the electrodes. For large area devices, resistance losses within the electrodes may also contribute significantly. A low value of R_{sh} does not affect J_{sc} but reduces V_{oc} and FF [45, 46].

2.3.3 External quantum efficiency

Another fundamental measurement of the performance of a solar cell is the external quantum efficiency (EQE) also known as the incident photon-to-current conversion efficiency (IPCE). The EQE is defined as the ratio between the number of collected photogenerated charges at the electrodes to the number of incident photons at a particular wavelength, as a function of incident energy. It is the probability that the absorption of one photon will result in the generation of one electron that is able to flow through an external circuit, and is typically integrated over the solar spectrum.

The EQE value corresponds to the photocurrent density produced in the external circuit under monochromatic illumination of the cell divided by the photon flux that strikes the cell. From such an experiment the EQE as a function of wavelength can be calculated as [47]:

$$EQE(\lambda) = \frac{J_{sc}(\lambda)}{e\,\Phi(\lambda)} = 1240\,\frac{J_{sc}(\lambda)\ (A/cm^2)}{\lambda\ (nm)\,P_{in}\ (W/cm^2)} \tag{2.7}$$

where Φ is the photon flux, P_{in} is the incident power, λ is the wavelength of the incident light and e is the elementary charge. EQE values provide practical information about the monochromatic quantum efficiencies of a solar cell.

2.4 Dye-sensitized solar cells

The dye-sensitized solar cell (DSSC) technology exhibit peculiar characteristics which differentiate them from other photovoltaic technologies. In DSSC technology the spectral properties optimization can be done by modifying the dye, while carrier transport properties can be improved by optimizing the semiconductor and the electrolyte composition. In 1991, O'Regan and Grätzel demonstrated that a film of titania (TiO_2) nanoparticles deposited on a DSSC would act as a mesoporous n-type photoanode and thereby increase the available surface area for dye attachment by a factor of more than a thousand [48].

A schematic representation of a DSSC is shown in Fig. 2.7. An actual DSSC contains, in general, five components:

1. A mechanical support coated with transparent conductive oxides (TCO) such as fluorine-doped tin oxide (FTO);

2. A semiconductor film (photoanode), usually based on TiO_2 [49], SnO_2 [14, 15] or ZnO [50];

3. A dye-sensitizer adsorbed onto the surface of the semiconductor. Sensitizing dyes have traditionally been made from ruthenium-based complexes such as cis-Bis(isothio cyanato) bis(2,2'-bipyridyl-4,4'-dicarboxylato ruthenium(II) (N3) and Di-tetrabutyla mmonium cis-bis(isothiocyanato)bis(2,2'-bipyridyl-4,4'-dicarboxylato) ruthenium(II) (N719) [14, 15, 50];

4. An electrolyte containing a redox mediator such as iodide/triiodide systems [14, 15, 50];

5. A counter electrode, like platinum, capable of regenerating the redox mediator.

DSSCs are unique compared with almost all other kinds of third generation solar cells in that electron transport, light absorption and hole transport are each handled by different materials in the cell [51]. The sensitizing dye in a DSCC is anchored to a wide-band gap semiconductor such as TiO_2, SnO_2 or ZnO. When the dye absorbs light, the photoexcited electron is rapidly transfered to the conduction band of the semiconductor,

Figure 2.7: Schematic overview of a DSSC.

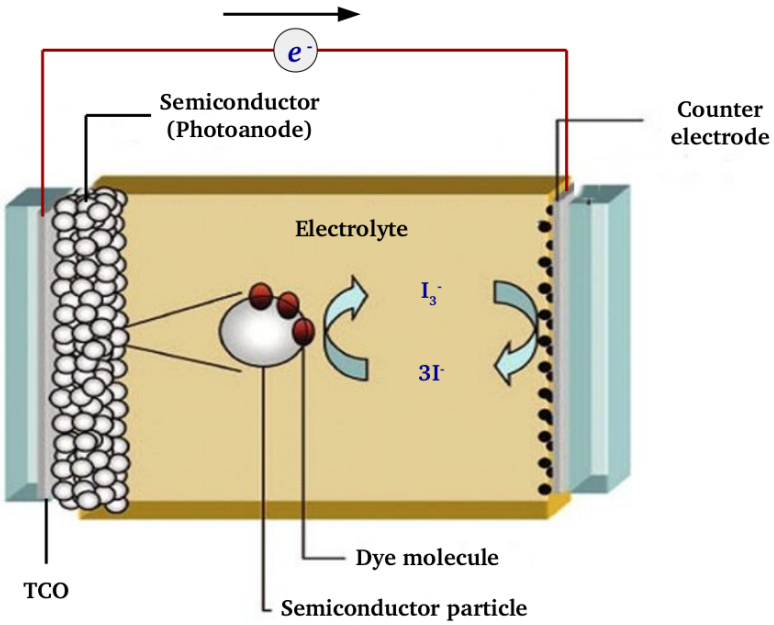

Source: Adapted from HAGFELDT et al. (2010) [47].

which carries the electron to one of the electrodes. A redox couple, usually comprised of iodide/triiodide (I^-/I_3^-), then reduces the oxidized dye back to its neutral state and transports the positive charge to the platinized counter-electrode.

2.4.1 Generation and recombination mechanisms

An energy level diagram showing the operation of a typical DSCC is shown in Fig. 2.8. The first step (1) is the absorption of a photon by the sensitizer dye (D) leading to an excited state (D^*) from which an electron is injected into the conduction band of the semiconductor (2), leaving the dye-sensitizer in the oxidized state that is regenerated by the redox couple (3). Unlike traditional inorganic solar cells, DSSCs require relatively large over-potentials to drive electron injection to semiconductor and regenerate the oxidized dye, as shown in Fig. 2.8. Typically, a potential difference between the lowest unoccupied molecular orbital (LUMO) level of the dye and the conduction band of semiconductor is required for fast electron injection [47].

Figure 2.8: Operating principles and energy level diagram of a typical DSSC.

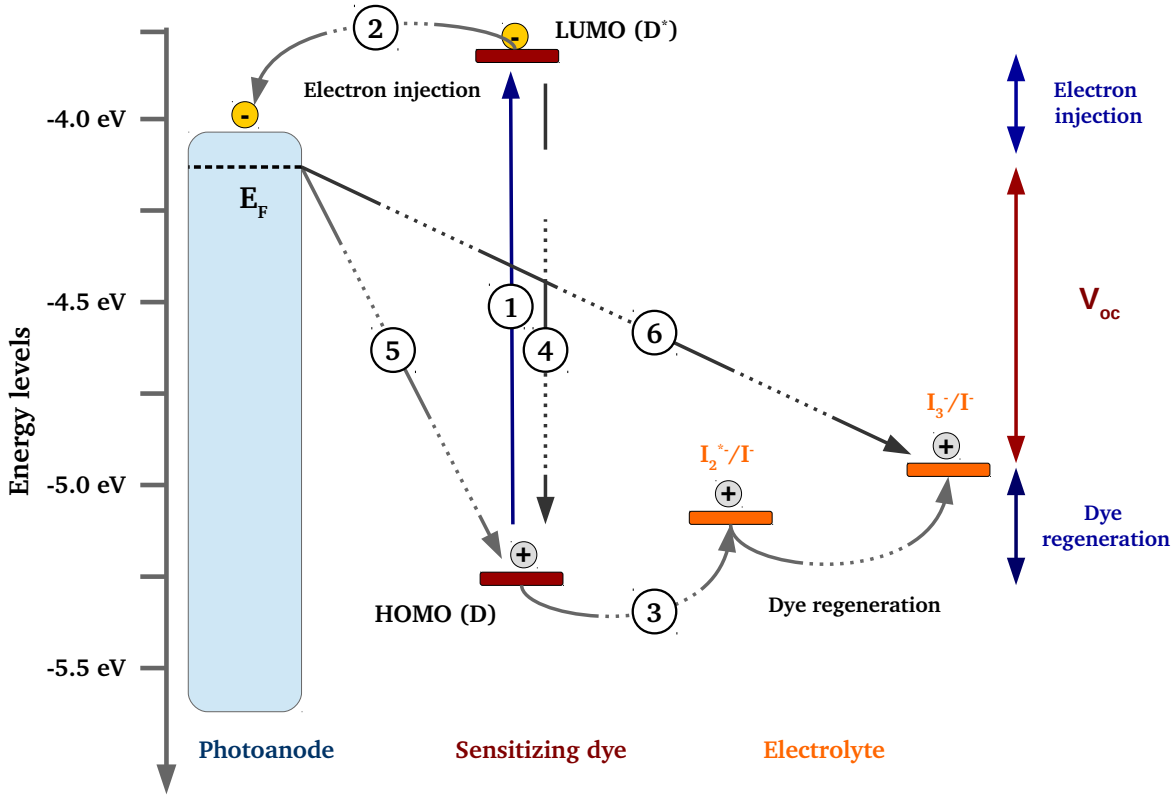

Source: Adapted from HARDIN et al. (2012) [51].

In some cases, recombination between charge carriers generated by photon absorption may occur. A few possible recombination mechanisms are: direct recombination of the excited dye reflected by the excited state lifetime (4), recombination of injected electrons in the semiconductor with either oxidized dyes (5) or (6) acceptors in the electrolyte.

The iodide/triiodide system has been particularly successful in DSSCs because of the slow recombination kinetics between electrons in the titania with the oxidized dye and the triiodide in the electrolyte, which leads to long-lived electron lifetimes [52]. Iodide reduces the oxidized dye to form an intermediate ionic species (such as I_2^{*-}) that then disproportionates to form triiodide and diffuses to the counter-electrode, providing two electrons per molecule, as shown in Fig. 2.8. The small size of the I^-/I_3^- redox components allows for relatively fast diffusion within the mesopores, and the two-electron system allows for a greater current to be passed for a given electrolyte concentration.

The injected electron flows through the semiconductor network to arrive at the back contact and then through the external load to the counter electrode to reduce the redox mediator. This completes the circuit.

2.5 Organic Solar Cells

Organic semiconductors can be broadly classified into two categories: small molecules or oligomers [53] and polymers [54]. In 1977, Shirakawa *et al* [55] reported on their discovery of electrically conductive polymers (for which, in 2000, the Nobel Prize in Chemistry was awarded jointly to Heeger, MacDiarmid and Shirakawa). This report boosted the research in organic semiconductors aiming its application in new technologies. Organic semiconductors have several unique physical properties, which offer many advantages compared with inorganic semiconductors, such as:

- the extremely high absorption coefficients of some polymers and organic dyes in the visible range offer the possibility to prepare very thin photovoltaic cells [56];
- many fluorescent dyes emit strongly red-shifted light compared to their absorption. Thus, there are almost no reabsorption losses in organic light-emitting diodes [57];
- since organic semiconductors consist of molecular structures with saturated electron systems, the number of intrinsic defects in disordered systems is much lower than that in inorganic amorphous semiconductors having a large number of dangling bonds [58];
- a nearly unlimited number of chemical compounds is available, and it is possible to prepare tailor-made materials [54];
- organic semiconductors can usually be deposited on room temperature substrates and are very well compatible with flexible substrates [20].

Figure 2.9 presents an illustration of a bulk heterejunction organic solar cell. The typical structure, from top to bottom, consists of a transparent electrode, which is generally composed of glass coated with a transparent conducting oxide, usually tin-doped

indium oxide (ITO) or fluorine tin oxide (FTO). This is followed by an interfacial layer composed of a hole transport material (HTM), typically an organic or metal oxide layer, such as PEDOT:PSS[59], V_2O_5 [60] or MoO_3 [61]. Next, the active layer, composed of two materials: (i) the absorber, which is responsible for the photovoltaic activity of the cell, consists of an interpenetrating network of electron donor (hole-transporting) and (ii) acceptor (electron-transporting) materials. In state-of-the-art systems, the donor is generally the light-absorbing material. The bottom contact typically consists of a second interfacial layer composed of an electron transport material (ETM) as ZnO [11], SnO_2 [62] or TiO_2 [63]. Finally, a low work function metal electrode, such as Ag or Al.

Figure 2.9: Schematic of a BHJ OSC: normal and inverted arquiteture.

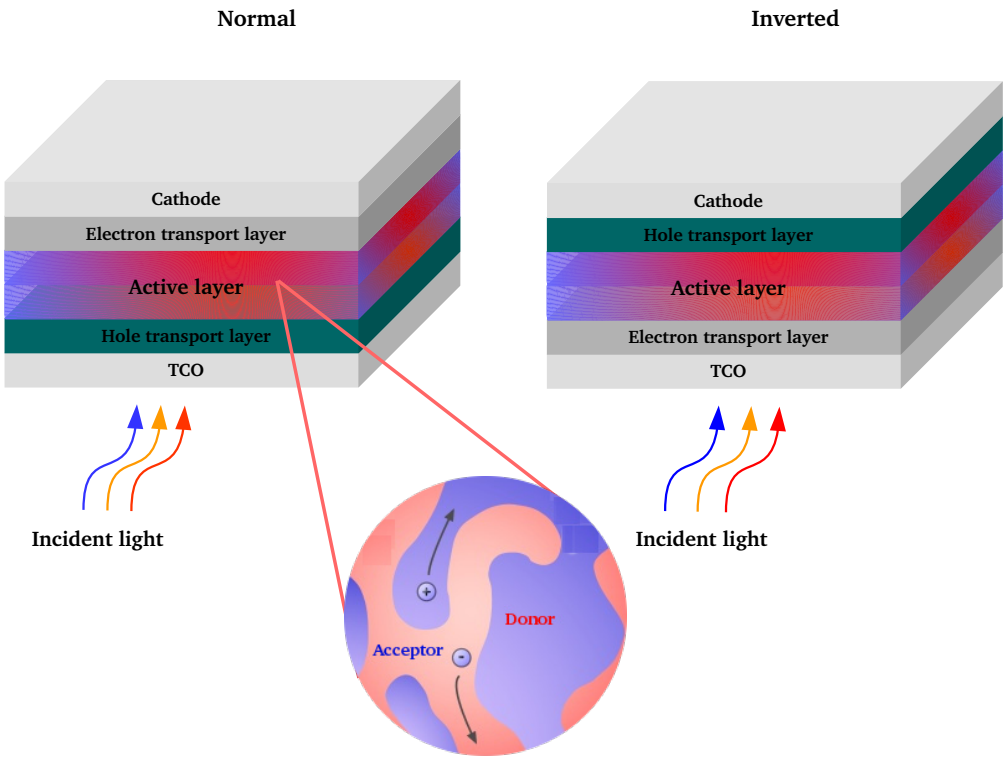

Source: Own author.

2.5.1 Mechanism of photon-to-electron conversion process

Figure 2.10 illustrates the four fundamental steps involved in the photon-to-electron conversion mechanism for OPVs.

Figure 2.10: Fundamental mechanism of the photon-to-electron conversion process in BHJ OSCs.

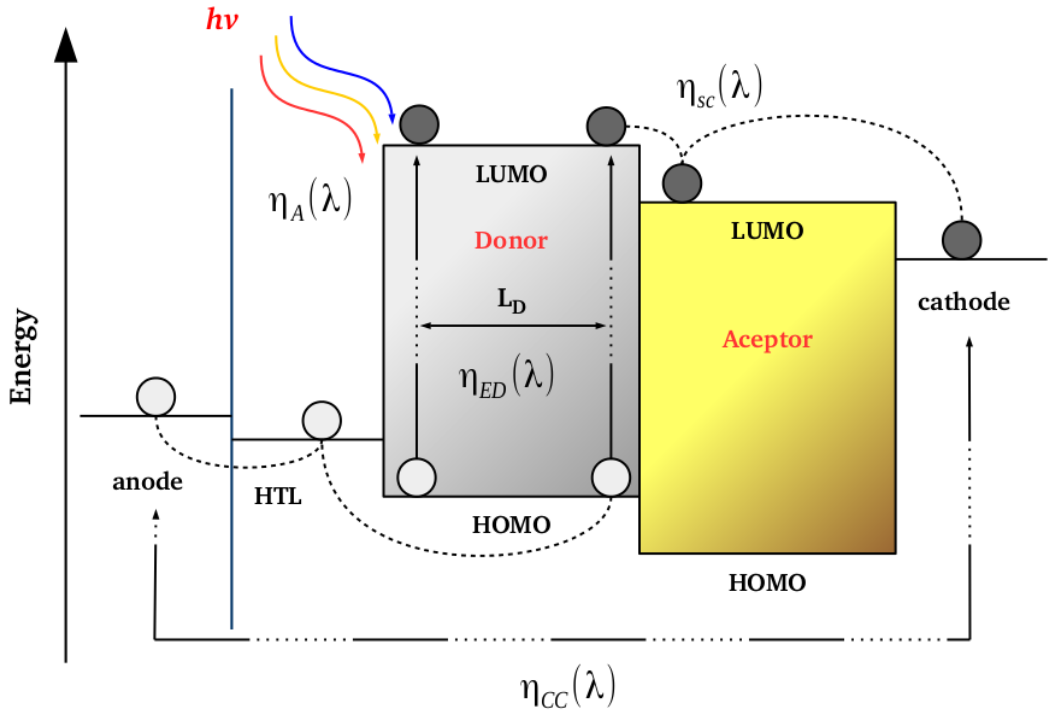

Source: Adapted from SU et al. (2012) [64].

First, upon the absorption of light, an electron in the donor undergoes photoinduced excitation from the HOMO to the LUMO of the organic material, forming a Frenkel exciton [24] (coulombically bound electron (e^-) and hole (h^+). The ratio of the generated Frenkel excitons to the total incident photons, in terms of energy, is defined as the absorption efficiency (η_A). Excitons in organic materials have a binding energy of 0.5–1 eV [65], due to their low dielectric permittivity [66] ($\epsilon = 3$–4), which is substantially higher than

the thermal energy at a room temperature of 0.025 eV. Thus, if the organic material is to serve as an electron donor in OPVs, a second material is required as an electron acceptor to ensure a built-in internal field at the interface to break up any excitons that diffuse there into free carriers. The most widely used acceptor materials are fullerenes, which have electron affinities greater than those of polymers or small molecules [64].

Second, the excitons must diffuse to the donor-acceptor (D-A) interfaces within the diffusion length (L_D) to prevent recombination to the ground state. Because the value of L_D in organic materials is typically 10 nm [37, 38, 40], the ideal donor or acceptor domain size should be less than 20 nm. This D-A interface concept is analogous – in terms of charge transport – to a p-n junction in an inorganic semiconductor. The ratio of the number of excitons that reaches the D-A interface to the total number of excitons generated through photoexcitation is defined as the exciton diffusion efficiency (η_{DE}).

Third, an exciton at a D-A interface undergoes charge-transfer (CT) process at an ultrafast pace [67] (ca. 100 fs) to form a CT exciton, where the hole and electron remain in the donor and acceptor phases, respectively, held together through coulombic attraction. The charge separation efficiency (η_{CS}) is defined as the ratio of the number of excitons that have undergone the CT process to the number of excitons that have reached the D-A interface.

Fourth, the CT exciton dissociates, as a result of the built-in electric field, into free holes and electrons, which are then transported through the donor and acceptor phases, respectively, to their respective electrodes. The transport of free carriers to the respective electrodes occurs within a period of time ranging from nano to microseconds. The charge collection efficiency (η_{CC}) is defined as the ratio of the number of carriers that have been collected at the electrodes to the number of excitons that have undergone the CT process.

2.5.2 Relationship between the energy band and the η of a device

As mentioned in a previous section, the efficiency of a solar cell can measured as the product of V_{oc}, J_{sc} and FF. V_{oc} is determined by recombination as well as the energy level alignment between the photoactive polymer donor and the fullerene acceptor, J_{sc}

is determined by the light harvesting and the charge separation efficiency under large extraction fields, and FF is determined by the device series resistance, the dark current and the charge recombination/extraction rate under low internal fields.

EQE describes the overall efficiency of the four main processes in the photovoltaic process for OSCs, including absorption, exciton diffusion, charge separation, and charge collection, as defined by the relation [64, 68–70]

$$EQE = \eta_A(\lambda)\,\eta_{DE}(\lambda)\,\eta_{CS}(\lambda)\,\eta_{CC}(\lambda) \tag{2.8}$$

where λ is the wavelength of incident light. EQE values close to 100 % for a specified wavelength indicate efficient current generation for light absorbed at that wavelength, with limited recombination losses. Increasing recombination or reflection losses result in lower EQE values.

The value of J_{sc} is influenced by the breadth of the light absorption spectrum (determined mainly by the gap energy, E_g), the extent of light absorption (determined by the thickness of the active layer), and the morphology of the active layer. Among all of the approaches to improve η, the most common and successful strategy is developing new low band gap donor materials to maintain a broad overlap with the solar spectrum and ensure effective harvesting of solar photons, which leads to higher J_{sc} [71]. Theoretically, J_{sc} is defined by the relation [64],

$$J_{sc} = \frac{hc}{e}\int \frac{P_{in}EQE(\lambda)}{\lambda}\,d\lambda \tag{2.9}$$

where P_{in} represents the incident power, e the elementary charge, h the Planck constant, and c the speed of light. Since the absorbed photon energy (E_{ph}) is inversely proportional to the wavelength

$$E_{ph} = \frac{1240}{\lambda\ (nm)}\ \text{eV}, \tag{2.10}$$

J_{sc} generally increases with increasing λ across the visible and infra-red regions of the solar spectrum.

Theoretically, the value of V_{oc} is linearly proportional to the difference in energy levels between the HOMO of the donor and the LUMO of the acceptor. Therefore, to enlarge the value of V_{oc} , one can either lower the HOMO of the donor or raise the LUMO of the acceptor [64, 69]. For effective charge transfer process, however, the LUMO of the conjugated polymer must be higher [69, 72] (by at least 0.3 eV) than that of the fullerene. Thus, V_{oc} can be obtained by:

$$V_{oc} = \frac{1}{e}\{E_{D(\mathrm{HOMO})} - E_{A(\mathrm{LUMO})}\} - 0.3\ eV. \tag{2.11}$$

Hence, the value of V_{oc} is determined essentially by the material properties of the donor and acceptor in the active layer, although different cathode materials also have an effect. The value of $\{E_{(D(\mathrm{HOMO})} - E_{A(\mathrm{LUMO})}\}/e$ is equal to the built-in potential (V_{bi}).

2.5.3 Doping of organic semiconductors

Due to the very different structure of organic and inorganic semiconductors, one can expect significant differences in the properties of doped layers. However, there are many similarities in the basic properties of the doping process. Doping inorganic semiconductors by controllably introducing impurity atoms is the basis of several functionality in today's electronic devices. It allows tuning the energy level alignment at interfaces between differently doped materials and at interfaces to metal contacts. Dopant atoms in a highly pure material are covalently bonded to the surrounding matrix, where they introduce electronic defect states in the fundamental gap of the semiconductor [73]. The basic principle of doping in inorganic semiconductors is illustrated in Fig. 2.11.

Key differences in the doping behavior are caused by the fact that the transport is driven by electron hopping in a distribution of more or less localized states. A major impact on the transport properties in organic semiconductors can be expected in particular when the frontier (HOMO/LUMO) molecular orbitals of the impurities have energies that fall within the HOMO-LUMO gaps of the pure molecules. One distinguishes between deep traps (when the trapping energy is much larger than k_BT and shallow traps (when the trapping energy is on the order of k_BT, which allows for thermal detrapping) [75].

Figure 2.11: Doping mechanisms of molecular p-type and n-type doping. In p-type doping the molecular dopant acts as acceptor and in n-type doping as donor. A sufficient energetic overlap of matrix and dopant energy levels is required for efficient doping.

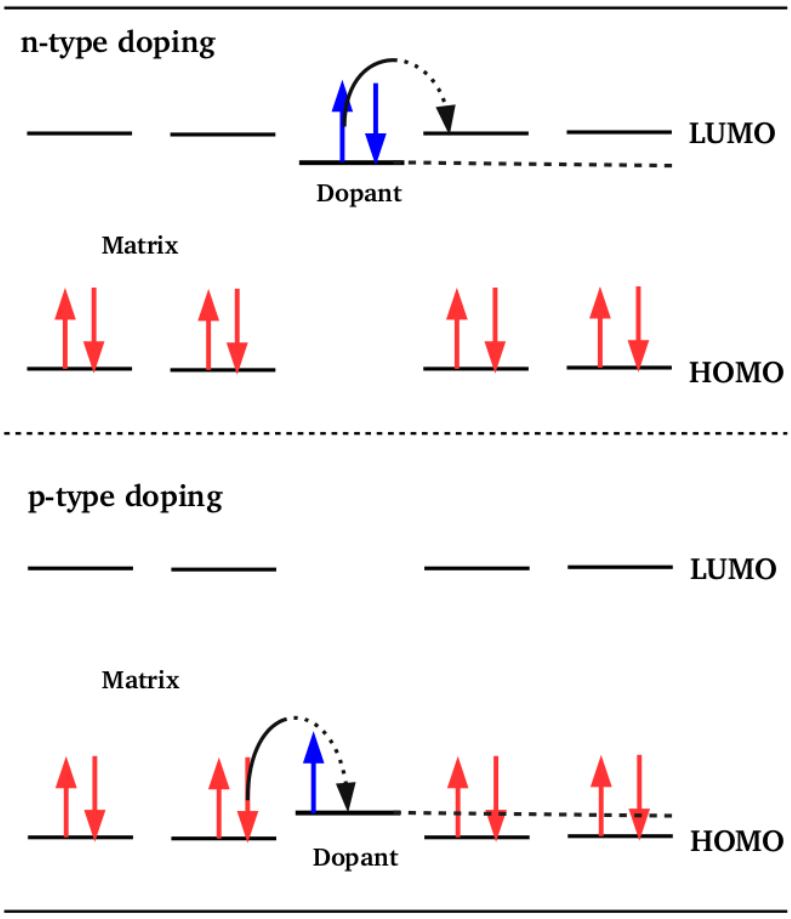

Source: Adapted from WALZER et al. (2007) [74].

In purely organic compounds, emission from a spin triplet state, i.e. phosphorescence, is forbidden by spin-selection rules and it is thus only very weak. When a heavy metal is incorporated in the otherwise organic structure this allows for a spin flip, so that emission becomes possible and is strong. Knowledge of electronic processes involving the triplet state is necessary not only because the understanding of the electronic structure of organic semiconductor is incomplete without it, but also because the triplet state plays a significant role in device applications. As the name suggests, there are three degenerate triplet states to one singlet state [32].

Recently, it has been shown that doping the active layer of BHJ OSCs with magnetic nanoparticles (MNPs) improves their photovoltaic parameters [11, 33, 59, 76]. Currently there are two non-exclusive possible explanations. One claim is that a coercive electric field generated by dipole interactions from magnetic MNPs dispersed in the active layer increases the driving force that dissociates excitons on the donor/acceptor interfaces [59, 76]. The other claim is that a spin-orbit coupling [11, 33] due to the presence of NP magnetic moments increases the efficiency of intersystem crossing process in the device, and thus extends the lifetime (and diffusion length) of the photogenerated excitons.

2.5.4 Donor and acceptor materials

OSCs in which the photoactive layer is composed of a semiconductor polymer (electron donor) and a fullerene derivative (electron acceptor) have been subject of intense research. Experimental data from BHJ solar cells are based on the combination of a variety of donor and acceptor materials fabricated in different laboratories and characterized by different techniques. Most OSCs are made with bulk heterojunctions wherein an electron donating polymer and an electron accepting fullerene derivative form nanoscaled interpenetrating networks allowing efficient exciton dissociation and carrier transport [72, 77].

The polymer donor serves as the main solar light absorber and as the hole transporting phase, whereas the small molecule transports electrons. Therefore a wide optical absorption range (to match the solar spectrum), large extinction coefficients, and large carrier mobilities are basic requirements toward the design of ideal photoactive blends [54].

Figure 2.12 shows the HOMO and LUMO energy levels of some of the state-of-the-art photovoltaic polymers, electron accepting fullerene derivatives and the electron affinities and ionization energies of high/low work function metal oxides.

A fundamental difference of organic photovoltaic (OPV) compared with inorganic photovoltaic materials is the creation of strongly bound electron–hole pairs (excitons) upon absorption of light in the organic semiconducting materials. The energy which is required to split an exciton is in the range of 100–400 meV compared to a few meV for crystalline semiconductors. The thermal energy k_BT at standard conditions and the

electric field is not sufficient to dissociate these excitons. In order to split excitons into free charge carriers, the energy can be provided in the presence of an electron accepting material with a different electron affinity than the donor material [78].

Figure 2.12: The energy level diagram of state-of-art photovoltaic polymers, electron-accepting fullerene derivatives, and transition metal oxides.

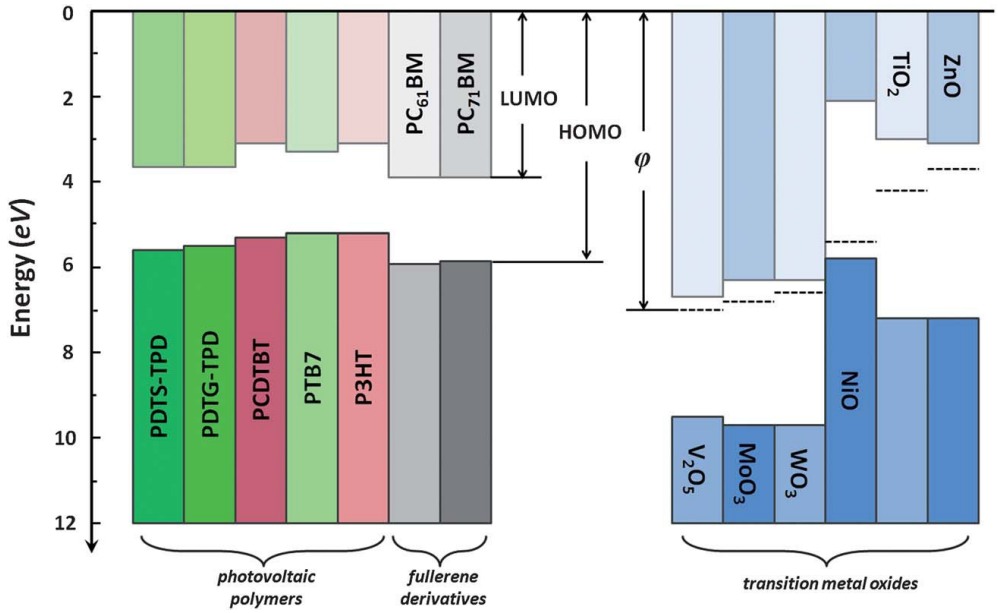

Source: CHEN et al. (2012) [77].

2.5.5 Electron and hole transport materials

Figure 2.12 shows some p-type and n-type materials used as interfacial layer in OSCs. Metal oxides can be p-type and n-type materials, depending on the position of the valence band and conduction band. For a p-type contact material, the valence band of the metal oxide is required to match the HOMO of the polymer. For an n-type material, electron transfer from the LUMO of the acceptor to the conduction band of the metal oxide is required [78].

Poly(3,4-ethyl-enedioxythiophene) (PEDOT) is widely used as a solution processed p-type interfacial layer and transparent electrode material in organic electronics. Usually,

PEDOT is doped with Poly(styrene sulfonate) (PSS) for improved conductivity and solubility in protic solvents. Additionally, p-type transition metal oxides (TMOs) have been successfully introduced in OPV. High work-function TMOs like V_2O_5 [11] or MoO_3 [61] as interlayers on the anode side have been evidenced to allow for efficient hole extraction.

TiO_2 [63], ZnO_2 [11] and SnO_2 [62] are extensively studied n-type materials for interfacial layers in OPV devices. These materials are transparent in the visible light spectrum but absorb ultraviolet (UV) light. The thickness of the interfacial layer is tunable without absorption losses in the visible (VIS) light and thus can additionally act as optical spacer.

n- and p-type semiconductivity in metal oxides are, in general, due to the intrinsic point defects such as atomic vacancies present in the oxides. These metal oxides form Ohmic contacts with photovoltaic polymers and fullerenes through favorable vacuum level shift, energy level bending and Fermi level pinning at the polymer-electrode interfaces. In addition, the use of oxide interlayers circumvents the direct contact between a photoactive polymer and electrodes, where high densities of carrier traps or unfavorable interface dipoles hinder efficient charge collection [77].

2.6 Oxide nanoparticles

2.6.1 Tin oxide

Tin dioxide (SnO_2) is a typical wide band gap n-type semiconductor with direct band gap of about 3.6 eV at room temperature. It is one of the most widely used semiconductor oxide due to its chemical and mechanical stability [79] and excellent optical and electrical properties [80, 81]. It has a rutile-type tetragonal crystal structure with a $P4_2/mnm$ space group [82, 83]. Its unit cell consists of two Sn^{4+} and four O^{2-} ions with each tin cation coordinated by six oxygen anions in the corners of a regular octahedron. Each oxygen anion is surrounded by three Sn^{4+} ions which approximate the corners of an equilateral triangle [83] as shows the Fig. 2.13. Tin oxide has many technological applications such as in solar cells [11, 14, 62], photocatalytical activity [84], gas sensors of toxic materials [85, 86] and anodes for lithium ion batteries [87].

Figure 2.13: Schematic representation of tin oxide structure.

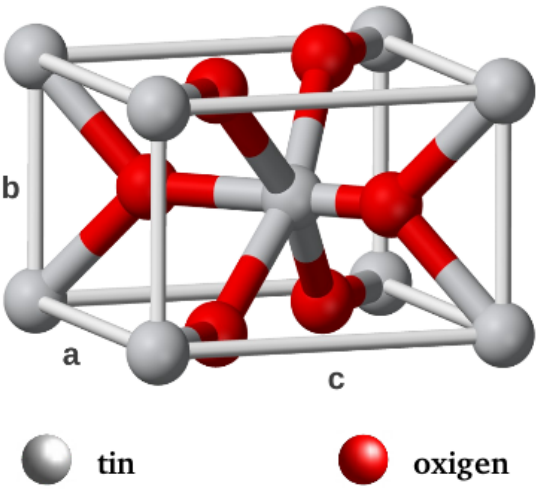

Source: Own author.

2.6.2 Oxide diluted magnetic semiconductors

Oxide diluted magnetic semiconductors (O-DMS), where transition metal (TM) atoms of $3d$ valence electrons are introduced into the cationic sites of the semiconducting host lattice, have attracted the interest of researchers due to their potential use in future spintronic and magneto-optical devices [88–90]. The discovery of room temperature ferromagnetism (RTFM) in Co-doped TiO_2 [91], ZnO [92] and SnO_2 [93] systems has played a crucial role in expanding the field of DMS to oxides, leading to a rapid development of new materials for application in advanced technology. As a result, intensive attention has been focused on O-DMS such as Fe-doped ZnO [94], SnO_2 [95], and TiO_2 [96]. One of the main features of these systems is that they can exhibit an intrinsic ferromagnetism at room temperature or above. Among the different semiconductor materials, the oxides with wide band gap such as TiO_2 and SnO_2 has been a subject of recent investigations due to their potential applications in the emerging fields such as photovoltaic cells [11] and anodes for lithium ion batteries [87].

2.6.3 Spinel ferrites

Ferrites are chemical compounds with the formula of AB_2O_4, where A and B represent various metal cations, usually including iron. Ferrites exist principally as garnet, spinel,

and hexaferrite structures [97]. Spinel ferrite structure is shown in Fig. 2.14. Cations have either four-fold or six-fold coordination forming tetrahedra A and octahedra B sublattices that are arranged in a close packed arrangement with respect to each other. A cations reside on 8 of 64 available tetrahedral sites whereas B cations reside on 16 of 32 available octahedral sites. Oxygen anions form a close packed structure and contribute 32 ions that electrically balance the unit cell [97]. The overall symmetry of oxygens is fcc (face centered cubic), which defines two types of interstitial sites. The space group is *Fd3m* [97–99].

Figure 2.14: Schematic representation of spinel ferrite structure.

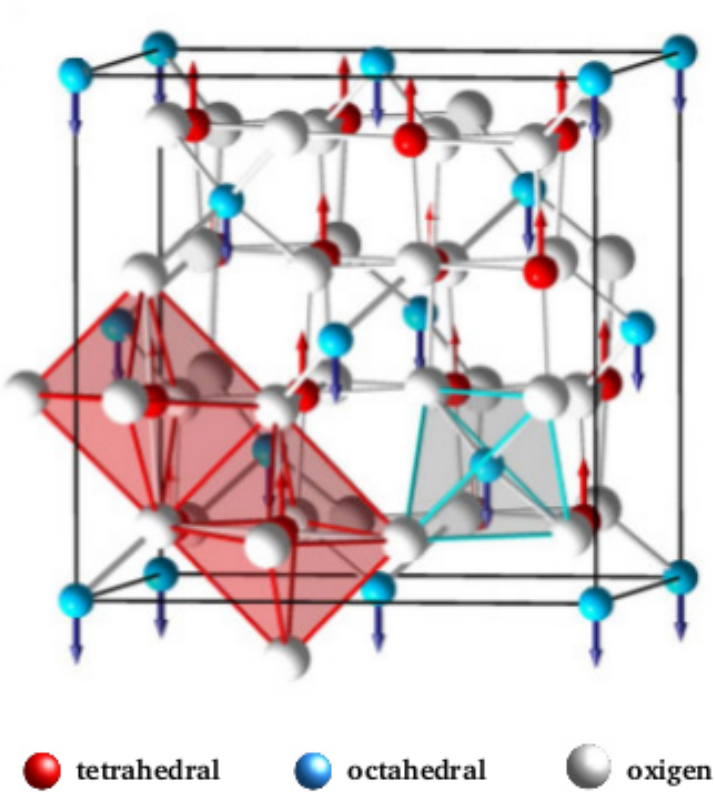

Source: SUTKA AND MEZINSKIS (2012) [100].

Spinel ferrite nanopaticles (SFNPs) are in the spotlight of current nanoscience due to immense application potential. Some of the interesting aspects of SFNPs are their

excellent magnetic properties often accompanied with other functional properties, such as catalytic activity [99]. Moreover, the magnetic response of the SFNPs can be tuned by particle size and shape up to some extent. Consequently, various spinel ferrite NPs are suggested as universal and multifunctional materials for exploitation in biomedicine [101], catalysis [102], sensing [103] and photovoltaic cells [59, 76]. Thus it is of ultimate interest to get control over their functional properties, which requires in-depth understanding of the correlation between their structural and magnetic order.

2.7 References

[1] LEWIS, N. S.; CRABTREE, G. *Basic research needs for solar energy utilization.* [S.l.]: US Department of Energy Office of Basic Energy Sciences, 2005.

[2] LARSEN, H.; PETERSEN, L. S. *Non-fossil energy technologies in 2050 and beyond.* [S.l.]: Risϕ Energy Report 9, 2010.

[3] KEY World Energy Statistics. [S.l.]: Organisation for Economic Cooperation and Development/International Energy Agency, 2016.

[4] BATTAGLIA, C. et al. High-efficiency crystalline silicon solar cells: status and perspectives. *Energy Environ. Sci.*, v. 9, p. 1552, 2016.

[5] SHOCKLEY, W.; QUEISSER, H. J. Detailed balance limit of efficiency of p-n junction solar cells. *J. Appl. Phys.*, v. 32, p. 510, 1961.

[6] KROGSTRUP, P. et al. Single-nanowire solar cells beyond the shockly-queisser limit. *Nat. Photonics*, v. 7, p. 306–310, 2013.

[7] SAGA, T. Advances in crystalline silicon solar cell technology for industrial mass production. *NPG Asia Mater*, v. 2, p. 96–102, 2010.

[8] KIM, J. et al. 9.4% efficient amorphous silicon solar cell on high aspect-ratio glass microcones. *Adv. Mater.*, v. 26, p. 4082–4086, 2014.

[9] CHIRILA, A. et al. Highly efficient Cu(In,Ga)Se_2 solar cells grown on flexible polymer films. *Nature Materials*, v. 10, p. 857–861, 2011.

[10] WILLIAMS, B. et al. Challenges and prospects for developing CdS/CdTe substrate solar cells on Mo foils. *Solar Energy Materials & Solar Cells*, v. 124, p. 31–38, 2014.

[11] PEREIRA, M. S. et al. Application of Fe-doped SnO_2 nanoparticles in organic solar cells with enhanced stability. *Opt. Mater.*, v. 64, p. 548–556, 2017.

[12] LIU, C. et al. Single-junction polymer solar cells with over 10% efficiency by a novel two-dimensional donor-acceptor conjugated copolymer. *ACS Appl. Mater. Interfaces*, v. 7, p. 4928–4935, 2015.

[13] CHEN, C. et al. An efficient triple-junction polymer solar cell having a power conversion efficiency exceeding 11%. *Adv. Mater.*, v. 26, p. 5670–5677, 2014.

[14] BIRKEL, A. et al. Highly efficient and stable dye-sensitized solar cells based on SnO_2 nanocrystals prepared by microwave-assisted synthesis. *Energy Environ. Sci.*, v. 5, n. 5392, 2012.

[15] WANG, Y. F. et al. Synthesis of hierarchical SnO_2 octahedra with tailorable size and application in dye-sen-sitized solar cells with enhanced power conversion efficiency. *J. Mater. Chem.*, v. 22, p. 21495, 2012.

[16] KRISHNAMOORTHY, T. et al. A facile route to vertically aligned electrospun SnO_2 nanowires on a transparent conducting oxide substrate for dye-sensitized solar cells. *J. Mater. Chem.*, v. 22, p. 2166, 2012.

[17] ZHANG, Q. et al. Small-molecule solar cells with efficiency over 9%. *Nature Photonics*, v. 9, p. 35–41, 2015.

[18] GRÄTZEL, M. The light and shade of perovskite solar cells. *Nat. Mater.*, v. 13, p. 838, 2014.

[19] YANG, W. S. et al. High-performance photovoltaic perovskite layers fabricated through intramolecular exchange. *Science*, v. 1234-1237, p. 348, 2015.

[20] ANDERSEN, T. R. et al. Fully roll-to-roll prepared organic solar cells in normal geometry with a sputter-coated aluminium top-electrode. *Sol. Energy Mater. Sol. Cells*, v. 149, p. 103–109, 2016.

[21] KADUWAL, D. et al. Layout flexibility for sheet-to-sheet produced flexible ITO-free organic solar modules with organic functional layers slot die coated under ambient atmospheric conditions. *Sol. Energy Mater. Sol. Cells*, v. 136, p. 200–205, 2015.

[22] KOCH, S. W. et al. Semiconductor excitons in new light. *Nature Materials*, v. 5, p. 523, 2006.

[23] BARDEEN, C. J. The structure and dynamics of molecular excitons. *Annu. Rev. Phys. Chem.*, v. 65, p. 127–48, 2014.

[24] FRENKEL, J. On the transformation of the light into heat solids. *Phys.l Rev.*, v. 37, p. 17, 1931.

[25] WANNIER, G. H. The structure of electronic excitation levels in insulating crystals. *Phys. Rev.*, v. 52, p. 191, 1937.

[26] BRAZOVSKII, S.; KIROVA, N. Physical theory of excitons in conducting polymers. *Chem. Soc. Rev.*, v. 39, p. 2453–2465, 2010.

[27] POPE, M.; SWENBERG, C. E. *Electronic Processes in Organic Crystals and Polymers*. 2. ed. [S.l.]: Oxford University Press, 1999. (Monographs on the physics and chemistry of materials).

[28] KNOESTER, J.; GRANOVICH, V. M. A. Electronic excitations in organic based nanostructures. In: _____. [S.l.]: Elsevier Inc., 2003. v. 31, cap. Frenkel and Charge-Transfer Excitons in Organic Solids, p. 1–96.

[29] ROCCA, G. C. L. Electronic excitations in organic based nanostructures. In: _____. [S.l.]: Elsevier Inc., 2003. v. 31, cap. Wannier-Mott Excitons in Semiconductors, p. 97–128.

[30] RLE CENTER FOR EXCITONICS, MASSACHUSETTS INSTITUTE OF TECHNOLOGY. 2017. Online – accessed June 20, 2017. Available at: <http://eecs-newsletter.mit.edu/tags/excitons/>.

[31] MIKHNENKO, O. V. et al. Exciton diffusion in organic semiconductors. *Energy Environ. Sci.*, v. 8, p. 1867, 2015.

[32] KÖHLER, A.; BÄSSLER, H. Triplet states in organic semiconductors. *Mater. Sci. Eng.*, v. 66, p. 71–109, 2009.

[33] GONZÁLEZ, D. M. et al. Improved power conversion efficiency of P3HT:PCBM organic solar cells by strong spin-orbit coupling-induced delayed fluorescence. *Adv. Energy Mater.*, v. 5, p. 1401770, 2015.

[34] DEIBEL, C. Quantum efficiency in complex systems, part ii: From molecular aggregates to organic solar cells. In: _____. *Quantum Efficiency in Complex Systems, Part II From Molecular Aggregates to Organic Solar Cells*. [S.l.]: Elsevier, 2011. v. 85, cap. Photocurrent Generation in Organic Solar Cells, p. 297 – 330.

[35] FERON, K. et al. Organic solar cells: Understanding the role of Forster resonance energy transfer. *Int. J. Mol. Sci.*, v. 13, p. 17020, 2012.

[36] YAO, E.-P. et al. An investigation of organic photovoltaics improvement via extension of the exciton lifetime,. *Phys. Chem. Chem. Phys.*, v. 17, p. 5826, 2015.

[37] SCULLY, S. R.; MCGEHEE, M. D. Effects of optical interference and energy transfer on exciton diffusion length measurements in organic semiconductors. *J. Appl. Phys.*, v. 100, p. 034907–1, 2006.

[38] KIM, Y.; BRADLEY, D. Bright red emission from single layer polymer light-emitting devices based on blends of regioregular P3HT and F8BT. *Curr. Appl. Phys.*, v. 5, p. 222–226, 2005.

[39] MIKHNENKO, O. V. et al. Direct measurement of the triplet exciton diffusion length in organic semiconductors. *Phys. Rev. Lett.*, v. 108, p. 137401, 2012.

[40] XU, B.; HOLDCROFL, S. Phosphorescence and delayed fluorescence of poly(3-hexylthiophene) films. *Thin Solid Films*, v. 242, p. 174, 1994.

[41] SERVAITES, J. D. et al. Organic solar cells: A new look at traditional models. *Energy Environ. Sci.*, v. 4, p. 4410, 2011.

[42] HAINS, A. W. et al. Molecular semiconductors in organic photovoltaic cells. *Chem. Rev.*, v. 110, p. 6689, 2010.

[43] ELUMALAI, N. K.; UDDIN, A. Open circuit voltage of organic solar cells: an in-depth review. *Energy Environ. Sci.*, v. 9, p. 391, 2016.

[44] NELSON, J. *The Physics of Solar Cells*. London, England: Imperial College Press, 2003.

[45] SIGNERSKI, R. On the light intensity dependence of short-circuit current of bilayer organic photovoltaic cells. *J. Non-Cryst. Solids*, v. 354, p. 4465–4468, 2008.

[46] SHROTRIYA, V. et al. Accurate measurement and characterization of organic solar cells. *Adv. Funct. Mater.*, v. 16, p. 2016–2023, 2006.

[47] HAGFELDT, A. et al. Dye-sensitized solar cells. *Chem. Rev.*, v. 110, p. 6595–6663, 2010.

[48] O'REGAN, B.; GRÄTZEL, M. A low-cost, high-efficiency solar cell based on dye-sensitized colloidal TiO_2 films. *Nature*, 1991.

[49] FAN, J. et al. Dye-sensitized solar cells based on TiO_2 nanoparticles/nanobelts ouble-layered film with improved photovoltaic performance. *Appl. Surf. Sci.*, v. 319, p. 75–82, 2014.

[50] LIMA, F. A. S. et al. Electrochemically synthesized mesoporous thin films of ZnO for highly efficient dye sensitized solar cells. *Ceram. Int.*, v. 41, p. 9314–9320, 2015.

[51] HARDIN, B. E. et al. The renaissance of dye-sensitized solar cells. *Nature Photonics*, v. 6, p. 162–169, 2012.

[52] BOSCHLOO, G.; HAGFELDT, A. Characteristics of the iodide/triiodide redox mediator in dye-sensitized solar cells. *Acc. Chem. Rec.*, v. 42, p. 1819–1826, 2009.

[53] WANG, N. et al. Photodegradation of small-molecule organic photovoltaics. *Sol. Energ. Mat. Sol. Cells*, v. 125, p. 170–175, 2014.

[54] FACCHETTI, A. Polymer donor-polymer acceptor (all-polymer) solar cells. *Materials Today*, v. 16, p. 123, 2013.

[55] SHIRAKAWA, H. et al. Synthesis of electrically conducting organic polymers: Halogen derivatives of polyacetylene, $(CH)_x$. *J. Chem. Soc., Chem. Commun.*, v. 16, p. 578–580, 1977.

[56] KALTENBRUNNER, M. et al. Ultrathin and lightweight organic solar cells with high flexibility. *nature communications*, v. 3, p. 770, 2012.

[57] REINEKE, S. et al. White organic light-emitting diodes with fluorescent tube efficiency. *Nature*, v. 459, p. 234, 2009.

[58] HEDLEY, G. J. et al. Light harvesting for organic photovoltaics. *Chem. Rev.*, v. 117, p. 796–837, 2017.

[59] KOVALENKO, A. et al. Towards improved efficiency of bulk-heterojunction solar cells using various spinel ferrite magnetic nanoparticles. *Organic Electronics*, v. 39, p. 118–126, 2016.

[60] TÉRAN-ESCOBAR, G. et al. Low-temperature, solution-processed, layered V_2O_5 hydrate as the hole-transport layer for stable organic solar cells. *Energy Environ. Sci.*, v. 6, p. 3088, 2013.

[61] HE, Z. et al. Enhanced power-conversion efficiency in polymer solar cells using an inverted device structure. *Nature Photonics*, v. 6, p. 591, 2012.

[62] TROST, S. et al. Avoiding photoinduced shunts in organic solar cells by the use of tin oxide (SnO_x) as electron extraction material instead of ZnO. *Adv. Energy Mater.*, v. 6, p. 1600347, 2016.

[63] MORAIS, A. et al. Enhanced photovoltaic performance of inverted hybrid bulk heterojunction solar cells using TiO_2/reduced graphene oxide films as electron transport layers. *J. Photonics Energy*, v. 5, p. 057408, 2015.

[64] SU, Y. W. et al. Organic photovoltaics. *Materials today*, v. 15, p. 554, 2012.

[65] FORREST, S. R. The path to ubiquitous and low-cost organic electronic appliances on plastic. *Nature*, v. 428, p. 911, 2004.

[66] DEIBEL, C.; DYAKONOV, V. Polymer–fullerene bulk heterojunction solar cells. *Rep. Prog. Phys. 73*, v. 73, p. 1–40, 2010.

[67] YAO, Y. et al. Ultrafast long-range charge separation in organic photovoltaics: Promotion by off-diagonal vibronic couplings and entropy increase. *J. Phys. Chem. Lett.*, v. 7, p. 4830–4835, 2016.

[68] FORREST, S. R. T he limits to organic photovoltaic cell efficiency. *MRS Bulletin*, v. 30, p. 28–32, 2005.

[69] YAN, J.; SAUNDERS, B. R. Third-generation solar cells: a review and comparison of polymer:fullerene, hybrid polymer and perovskite solar cells. *RSC Adv.*, v. 4, p. 43286, 2014.

[70] MAZZIO, K. A.; LUSCOMBE, C. K. The future of organic photovoltaics. *Chem. Soc. Rev.*, v. 44, p. 78, 2015.

[71] HE, Z. et al. Simultaneous enhancement of open-circuit voltage, short-circuit current density, and fill factor in polymer solar cells. *Adv. Mater.*, v. 23, p. 4636–4643, 2011.

[72] BARTESAGHI, D. et al. Competition between recombination and extraction of free charges determines the fill factor of organic solar cells. *Nat. Commun.*, v. 6, p. 7083, 2015.

[73] SALZMANN, I.; HEIMEL, G. Toward a comprehensive understanding of molecular doping organic semiconductors (review). *J. Electron Spectrosc. Relat. Phenom.*, v. 204, p. 208–222, 2015.

[74] WALZER, K. et al. Highly efficient organic devices based on electrically doped transport layers. *Chem. Rev.*, v. 107, p. 1233–1271, 2007.

[75] COROPCEANU, V. et al. Charge transport in organic semiconductors. *Chem. Rev.*, v. 107, p. 926–952, 2007.

[76] WANG, K. et al. Effects of magnetic nanoparticles and external magnetostatic field on the bulk heterojunction polymer solar cells. *Scientific Reports*, v. 5, p. 9265, 2015.

[77] CHEN, S. et al. Metal oxides for interface engineering in polymer solar cells. *J. Mater. Chem.*, v. 22, p. 24202–24212, 2012.

[78] STEIM, R. et al. Interface materials for organic solar cells. *J. Mater. Chem.*, v. 20, p. 2499–2512, 2010.

[79] CHANG, C. H. et al. Thermodynamic stability of SnO_2 nanoparticles: The role of interface energies and dopants. *J. Phys. Chem. C*, v. 119, p. 6389–6397, 2015.

[80] PRIYA, S. M. et al. Structural, morphological and optical properties of tin oxide nanoparticles synthesized by sol-gel method adding hydrochloric acid. *J. Sol-Gel Sci. Technol.*, v. 78, p. 365–372, 2016.

[81] RECHBERGER, F. et al. Strategies to improve the electrical conductivity of nanoparticle-based antimony-doped tin oxide aerogels. *J. Sol-Gel Sci. Technol.*, v. 80, p. 660–666, 2016.

[82] BELTRÁN, J. J. et al. Crystallographic and magnetic properties of Fe-doped SnO_2 nanopowders obtained by a sol–gel method. *J. Mater. Sci.*, v. 45, p. 5002–5011, 2010.

[83] DIÉGUEZ, A. et al. The complete raman spectrum of nanometric SnO_2 particles. *J. Appl. Phys.*, v. 90, p. 1557, 2001.

[84] PAL, M. et al. Sol-gel based simonkolleite nanopetals with SnO_2 nanoparticles in graphite-like amorphous carbon as an efficient and reusable photocatalyst. *RSC Adv.*, v. 5, p. 75062, 2015.

[85] SUN, J. et al. Growth of SnO_2 nanowire arrays by ultrasonic spray pyrolysis and their gas sensing performance. *RSC Adv.*, v. 4, p. 43429, 2014.

[86] MEI, L. et al. Gas sensing of SnO_2 nanocrystals revisited: Developing ultra-sensitive sensors for detecting the H_2S leakage of biogas. *Scientific Reports*, v. 4, p. 6028, 2013.

[87] MUELLER, F. et al. Fe-doped SnO_2 nanoparticles as new high capacity anode material for secondary lithium-ion batteries. *J. Power Sources*, v. 299, p. 398–402, 2015.

[88] FUKUMURA, T. et al. Exploration of oxide-based diluted magnetic semiconductorstoward transparent spintronics. *Appl. Surf. Sci.*, v. 223, p. 62–67, 2004.

[89] OHNO, H. A window on the future of spintronics. *Nature Materials*, v. 9, p. 952, 2010.

[90] OGANISIAN, K. et al. Synthesis of iron doped titanium dioxide by sol-gel method for magnetic applications. *Proc. Appl. Ceram.*, v. 9, p. 43–51, 2015.

[91] MATSUMOTO, Y. et al. Room-temperature ferromagnetism in transparent transition metal-doped titanium dioxide. *Science*, v. 291, p. 854–856, 2001.

[92] UEDA, K. et al. Magnetic and electric properties of transition-metal-doped ZnO films. *Appl. Phys. Lett.*, v. 79, p. 988, 2001.

[93] OGALE, S. B. et al. High temperature ferromagnetism with a giant magnetic moment in transparent Co-doped $SnO_{2-\delta}$. *Phys. Rev. Lett.*, v. 91, p. 77205, 2003.

[94] BELTRÁN, J. J. et al. Understanding the role of iron in the magnetism of fe doped zno nanoparticles. *Phys. Chem. Chem. Phys.*, v. 17, p. 15284, 2015.

[95] ARAGÓN, F. H. et al. Fe doping effect on the structural, magnetic and surface properties of SnO_2 nanoparticles prepared by a polymer precursor method. *J. Phys. D: Appl. Phys.*, v. 49, p. 155002, 2016.

[96] CHOUDHURY, B. et al. Oxygen defect assisted paramagnetic to ferromagnetic conversion in fe doped TiO_2 nanoparticles. *RSC Adv.*, v. 4, p. 29314–29323, 2014.

[97] HARRIS, V. G. Modern microwave ferrites. *IEEE Transactions on Magnetics*, v. 48, p. 1075–1104, 2012.

[98] VALENZUELA, R. Novel applications of ferrites. *Physics Research International*, v. 2012, p. 9, 2012.

[99] PACAKOVA, B. et al. Magnetic spinels-synthesis, properties and applications. In: _____. [S.l.]: InTec, 2017. cap. Spinel Ferrite Nanoparticles: Correlation of Structure and Magnetism.

[100] SUTKA, A.; MEZINSKIS, G. Sol-gel auto-combustion synthesis of spinel-type ferrite nanomaterials. *Front. Mater. Sci.*, v. 6, p. 128, 2012.

[101] KANAGESAN, S. et al. Synthesis, characterization and in vitro evaluation of manganese ferrite ($MnFe_2O_4$) nanoparticles for their biocompatibility with murine breast cancer cells (4T1). *Molecules*, v. 21, p. 312, 2016.

[102] ZHANG, L.; WU, Y. Sol-gel synthesized magnetic $MnFe_2O_4$ spinel ferrite nanoparticles as novel catalyst for oxidative degradation of methyl orange. *Journal of Nanomaterials*, v. 2013, p. 6 pages, 2013.

[103] VIGNESH, R. H. et al. Synthesis and characterization of $MnFe_2O_4$ nanoparticles for impedometric ammonia gas sensor. *Sens. Actuat. B Chem.*, v. 220, p. 50–58, 2015.

3. STRUCTURAL, MORPHOLOGICAL AND OPTICAL PROPERTIES OF SnO_2 NANOPARTICLES OBTAINED BY A PROTEIC SOL-GEL METHOD AND THEIR APPLICATION IN DYE-SENSITIZED SOLAR CELLS

Tin dioxide nanoparticles were synthesized by the proteic sol-gel method. Tin chloride ($SnCl_4 \cdot 5H_2O$) was used as source of Sn^{4+} and commercial gelatin as organic precursor. Several calcination temperatures were employed. Thermogravimetric analysis and differential scanning calorimetry were performed to investigate the thermal behavior of the precursor powders as well as to select the appropriate calcination temperatures for oxide formation. Structural, morphological and optical properties of the synthesized materials were studied by X-ray diffraction, transmission electron microscopy, Fourier transformed infrared spectroscopy, and ultraviolet-visible spectroscopy. The results confirmed the formation of spherical nanoparticles of rutile SnO_2 with an optical absorption band in the ultraviolet region near the visible light range. Thermally treated samples showed improved crystallinity and superior transparency to visible light. These SnO_2 nanoparticles were successfully employed as photoanode material in dye-sensitized solar cells. The performance of the cells was evaluated by measuring J×V curves in a solar simulator and was found to be in line with results in the literature.

3.1 Introduction

Tin dioxide (SnO_2) is a typical wide band gap n-type semiconductor with direct band gap of about 3.6 eV at room temperature. It is one of the most widely used semiconductor oxide due to its chemical and mechanical stability [1] and excellent optical and electrical properties [2, 3]. It has a rutile-type tetragonal crystal structure with a $P4_2/mnm$ space

group [4, 5]. Its unit cell consists of two Sn^{4+} and four O^{2-} ions with each tin cation coordinated by six oxygen anions in the corners of a regular octahedron. Each oxygen anion is surrounded by three Sn^{4+} ions which approximate the corners of an equilateral triangle [5]. Tin oxide has many technological applications such as in solar cells [6–8], photocatalytical activity [9], gas sensors of toxic materials [10, 11], liquid crystal displays and anodes for lithium ion batteries [12].

The synthesis of SnO_2 nanoparticles has been carried out by different methods such as solid-state reaction methods [13], chemical precipitation [14, 15], conventional sol-gel [16, 17], among others. Sol-gel methods present several advantages over other methods such as a potential to produce high purity compounds with homogeneity at the atomic scale, as well as a significant reduction of required processing times and temperatures.

The proteic sol-gel [18] method used in this work is a variation of the conventional method that employs edible gelatin or coconut water as organic precursor for oxide formation. This method has been successfully employed in the synthesis of nanometric semiconducting materials with potential use in various technological applications [19–21]. As it uses low cost reagents like metal nitrates and chlorides, this method is relatively simple and cost efficient.

The synthesis by the proteic sol-gel method consists of four stages: dissociation of metal ions from precursor salts; formation of metal-gelatin chelates; drying; and calcination. In the first stage metal ions are dissociated from the precursor salts in distilled water. The solution with dissociated ions is put in contact with the gelatin to form metal chelates where metal ions join the functional groups (amino acids) of the gelatin. The drying stage is employed to remove water and form a puffy polymeric substance. Finally, calcination is performed to remove organic matter with formation of the desired compound. When calcination is done in open air, oxides of the metallic ions are formed. Calcination temperatures are generally just low enough to evaporate the organic matter without affecting the outcome of the reaction.

This chapter presents structural, morphological and optical characterization of SnO_2 nanoparticles produced by the proteic sol-gel method. The material was applied as photoanode in dye-sensitized solar cells to demonstrate its technological viability.

3.2 Experimental procedure

The entire process of nanoparticles synthesis and DSSC building is schematically represented in Fig. 3.1 and described below.

Figure 3.1: Schematic representation of nanoparticles synthesis and DSSC building.

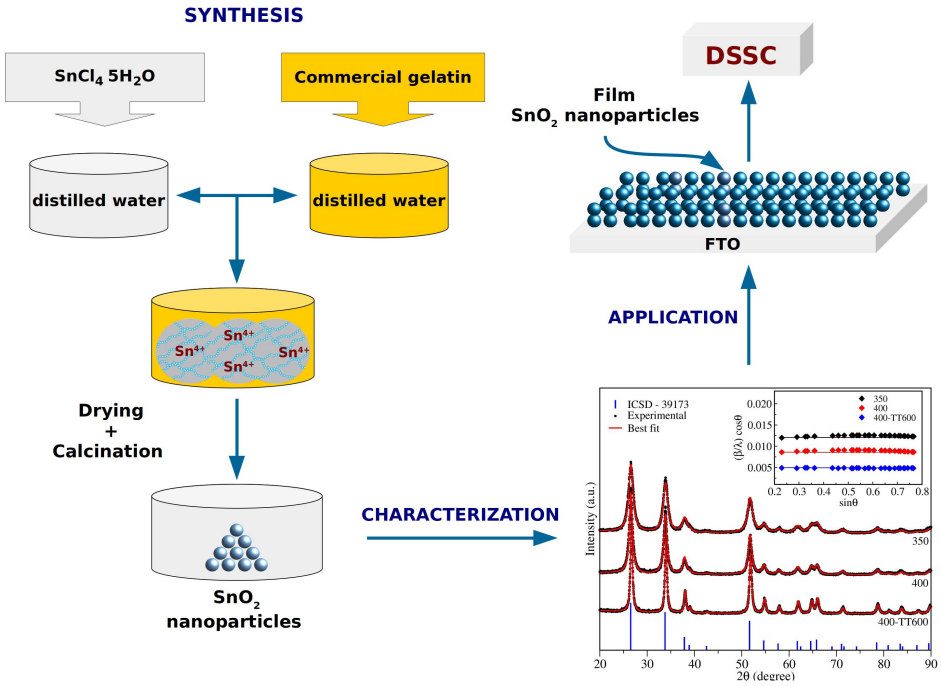

Source: Own author

3.2.1 Nanoparticles synthesis and characterization

Samples of nanoparticulated SnO_2 were prepared by the proteic sol-gel method [18]. $SnCl_4 \cdot 5H_2O$ was employed as source of Sn^{4+} ions and commercial gelatin as organic precursor. In a typical procedure, two separate solutions were produced by dissolving

10 g of $SnCl_4 \cdot 5H_2O$ and 5 g of commercial gelatin in 10 mL and 20 mL, respectively, of distilled water, and stirred for 60 min in room temperature. Both solutions were added together under continuous stirring at temperature of 40 °C for 10 h to promote polyesterification. This mixture was then dried at 150 °C in air during 24 h to remove volatile components, resulting in a black solid puffy mass, referred to in this text as the precursor powder.

The precursor powder was calcined at 350 and 400 °C (at a heating rate of 5 °C/min) in air atmosphere for 4 h, resulting in the SnO_2 nanoparticles. The sample calcined at 400 °C was submitted to a thermal treatment at 600 °C in air atmosphere for 2 h in order to eliminate residual organic matter. These samples are referred to throughout this work as 350, 400 and 400–TT600, respectively.

Thermogravimetric analysis (TGA) and differential scanning calorimetry (DSC) were performed using a NETZSCH STA 449F3 Jupiter thermal analysis equipment. Measurements were performed under air atmosphere with heating hate of 5 °C/min.

X-ray diffraction (XRD) patterns were collected at room temperature using a Rigaku DMAXB diffractometer operating with a Kα-Cu source ($\lambda = 1.54$ Å) at 40 kV and 30 mA. The pattens were Rietveld refined [22, 23] using the program GSAS [24] and based in the SnO_2 standard crystal structure cataloged by the Inorganic Crystal Structure Database under number 39173 (ICSD-39173).

Transmission electron microscopy (TEM) were performed using a 200 kV JEM 2011 microscope. Fourier transformed infrared (FTIR) absorption spectra were collected at room temperature in transmission mode using a Bruker Vertex 70 spectrometer. Ultraviolet-visible (UV-vis) spectroscopy was carried out at room temperature using a UV 2600 Shimadzu spectrophotometer coupled to an integrating sphere ISR 2600 Plus. Scanning electron microscopy (SEM) of photoanode films was performed in air under ambient conditions using a Quanta FEG 450 microscope.

3.2.2 Solar cells construction and characterization

400-TT600 nanoparticles were used as photoanode in the production of dye-sensitized solar cells (DSSCs). An amount of 250 mg of SnO_2 nanoparticles were dispersed in a mixture of ethanol (0.5 ml), Triton-X-100 (2 drops), acetic acid (0.02 ml) and isopropanol (0.25 ml). The solution was placed in an ultrasonic bath for 1 h, and subsequently kept under stirring at room temperature for 24 h. A SnO_2 photoanode was prepared using the spin coating method with the prepared semiconductor solution applied on a FTO substrate. The photoanode was then sintered at 450 °C for 30 min. The SnO_2 electrodes prepared as described above were dipped into a solution of N719 dye in acetonitril for 24 h at room temperature and then rinsed with ethanol and dried under a nitrogen gas flow. The dye-adsorbed SnO_2 electrode and Pt-counter electrode were assembled into a sandwich-type cell and sealed with a hot-melt film. The electrolyte (Iodolyte AN-50) was inserted through a hole that was sealed using the hot-melt film.

Solar simulations were performed using a Steuernagel Solarkonstant KHS1200 solar simulator under simulated AM 1.5 solar illumination at 100 mW/cm^2. J×V curves were measured using a Keithley 2601 multimeter.

3.3 Results and discussion

Thermal analysis was performed in order to study the thermal decomposition of the materials and to select the appropriate temperatures of oxide formation and thermal treatment. Figure 3.2 shows TGA/DSC curves obtained from the precursor powder and SnO_2 samples calcined at 400 °C before and after thermal treatment.

The thermal behavior of the precursor powder may be divided into three main stages as indicated in Fig. 3.2a. The first one occurs in the 200–300 °C range and can be attributed to the thermal degradation of gelatin chains. This reaction is characterized by an endothermic peak at about 250 °C in the DSC scan and is responsible for the loss of about 40% of the sample mass. The second stage occurs between 300–450 °C where the sharp DSC exothermic peak at about 370 °C is attributed to the formation of SnO_2 [10, 25]. Some organic matter is decomposed in this stage as the TGA curve

shows an approximate loss of 20% of mass. The third and last stage takes place in the temperature range of 450–700 °C. The exothermic peak around 580 °C is due to carbonate decomposition releasing carbonyl groups [25–27]. Another 20% of mass is lost in this stage adding up to a total of 80% of mass loss in the entire process.

Figure 3.2: TGA/DSC curves of (a) precursor powder, (b) sample 400 and (c) sample 400-TT600.

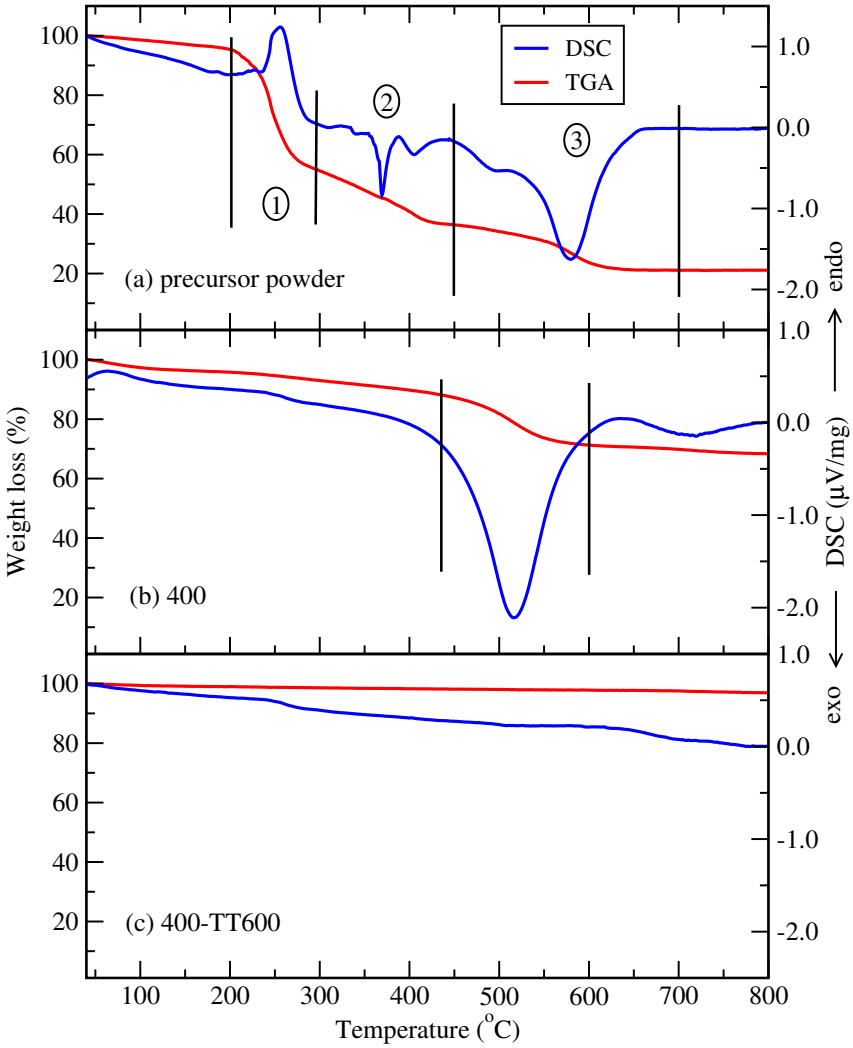

Source: Own author

These results suggest that SnO_2 formation occurs at temperatures between 350–400 °C. The thermal analysis of a sample calcined at 400 °C for 4 h is showed in Fig. 3.2b. A single thermal event, responsible for a 15% moss loss, is observed in the 450–600 °C range. The

broad exothermic peak at around 515 °C is attributed to the formation and evaporation of CO_2 [25–27]. This result indicates that the calcination process did not eliminate the organic matter entirely. This sample was then treated at 600 °C for 2 h and its thermal behavior is shown in Fig. 3.2c. The DSC shows no endo or exothermic processes and the TGA shows no mass loss, confirming that all organic matter has been eliminated by the thermal treatment.

Figure 3.3 shows X-ray diffraction patterns of SnO_2 samples. All diffractograms show peaks that match the ICSD-39173 reference pattern relative to the tetragonal crystal structure of SnO_2 (bars in the figure). No other crystalline phase was found.

Figure 3.3: X-ray diffraction patterns of SnO_2 samples 350, 400 and 400–TT600. Dots and solid lines are the experimental data and best fit respectively. Bars represent the ICSD-39173 standard pattern. Insert: Williamson-Hall curves.

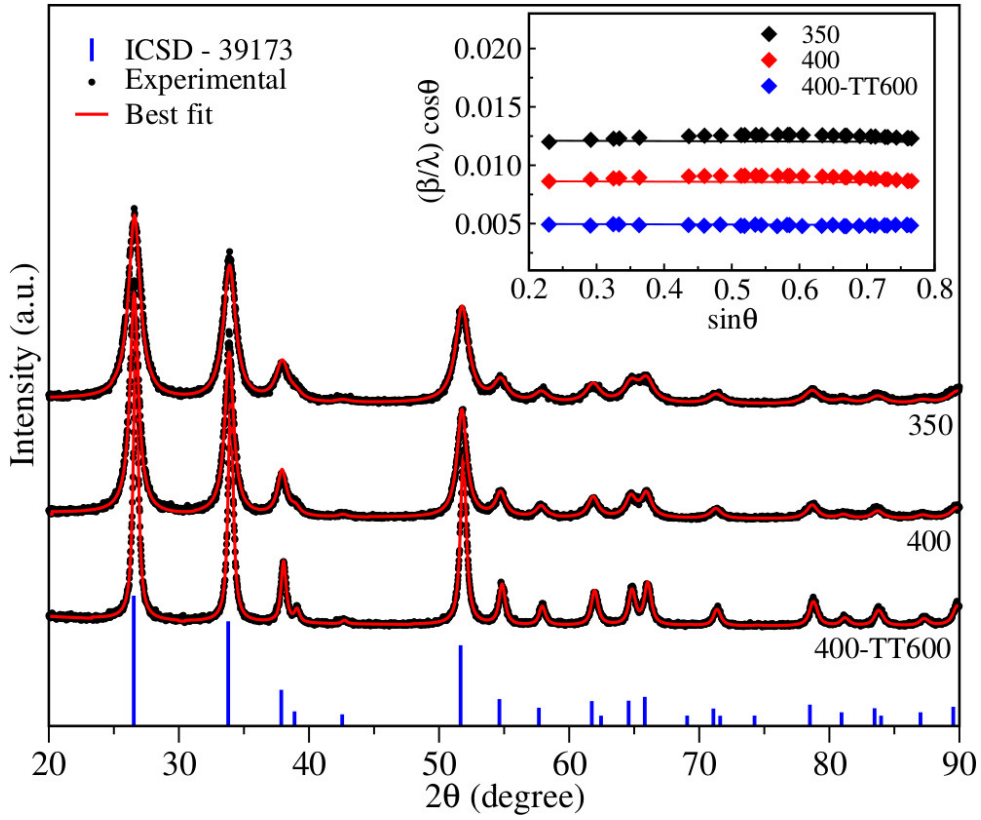

Source: Own author

The patterns were Rietveld refined and the best fits are shown as solid red lines. Williamson-Hall curves [28] are shown in the inset of Fig. 3.3. Table 3.1 shows lattice parameter, unit cell volume, and crystallite average size.

Table 3.1: Lattice parameters, unit cell volume, average crystallite size and microstrain of SnO_2 samples 350, 400 and 400-TT600.

sample	$a = b$ (Å)	c (Å)	volume (Å^3)	D_S (nm)	D_{WH} (nm)	ϵ (%)
350	4.740	3.185	71.55	8.1	8.2	0.01
400	4.738	3.185	71.52	11.0	11.0	-0.01
400–TT600	4.743	3.189	71.75	20.6	20.3	-0.04

Source: Own author

The crystallite average sizes were calculated by the Scherrer formula (D_S)

$$D_S = \frac{k\,\lambda}{\beta\,cos\,\theta}\,, \tag{3.1}$$

where λ is the radiation wavelength, θ is the diffraction angle and, k is a constant related to the shape of particles, and corrected by the Williamson-Hall method (D_{WH}) after compensating for residual microstrain (ϵ) [28] using the expression:

$$\frac{\beta\cos\theta}{\lambda} \;=\; \frac{k}{D_{WH}} + \frac{4\epsilon}{\lambda}\sin\theta, \tag{3.2}$$

where β is the measured peak width - corrected for instrumental line broadening.

Lattice parameters (and unit cell volume) values are virtually the same for all samples. All samples showed crystallite size in the nanometer range (8 to 20 nm) with negligible levels of microstrain. The thermal treatment led to an increase of particle size from 11 (sample 400) to about 20 nm (sample 400-TT600). Sample homogeneity improved with thermal treatment as the Williamson-Hall curve of the 400-TT600 sample is more akin to a straight line.

Figure 3.4 shows TEM images (two different magnifications) of a SnO_2 sample calcined at 350 °C. It can be seen that SnO_2 nanoparticles have an approximate spherical morphology with an average diameter between 5–10 nm, in agreement with the sizes obtained from the XRD data.

A zoomed-in image of a nanoparticle is shown on the inset of Fig. 3.4a. The selected area of electron diffraction (SAED) pattern of the sample is shown on the inset of Fig. 3.4b. The interplanar distance shown in Fig. 3.4a was estimated as approximately 0.33±0.02 nm, which corresponds to the {110} diffraction planes of the rutile-type structure. It is worth mentioning that these diffraction planes are commonly found in nanosized SnO_2 systems. These values are in agreement with those reported in the literature [9, 29]

Figure 3.4: TEM images (two different magnifications) of SnO_2 nanoparticles calcined at 350 °C. Inset: A zoomed-in image of a nanoparticle and corresponding selected area electron diffraction (SAED) pattern.

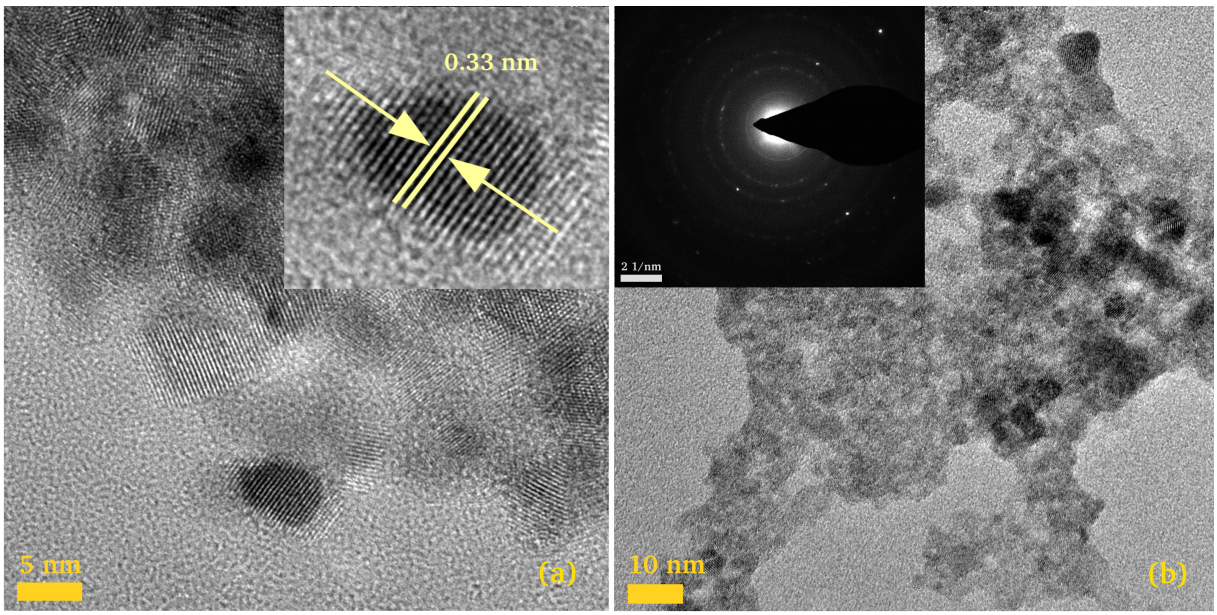

Source: Own author

FTIR spectra of the precursor powder and SnO_2 nanoparticles are shown in Fig. 3.5. The precursor powder spectrum exhibits absorption bands in a wide range attributed to gelatin. The absorption peak at 890 cm^{-1} is assigned to C–H bending modes in alkene groups [30]. The peaks at 1405 and 1478 cm^{-1} are attributed to C–O and N–H vibration bands, respectively [30–32]. The broad absorption region in the range 1360–1760 cm^{-1}, centered at 1572 cm^{-1}, is assigned to overlapping vibration modes of carboxylic, alkene and amine groups (C=O, C=C and N−H) present in gelatin [30–33]. The peak appearing at around 1105 cm^{-1} is attributed to the vibration of the hydroxyl-tin (Sn–OH) bond [2, 34]. The broad absorption bands centered at 1740 cm^{-1} and 3160 cm^{-1} are attributed, respectively, to bending and stretching vibrations of hydroxyl groups of water molecules.

Figure 3.5: FTIR spectra of the precursor powder and SnO_2 samples 350, 400 and 400–TT600.

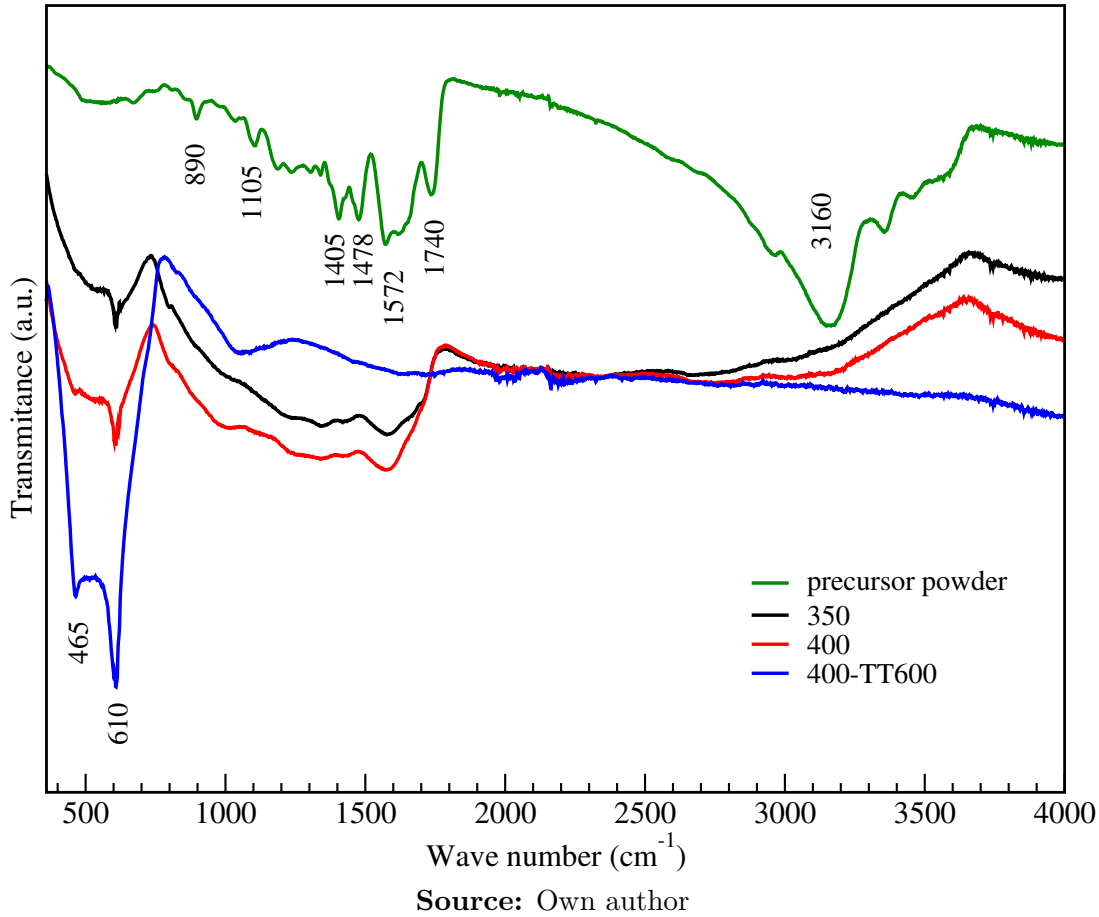

Source: Own author

FTIR spectra of SnO_2 nanoparticles show intense absorption bands at a lower wave number range of 465–610 cm^{-1} characteristics of Sn–O stretching modes expected for crystalline SnO_2 [33, 35–37]. The spectrum for the 400–TT600 sample presents narrower band widths and larger intensities attributed to the improvement in crystallinity due to the removal of residual organic matter.

Samples 350 and 400 spectra present a region of overlapped broadened bands between 800 and 1750 cm^{-1} resulting from vibrations of functional groups present in the gelatin still remaining after calcination. These bands are absent from the spectrum of the 400–TT600 sample providing further confirmation that all residual organic matter has been eliminated by the thermal treatment. The 1740 and 3160 cm^{-1} bands attributed to water molecules are absent from all calcined samples spectra.

UV-vis absorbance spectra of SnO_2 samples are shown in Fig. 3.6. The curves display an absorption band in the ultraviolet region near the visible light range. The samples 350 and 400 are translucent and exhibit a dark color due to the presence of residual organic material from the synthesis. As expected, the sample 400–TT600 showed superior transparency to visible light due to the absence of organic matter.

As the absorbance spectra of these nanoparticles do not show very sharp absorption edges, the point of inflection obtained from the maximum of the first derivative can be considered to represent the absorption edge [38]. Therefore, energy band gaps were estimated by taking the maximum of the first derivative of each absorbance spectrum (shown in the inset of Fig. 3.6). The band gap of samples 350 and 400 was estimated as 3.92 eV and of sample 400–TT600 as 3.85 eV. This slight narrowing of the band gap is due to improved crystallinity and increased crystallite size of 400–TT600 nanoparticles.

High transmittance in the visible and large electron mobility are two characteristics of a material that makes it suitable to be used as photoanode in DSSCs. The results showed that the 400–TT600 nanoparticles have better crystallinity and are free of residual organic matter and thus are expected to have improved electron mobility when compared to the 350 and 400 nanoparticles. Moreover, UV-vis results showed superior transparency of 400–TT600 nanoparticles in the visible region of the electromagnetic spectrum. Therefore, the

400–TT600 nanoparticles were chosen to be used as photoanode in the construction of DSSCs.

Figure 3.6: UV-Vis absorbance spectra of SnO_2 samples 350, 400 and 400–TT600. Inset: first derivative with arrows identifying the points of maxima.

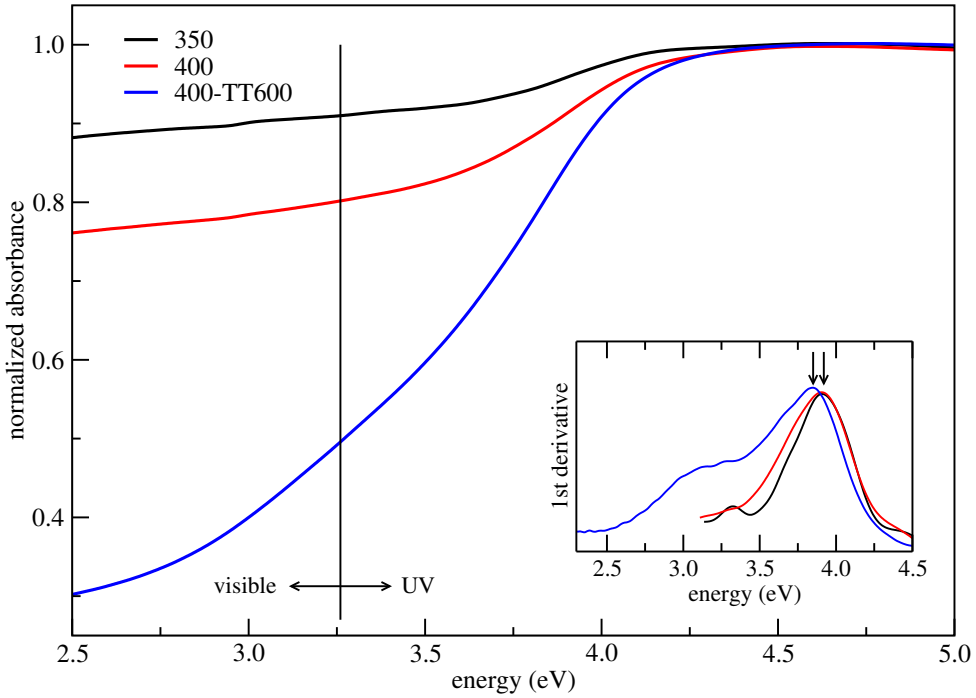

Source: Own author

Figure 3.7 shows SEM images of a SnO_2 photoanode film after the dye-loading. Upon deposition, nanoparticles form micrometer-sized agglomerates as can be observed on the top-view image showed in Fig. 3.7a. Film thickness was estimated from the cross-sectional-view image showed in Fig. 3.7b and was found to be larger than 100 μm. Voids in the film with a few micrometers can also be observed.

Figure 3.7: SEM images of a SnO_2 photoanode film from: (a) top view and (b) cross sectional view after the dye-loading.

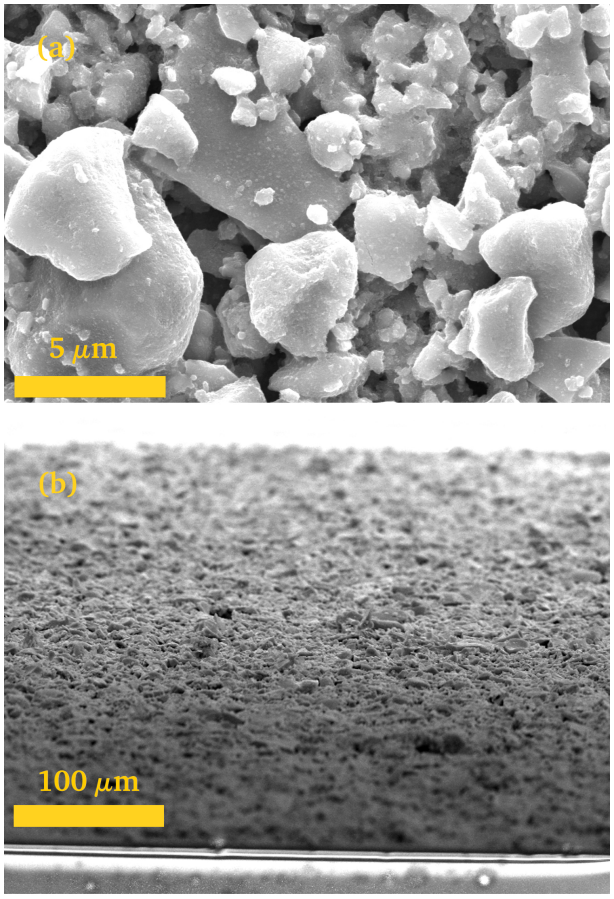

Source: Own author

A total of five devices were manufactured. The devices were built with an active area of 0.20 cm^2. The photovoltaic performance of DSSCs based on SnO_2 photoanodes was characterized by current vs. voltage (J×V) measurements under solar simulation. The J×V curve of the best device is shown in Fig. 3.8. Photovoltaic parameters are listed in Table 3.2.

The photovoltaic parameters in DSSCs depends on several factors such as adsorption of the dye by the photoanode material [8, 39] and thickness of the photoanode film [39]. Agglomeration of nanoparticles implies in less active area for dye adsorption, which can result in fewer photoinduced charge carriers with consequent lower short-circuit current. The use of thick films as photoanode can increase series resistance (R_s) values which leads to increased recombination, which can be associated with low fill factor (FF). All these factors together may lead to modest values of power conversion efficiency (η). Despite

this shortcoming, the best value of η of 0.53% obtained in this work is similar to values recently reported by other research groups [40].

Figure 3.8: J×V curve of the best DSSC using SnO_2 nanoparticles as photoanode. Under simulated AM 1.5 solar illumination at 100 mW/cm^2.

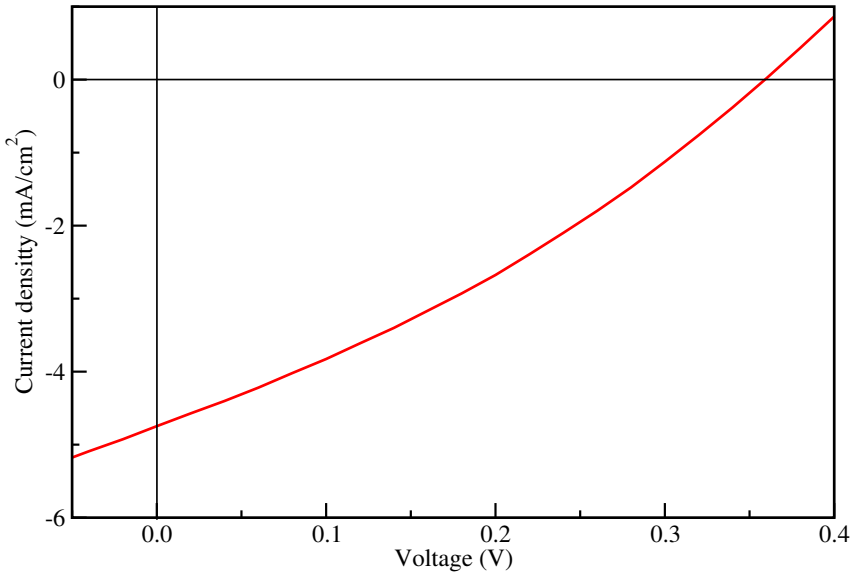

Source: Own author

Table 3.2: Photovoltaic parameters of DSSCs employing SnO_2 nanoparticles as photoanodes. J_{sc}, V_{oc}, FF, η, R_s and R_{sh} are short-circuit current density, open-circuit voltage, fill factor and power conversion efficiency, serie resistance and shunt resistance, respectively. Under simulated AM 1.5 solar illumination at 100 mW/cm^2.

Devices	J_{sc} (mA/cm^2)	V_{oc} (V)	FF (%)	η (%)	R_s (Ωcm^2)	R_{sh} (Ωcm^2)
D1	4.74	0.36	31.40	0.53	19	114
D2	3.42	0.40	33.67	0.45	63	313
D3	3.80	0.31	26.00	0.30	74	86
D4	3.54	0.30	29.00	0.30	41	116
D5	2.60	0.30	31.00	0.25	39	180
avg	3.62 ± 0.3	0.34 ± 0.04	30.20 ± 3	0.36 ± 0.1	47 ± 2	162 ± 104

Source: Own author

3.4 Conclusion

SnO_2 nanoparticles were successfully synthesized using a proteic sol-gel method and applied as photoanode in DSSCs.

Thermal analysis suggested SnO_2 formation at temperatures between 350–400 °C. Thermal results showed the presence of residual organic matter not eliminated by the calcination process. A thermal treatment at 600 °C was shown to be efficient to eliminate this residual organic matter. FTIR and UV-vis results confirmed these findings. XRD results for all samples showed the presence of a single rutile SnO_2 nanostructured phase (crystallite size in the range 8 to 20 nm with negligible levels of microstrain). TEM results showed nanoparticles with spherical shape and average diameter between 5–10 nm.

FTIR, Williamson-Hall and UV-vis results showed that the thermally treated samples presented improved crystallinity and superior transparency to visible light. Therefore, these nanoparticles were chosen to be used as photoanodes in the construction of DSSCs that presented photovoltaic parameters consistent with results obtained from similar cells and reported in the literature.

The present work represents an evolution in the production of nanoparticles by an alternative sol-gel process and represents a promising path to applications in emerging technologies.

3.5 References

[1] CHANG, C. H. et al. Thermodynamic stability of SnO_2 nanoparticles: The role of interface energies and dopants. *J. Phys. Chem. C*, v. 119, p. 6389–6397, 2015.

[2] PRIYA, S. M. et al. Structural, morphological and optical properties of tin oxide nanoparticles synthesized by sol-gel method adding hydrochloric acid. *J. Sol-Gel Sci. Technol.*, v. 78, p. 365–372, 2016.

[3] RECHBERGER, F. et al. Strategies to improve the electrical conductivity of nanoparticle-based antimony-doped tin oxide aerogels. *J. Sol-Gel Sci. Technol.*, v. 80, p. 660–666, 2016.

[4] BELTRÁN, J. J. et al. Crystallographic and magnetic properties of Fe-doped SnO_2 nanopowders obtained by a sol–gel method. *J. Mater. Sci.*, v. 45, p. 5002–5011, 2010.

[5] DIÉGUEZ, A. et al. The complete raman spectrum of nanometric SnO_2 particles. *J. Appl. Phys.*, v. 90, p. 1557, 2001.

[6] PEREIRA, M. S. et al. Application of Fe-doped SnO_2 nanoparticles in organic solar cells with enhanced stability. *Opt. Mater.*, v. 64, p. 548–556, 2017.

[7] TROST, S. et al. Avoiding photoinduced shunts in organic solar cells by the use of tin oxide (SnO_x) as electron extraction material instead of ZnO. *Adv. Energy Mater.*, v. 6, p. 1600347, 2016.

[8] BIRKEL, A. et al. Highly efficient and stable dye-sensitized solar cells based on SnO_2 nanocrystals prepared by microwave-assisted synthesis. *Energy Environ. Sci.*, v. 5, n. 5392, 2012.

[9] PAL, M. et al. Sol-gel based simonkolleite nanopetals with SnO_2 nanoparticles in graphite-like amorphous carbon as an efficient and reusable photocatalyst. *RSC Adv.*, v. 5, p. 75062, 2015.

[10] SUN, J. et al. Growth of SnO_2 nanowire arrays by ultrasonic spray pyrolysis and their gas sensing performance. *RSC Adv.*, v. 4, p. 43429, 2014.

[11] MEI, L. et al. Gas sensing of SnO_2 nanocrystals revisited: Developing ultra-sensitive sensors for detecting the H_2S leakage of biogas. *Scientific Reports*, v. 4, p. 6028, 2013.

[12] MUELLER, F. et al. Fe-doped SnO_2 nanoparticles as new high capacity anode material for secondary lithium-ion batteries. *J. Power Sources*, v. 299, p. 398–402, 2015.

[13] AHMED, S. Room-temperature ferromagnetism in pure and Mn doped SnO_2 powders. *Solid State Commun.*, v. 150, p. 2190–2193, 2010.

[14] FERRARI, S. et al. Magnetic properties and environment sites in Fe doped SnO_2 nanoparticles. *Mater. Chem. Phys.*, v. 177, p. 206–212, 2016.

[15] SHAYESTEH, S. F.; NOSRATI, R. The structural and magnetic properties of diluted magnetic semiconductor $Zn_{1-x}Ni_xO$ nanoparticles. *J. Supercond. Nov. Magn.*, v. 28, p. 1821–1826, 2015.

[16] MEHRAJ, S. et al. Structural, electrical and magnetic properties of (Fe, Co) co-doped SnO_2 diluted magnetic semiconductor nanostructures. *Physica E*, v. 65, p. 84–92, 2015.

[17] INPASALINI, M. S. et al. Evidence of bound magnetic polaron-mediated weak ferromagnetism in co-doped SnO_2 nanocrystals: Microstructural, optical, hyperfine, and magnetic investigations. *J. Electron. Mater.*, v. 45, p. 3562–3569, 2016.

[18] MENESES, C. T. et al. A simple route to the synthesis of high-quality NiO nanoparticles. *J. Nano. Res.*, v. 9, p. 501–505, 2007.

[19] NOGUEIRA, N. A. S. et al. X-ray diffraction and mossbauer studies on superparamagnetic nickel ferrite ($NiFe_2O_4$) obtained by the proteic sol-gel method. *Mater. Chem. Phys.*, v. 163, p. 402–406, 2015.

[20] BRAGA, T. P. et al. Synthesis of air stable FeCo alloy nanocrystallite by proteic sol-gel method using a rotary oven. *J. Alloys Compd.*, v. 622, p. 408–417, 2015.

[21] SANTOS, C. M. et al. Synthesis of FeNi alloy nanomaterials by proteic sol-gel method: Crystallographic, morphological, and magnetic properties. *J. Nanomater.*, v. 2016, p. 1–9, 2016.

[22] RIETVELD, M. H. Line profiles of neutron powder-diffraction peaks for structure refinement. *Acta Crystallogr.*, v. 22, p. 151, 1967.

[23] RIETVELD, H. M. A profile refinement method for nuclear and magnetic structures. *J. Appl. Crystallogr.*, v. 2, p. 65, 1969.

[24] TOBY, B. H. EXPGUI, a graphical user interface for GSAS. *J. Appl. Crystallogr.*, v. 34, p. 210, 2001.

[25] ZHAO, B. et al. Preparation of honeycomb SnO_2 foams and configuration-dependent microwave absorption features. *ACS Appl. Mater. Inter.*, v. 7, p. 26217–26225, 2015.

[26] LIU, J. et al. Synthesis of SnO_2/In_2O_3 hetero-nanotubes by coaxial-electrospinning method for enhanced formaldehyde response. *New J. Chem.*, v. 40, p. 1756, 2016.

[27] GHODSI, F. E. et al. Derivation of the optical constants of spin coated CeO_2–TiO_2–ZrO_2 thin films prepared by sol-gel route. *J. Phys. Chem. Solid*, v. 72, p. 761–767, 2011.

[28] WILLIAMSON, G. K.; HALL, W. H. X-ray line broadening from filed aluminium and wolfram. *Acta Metallurgica*, v. 1, p. 22, 1953.

[29] ARAGÓN, F. H. et al. Fe doping effect on the structural, magnetic and surface properties of SnO_2 nanoparticles prepared by a polymer precursor method. *J. Phys. D: Appl. Phys.*, v. 49, p. 155002, 2016.

[30] SMITH, B. C. The infrared spectroscopy of alkenes. *Spectroscopy*, v. 31, p. 28–34, 2016.

[31] LIM, A. H. et al. Biomineralized Sn-based multiphasic nanostructures for Li-ion battery electrodes. *Nanoscale*, v. 4, p. 4694, 2012.

[32] ZHU, H. et al. A simple hydrothermal route for synthesizing SnO_2 quantum dots. *Nanotechnology*, v. 17, p. 2386–2389, 2006.

[33] CHEN, H. et al. Synthesis and characterization of Ni doped SnO_2 microspheres with enhanced visible-light photocatalytic activity. *RSC Adv.*, v. 5, p. 56401, 2015.

[34] ZHANG, J.; GAO, L. Synthesis and characterization of nanocrystalline tin oxide by sol–gel method. *J. Solid State Chem.*, v. 177, p. 1425–1430, 2004.

[35] AZAM, A. et al. Effect of Mn doping on the structural and optical properties of SnO_2 nanoparticles. *J. Alloys Compd.*, v. 523, p. 83–87, 2012.

[36] SRINIVAS, K. et al. Structural, optical, and magnetic properties of nanocrystalline Co doped SnO_2 based diluted magnetic semiconductors. *J. Phys. Chem. C*, v. 113, p. 3543–3552, 2009.

[37] FANG, L. M. et al. Synthesis and characteristics of $Fe^{(}3+)$-doped SnO_2 nanoparticles via sol-gel-calcination or sol-gel-hydrothermal route. *J. Alloy. Compd.*, v. 454, p. 261–267, 2008.

[38] MANDAL, S. K. et al. Reduction of magnetization in $Zn_{0.9}Fe_{0.1}O$ diluted magnetic semiconducting nanoparticles by doping of Co or Mn ions. *J. Appl. Phys.*, v. 101, p. 123920, 2007.

[39] FUKAI, Y. et al. Highly efficient dye-sensitized SnO_2 solar cells having sufficient electron diffusion length. *Electrochem. Commun.*, v. 9, p. 1439–1443, 2007.

[40] KRISHNAMOORTHY, T. et al. A facile route to vertically aligned electrospun SnO_2 nanowires on a transparent conducting oxide substrate for dye-sensitized solar cells. *J. Mater. Chem.*, v. 22, p. 2166, 2012.

4. APPLICATION OF Fe-DOPED SnO_2 NANOPARTICLES IN ORGANIC SOLAR CELLS WITH ENHANCED STABILITY

Solution-processed P3HT:PCBM-based bulk heterojunction organic solar cells were constructed with Fe-doped tin oxide (Fe/SnO_2) magnetic nanoparticles (NP) incorporated to the active layer. Performance and stability of devices were evaluated. Devices reinforced with Fe/SnO_2 nanoparticles showed improvement in short-circuit current density J_{sc} up to 10 %, when compared with devices without the addition of NPs. Improved J_{sc} was attributed to the extension of photogenerated exciton lifetime as a result of the magnetic field provided by the NPs. Life time and stability tests revealed extended T_{80} for samples reinforced with NPs for both indoor and outdoor tests, which can be attributed to slightly improvements of fill factor during aging tests. Moreover, NP-reinforced devices have shown the tendency to overcome the burn-in regime faster. These results are indications that the addition of diluted magnetic semiconductor oxide nanoparticles in the active layer of organic solar cells has the potential to contributed to the extension of lifetime and improvement of stability of these devices.

4.1 Introduction

Organic solar cells (OSCs) are showing rapid advances in efficiency and potential for technological applications. In recent years, bulk heterojunction (BHJ) OSCs have attracted attention for both academic and industrial sectors due to their premium features of flexibility, fabrication simplicity, low manufacturing costs, short energy payback time, and low environmental impact [1–3]. In 2016, the companies Raynergy Tek and Heliatek reported power conversion efficiencies (η) over 11 % for single junction cells and as high as 13 % for tandem small molecule cells, respectively. This indicates that OSCs are strongly

competitive against their inorganic counterparts [4]. As the most reported architecture of OSCs, the BHJ structure comprises an interpenetrating network of a conjugated polymer donor such as poly(3-hexylthiophene-2,5-diyl) (P3HT) and a soluble fullerene acceptor which is typically [6,6]-phenyl-C_{60}-butyric acid methyl ester (PCBM) as the photoactive layer [5–9]. P3HT:PCBM BHJ OSCs was one of the first studied OSCs and still is the most widely studied structure, as both P3HT and PCBM materials are commercially available and more affordable.

Most recent studies on P3HT:PCBM BHJ-OSCs have been focused on optimizing microphase separation by choosing proper solvents for processing the photoactive layers [8, 10–12] or by post-thermal treatment of the photoactive layers [8, 10, 13]. Given the difficulty to tune the morphology between donor and acceptor materials at such small scales, another way around this issue that has gained attention consists of increasing the effective lifetime of the photogenerated excitons, and thereby their diffusion length [14–16].

It is known that in organic materials such as P3HT the primary photo-generated charge carriers are Coulomb-bound electron–hole pairs, so-called excitons, which lie in both singlet states and triplet states with different lifetimes. Only the dissociated excitons, i.e., Coulomb-bound electron–hole pairs dissociated into free charge carriers, could contribute to the photocurrent. One major bottleneck for the efficiency of this process is that in P3HT the singlet lifetime is approximately 300 ps and the resulting singlet exciton diffusion length is reported in the range of 3-6 nm [14, 17, 18]. In contrast, the P3HT triplet lifetime is in the order of 10 μs implying a triplet exciton diffusion length of the order of 100 nm [19], which aids their diffusion process toward donor-acceptor junctions and thus enhances the photovoltaic process in OSCs [14]. The migration of excitonic states from the excited singlet to the triplet can occur in the presence of strong spin–orbit coupling. This transition is known as intersystem crossing.

Magnetic nanoparticles, ferromagnetic domain boundaries, and surfaces exhibiting antiferromagnetism are amongst nanostructures that may bring about current enhancement [20]. Several recent observations suggest that magnetic nanostructures may induce

unusual spin dynamics of electrons in nearby organic molecules. These effects include enhanced quantum efficiency, magnetically modulated quantum efficiency [21] in organic LEDs doped with magnetic nanoparticles. Recently, several groups of researchers have reported improvements in efficiency and stability with insertion of NPs in BHJ CSOs [5–7, 22, 23].

Despite considerable improvement of OSCs η values, their poor stability and short carriers lifetime are still issues that need to be addressed before this technology becomes commercially viable. Organic solar cells degrade due to a number of factors, such as exposure to high temperatures and UV-light, water or oxygen intake, mechanical stress, among others [24]. One of the strategies that have been applied to improve OSCs lifetime and stability is the replacement of highly hygroscopic [25, 26] PEDOT:PSS as hole transport material (HTL). Over the last few years, transition metal oxides with large work function like NiO [27], MoO_3 [28, 29], WO_3 [30] and V_2O_5 [31, 32] among others, have been shown to be viable options as hole-transport layer in stable OSCs. In fact, water-based V_2O_5 was found be highly compatible with printing techniques [33] and was used as HTL for all OSCs used in this work.

In this chapter, we introduce Fe doped SnO_2 (Fe/SnO_2) magnetic nanoparticles (NPs) into P3HT:PCBM BHJ OSCs and find that the doping of NPs result in the enhancement of the J_{sc} and stability. In order to discuss in which way the performance of OSCs doped with NPs is mainly affected, we present a study based on the model system P3HT:PCBM solar cells blended with weight concentration of 10 % NPs.

4.2 Experimental procedure

4.2.1 Synthesis of Fe/SnO_2 nanoparticles

Fe/SnO_2 nanoparticle (Fe:Sn molar ratio of 1:10) samples were prepared by high-energy ball milling. Commercial SnO_2 and Fe_2O_3 (Sigma-Aldrich, 99.9 %) powders together with alumina vials and zirconia spheres (ball-to-powder mass ratio of 20:1) were used in a planetary mill (Fritsch Pulverissette 6) operating with an angular velocity of 500 rpm.

4.2.2 Solar cell fabrication

Two types of solar cell devices were prepared with inverted configuration and tested in air under ambient conditions: reference devices (ref-OSC) with configuration FTO/ZnO/ P3HT:PCBM/V_2O_5/Ag; and nanoparticle-bearing devices (NP-OSC) with configuration FTO/ZnO/P3HT:NP:PCBM/V_2O_5/Ag (see Fig. 4.1). The devices were built with an active area of 0.20 cm^2.

Figure 4.1: Schematic overview of the manufactured devices.

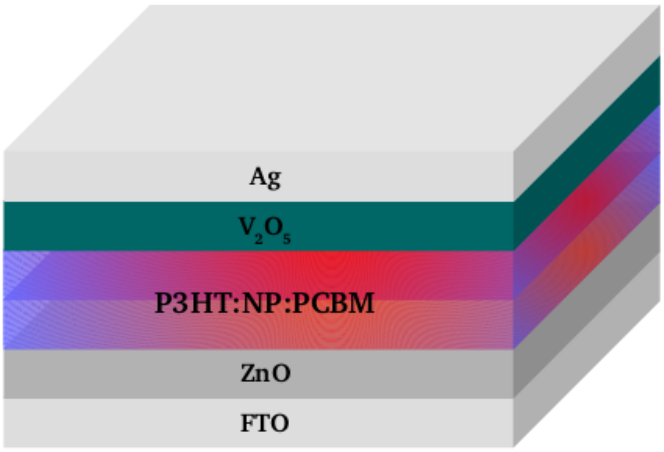

Source: Own author.

A 30 nm thick electron transport layer (ETL) was deposited from a solution of ZnO in chlorobenzene (40 mg/ml) that was spin-coated at 3000 rpm on the FTO surface (70 Ω/□) and dried at 140 °C for 30 min at air atmosphere conditions. This solution was produced by collaborators [8].

The bulk heterojunction blend of ref-OSCs comprised of a 1:1 molar mixture of P3HT:PCBM dissolved in 1,2-dichlorobenzene while that of NP-OSCs comprised of a molar 0.9:0.1:1 mixture of P3HT:NP:PCBM. The nanoparticles were suspended in 1,2-dichlorobenzene (30 mg/ml) and mixed added to the P3HT:PCBM blend to achieve the desired concentration. Blends were spin coated at 1000 rpm to deposit a 300 nm-thick

P3HT:PCBM and P3HT:NP:PCBM films.

A 120-nm thick hole transport layer (HTL) was deposited from a molar 1:1 solution of V_2O_5 sol-gel:isopropanol that was spin-coated at 3000 rpm and annealed at 120 °C for 1-2 min on a hot plate at atmosphere conditions. The V_2O_5 sol-gel was produced by collaborators [8].

Finally, a 100 nm-thick Ag back metal electrode was deposited by thermal evaporation in an evaporation system (Auto 306, BOC Edwards). The devices were subsequently annealed at 120 °C for 10 min in air. A set of six ref-OSC and NP-OSC devices were prepared for the tests of efficiency and stability.

4.2.3 Characterization

X-ray diffraction (XRD) patterns of powdered nanoparticles were collected at room temperature using a Rigaku DMAXB diffractometer operating with a Kα-Cu source (λ = 1.54 Å) at 40 kV and 30 mA. The data were collected in a range of 20 °-100 ° in 2θ and the pattens were Rietveld refined using the program GSAS [34].

Magnetization measurements of powdered nanoparticles were carried out at room temperature using a Lakeshore (model 7404) vibrating sample magnetometer (VSM) with maximum field of 27 kOe. Room temperature Mössbauer spectra were measured in transmission mode using a ^{57}Co(Rh) radioactive source mounted on a velocity driver operating in sinusoidal mode. The data were evaluated by least square fitting to series of discrete Lorentzian shaped subspectra by means of the software package Normos. Isomer shifts (δ) are quoted with respect to α-Fe.

Active layer film samples for atomic force microscopy (AFM), conductive atomic force microscopy (c-AFM) and scanning electron microscopy (SEM) were prepared via spin-coating of blends on a glass substrate covered with a 30 nm layer of ZnO. AFM and c-AFM measurements were done in air under ambient conditions using a Asylum Research scanning probe microscope. Images were collected in tapping mode using a Nanoworld (model Arrow CONTPt) Pt-coated Si probe with a spring constant of 0.2 N/m. SEM measurements were performed in air under ambient conditions using a Quanta FEG 450.

Solar simulations was performed on a KHS1200 (Steuernagel Solarkonstant) equipped with an AM1.5 filter (100 mW/cm^2, AM1.5G, 72 °C). J×V curves were measured using a Keithley 2601 multimeter with light intensity of 100 mW, calibrated with a Zipp & Konen CM-4 pyranometer, which was used constantly during measurements to set light intensity. A calibrated S1227-1010BQ photodiode from Hamamatsu was also applied for calibration before each measurement. Incident photon-to-electron conversion efficiency (IPCE) analyses were done with a QE/IPCE measurement System from Oriel (from 300 to 800 nm; at 10 nm intervals). The results were not corrected for any intensity losses due to light absorption or reflection by the glass support.

4.3 Results and discussion

4.3.1 Fe/SnO_2 nanoparticles

Figure 4.2 shows the XRD pattern of a Fe/SnO_2 nanoparticle sample.

Figure 4.2: X-ray diffraction pattern of a Fe/SnO_2 nanoparticle sample. Dots and solid lines are the experimental data and best fit respectively. Bars represent the ICSD-39173 standard pattern.

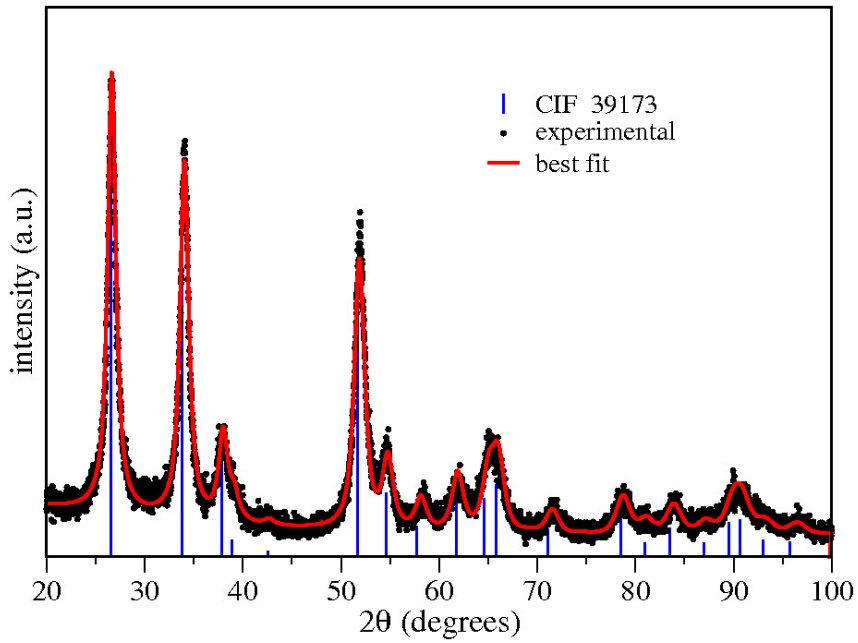

Source: Own author

The diffraction peaks correspond to the rutile-type tetragonal structure of SnO_2. No Fe-bearing phase was found indicating total incorporation of Fe_2O_3 by the SnO_2 matrix. The average particle size calculated using Scherrer's equation and corrected by the Williamson-Hall relation (which separates contributions of particle size and residual microstrain to the breadth of diffraction peaks) is about 10 nm.

Mössbauer spectra of Fe/SnO_2 nanoparticle sample and respective best fits (achieved using two paramagnetic doublets) are shown in Fig. 4.3. The absence of sextets confirms the successful incorporation of Fe^{3+} to the matrix. Isomer shift and quadrupole splitting values of both doublets are consistent with octahedral coordinated Fe^{+3} substituting for Sn^{4+} in the SnO_2 [35] matrix.

Figure 4.4 shows the magnetization *vs* applied field curve obtained at room temperature from a Fe/SnO_2 nanoparticle sample. The curve consists of a linear paramagnetic component and a magnetic hysteresis loop with coercivity of 145 Oe and remanent magnetization of 6.3×10^{-3} emu/g. These values indicate that the sample is ferromagnetic at room temperature.

Figure 4.3: Mössbauer spectrum of a Fe/SnO_2 nanoparticle sample.

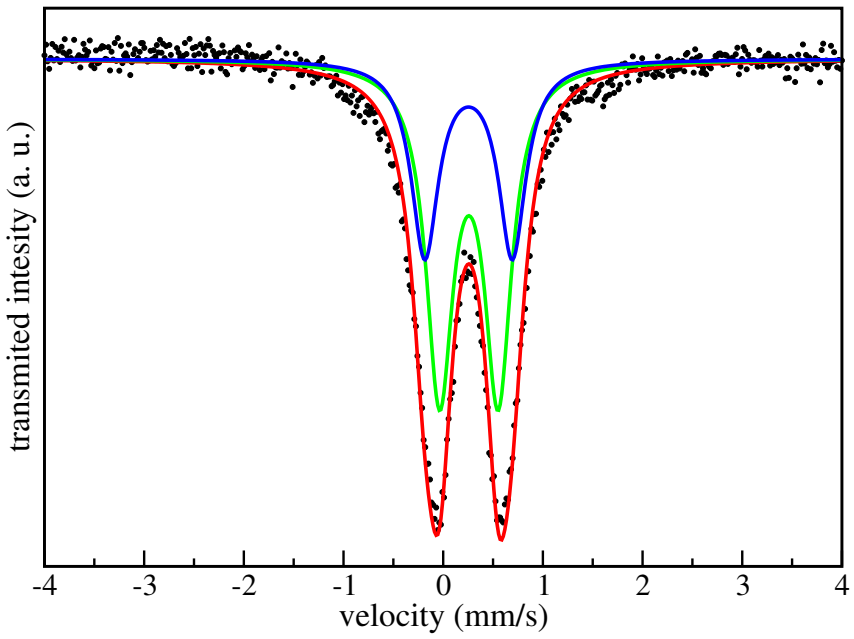

Source: Own author

Figure 4.4: Room temperature hysteresis loop of a Fe/SnO_2 nanoparticle sample.

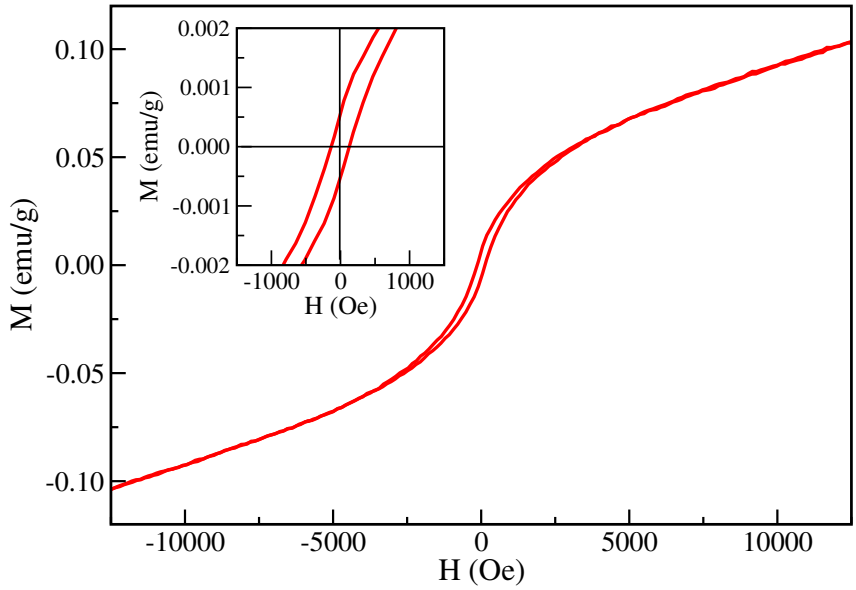

Source: Own author

4.3.2 Films morphology

Figure 4.5 shows SEM images of (a) ref-OSC and (b) NP-OSC active layer films. The images show PCBM domains (lighter regions) randomly distributed within the P3HT matrix (dark background) [5, 36]. The NP-OSC film also show bright spots attributed to clusters of NPs according to energy dispersive X-ray spectrometry results.

Figure 4.6 shows AFM and c-AFM images of the active layer of a ref-OSC and a NP-OSC film. It can be observed on the AFM surface topography images – parts (a) and (c) – that the addition of nanoparticles affects the morphology of the film, introducing aggregated domains (bright spots in Fig. 4.6c) reinforcing the SEM results. Doping induces the formation of NPs clusters that yield uneven film morphology which can lead to decrease of the shunt resistance R_{sh} and consequent increased leakage current [22].

Current AFM images – parts (b) and (d) – was used to examine conductivity variations in the P3HT:NP:PCBM blends. A high work function Pt-coated Si probe was used in all measurements. The high electron injection barrier between the Pt-coated Si tip and the P3HT:NP:PCBM blend blocks electron injection which allows hole transport only

within P3HT [13]. Therefore, bright and dark regions are attributed to P3HT-rich and PCBM-rich domains, respectively. Images of NP-bearing samples show non-conductive dark spots associated to clusters of NPs in the active layer, as was pointed out above.

Figure 4.5: SEM images of (a) ref-OSC and (b) NP-OSC films.

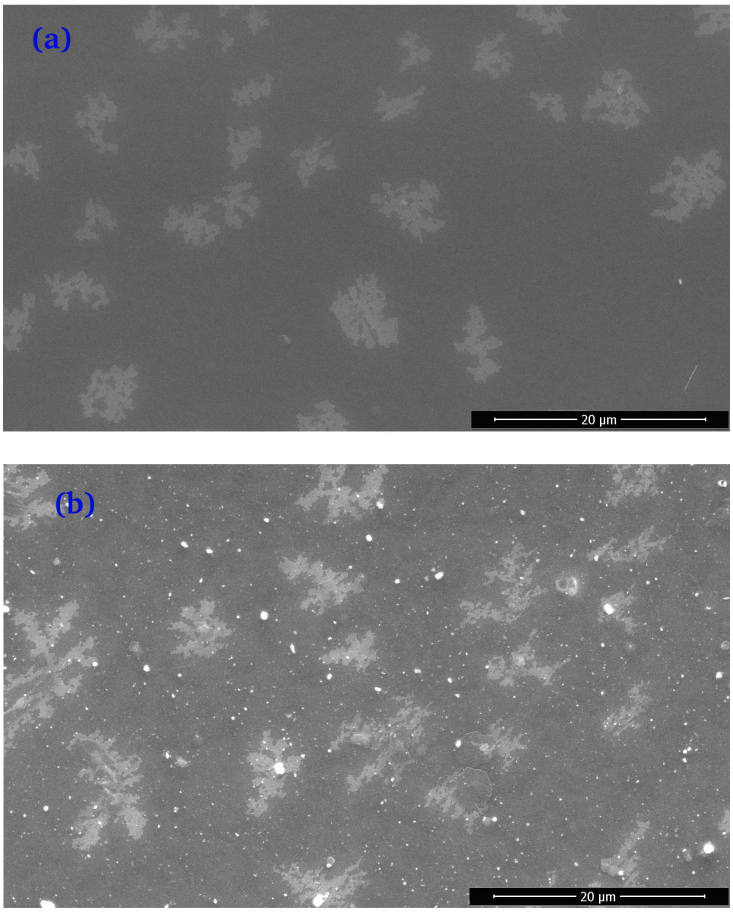

Source: Own author

Figure 4.6: (a) AFM and (b) c-AFM images of a ref-OSC film; (c) AFM and (d) c-AFM images of a NP-OSC film.

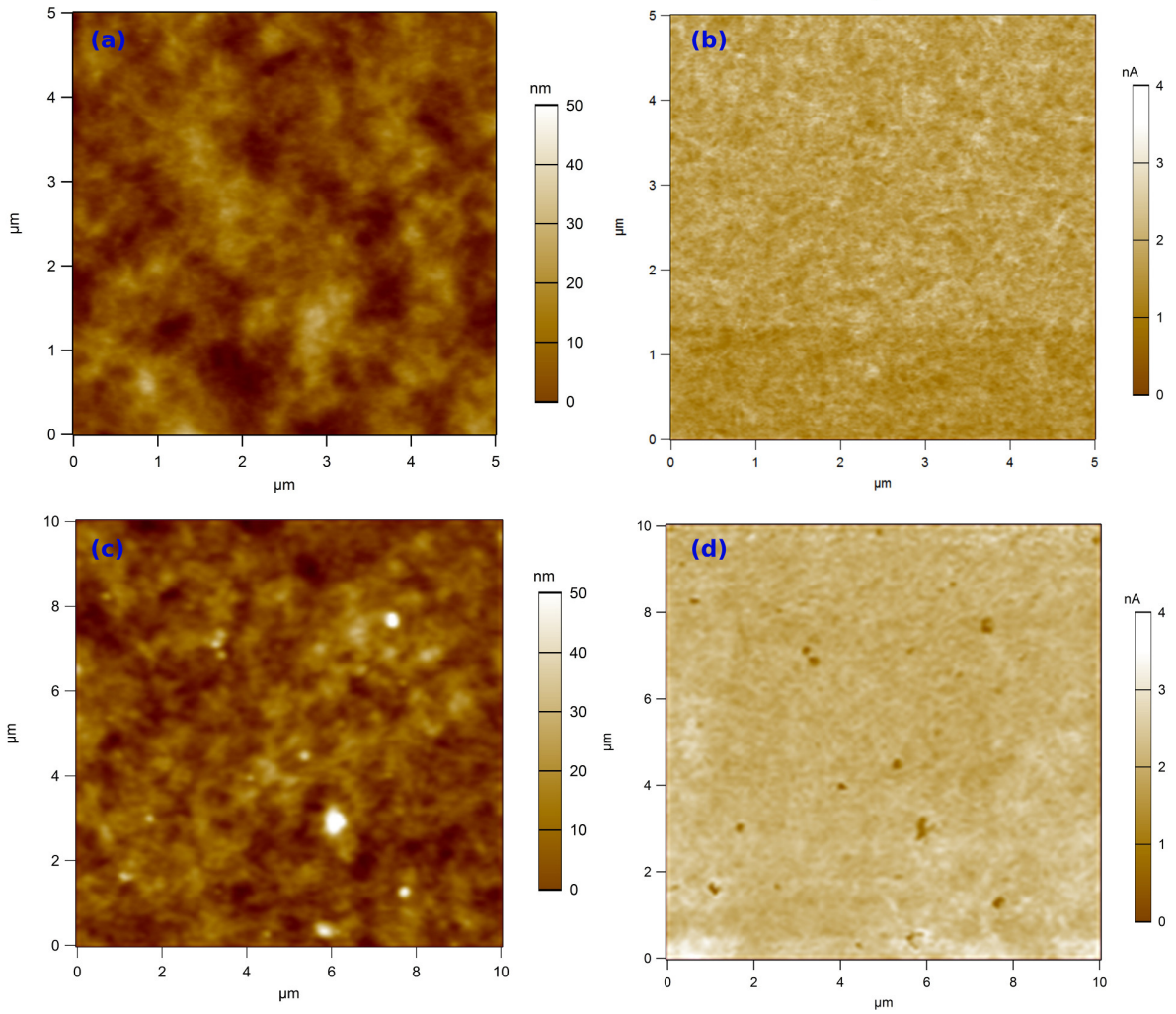

Source: Own author

4.3.3 Solar cells performance

Figure 4.7 shows (a) characteristic J×V curves (under AM1.5G illumination with light intensity of 100 mW/cm^2) and (b) normalized IPCE spectra of the ref-OSC and NP-OSC cells with the best performance. Photovoltaic parameters for a hero device and the average of the set of six samples of either ref-OSC or NP-OSC type are summarized in Table 4.1. It can be seen that the photovoltaic parameters of the best cells were very close to the average values of each set of six devices, ensuring good reproducibility of the results.

The devices reinforced with nanoparticles showed a slightly improved J_{sc} with average value increasing from 11.25 to 12.09 mA/cm^2. This suggests that the addition of NPs contributes to the dissociation of photogenerated excitons into free charge carriers result-

ing in an enlarged short-circuit current density. The broader IPCE spectrum found for NP-OSCs seen in Fig. 4.7b reinforces this suggestion.

Figure 4.7: (a) J×V curves and (b) normalized IPCE spectra of the best ref-OSC and NP-OSC cells.

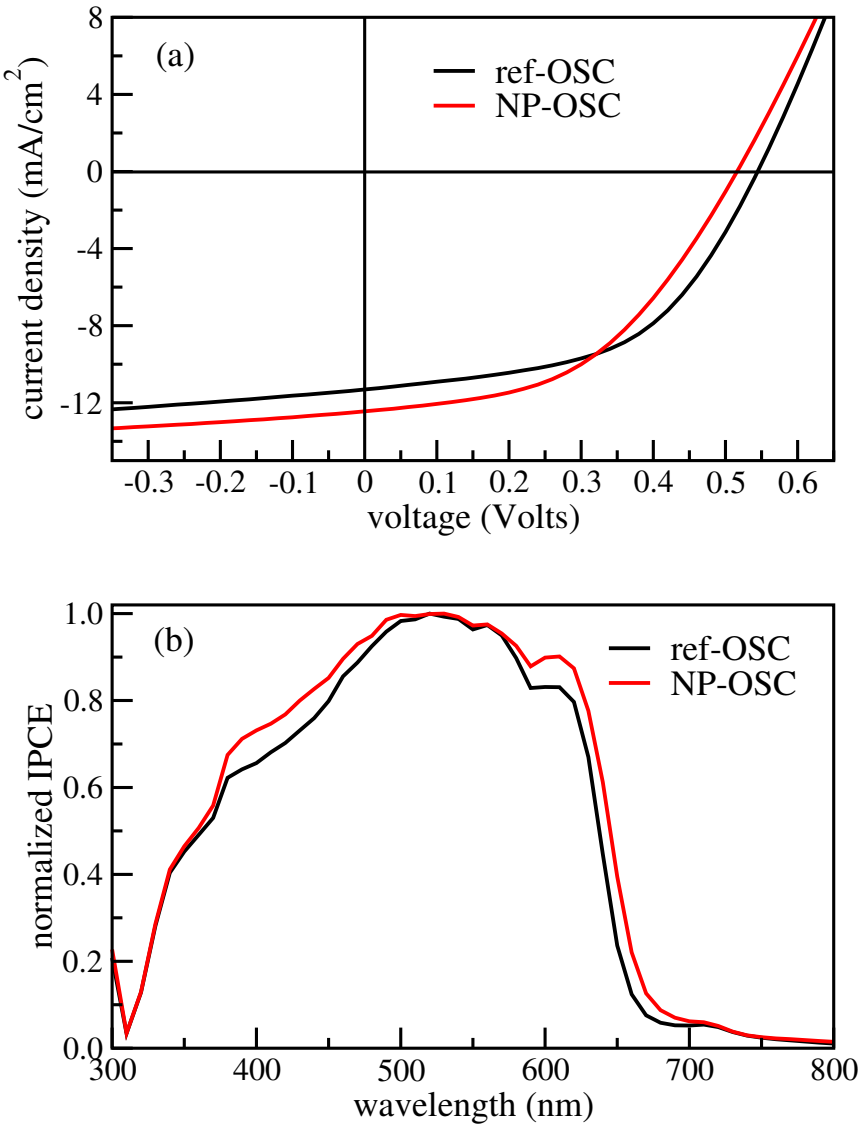

Source: Own author

Average V_{oc} was slightly lower for NP-OSCs, which can be attributed to added disorder to the system due to the presence of magnetic nanoparticles [37, 38]. Average FF was also lower for NP-OSC. This effect is very often observed in devices with enhanced J_{sc} [39].

The increase in the density of free photogenerated carriers improves both J_{sc} values and recombination rates due to a competition between recombination and extraction of free charges [39]. The combination of these effects tends to lower FF values

Series resistance (R_s) and shunt resistance (R_{sh}) were calculated from the slope of J×V curves and are also shown in Table 4.1. The increasing on average R_s values for NP-OSC devices is remarkable and most likely due to the presence of NP aggregates as seen on microscopy images.

As mentioned previously, addition of NPs to the active layer of OSCs produced a broader IPCE spectrum (see Fig. 4.7b). This improvement is observed in the region of longer wavelengths, suggesting that doping has caused a reduction in energy levels HOMO and LUMO of the donor.

Table 4.1: Photovoltaic parameters and resistance values of ref-OSC and NP-OSC devices.

Device	J_{sc} (mA/cm^2)	V_{oc} (V)	FF (%)	η (%)	R_s (Ω cm^2)	R_{sh} (Ω cm^2)
ref-OSC						
hero	11.30	0.54	52.0	3.20	425	275
avg	11.25 ± 0.04	0.54 ± 0.0	50.4 ± 1.0	3.06 ± 0.09	553 ± 100	298 ± 17
NP-OSC						
hero	12.44	0.52	47.34	3.04	1200	411
avg	12.09 ± 0.24	0.52 ± 0.0	47.24 ± 0.6	2.96 ± 0.06	831 ± 273	321 ± 69

Source: Own author

4.3.4 The role of magnetic NPs

Figure 4.8 shows measurements of photocurrent density J_{ph} as a function of effective bias voltage ($V_0 - V$). In both cells, photocurrent values increase sharply from zero to about 0.6 V when they slow down gradually as saturation is approached. The slope of the rise is steeper (see inset) and saturation is reached earlier for the reference device. The slightly larger saturation current in NP-OSC devices is attributed to a higher dissociation

of photogenerated excitons into free charge carriers. Therefore, the presence of magnetic NPs does not contribute to exciton generation but with the enhancement of excitons dissociation rate.

Figure 4.8: Plots of photocurrent density with respect to effective bias.

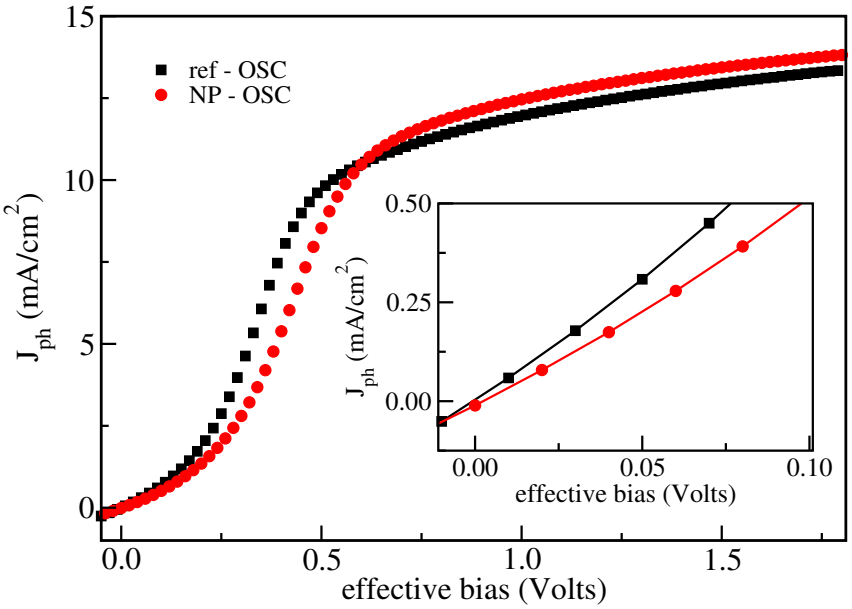

Source: Own author

Due to their ferromagnetism at room temperature, Fe/SnO_2 NPs generate a weak effective magnetic field within the OSC photoactive layer. The effect of magnetic fields on organic solar cells has been studied for different OSCs [6, 7, 22]. It has been observed that a low magnetic field can increase the rate of intersystem crossing thus increasing the concentration of triplet excitons. The increase of triplet excitons can lead to an increase of dissociated charge carriers due to triplets' longer lifetime in bulk materials as compared to that of singlet excitons, yielding larger currents through the devices [14, 22].

In order to clarify the effect of NPs on the enhancement of J_{sc} values, cells with P3HT:NP:PCBM molar ratios of 0:1:1 and 0.95:0.05:1 were fabricated and tested. The 0:1:1 cell exhibited very low J_{sc} ($\sim$0.14 mA/cm^2) and η ($\sim$0.006 %) values indicating that these NPs are not an efficient light absorbing material and electron donor.

Devices with 0.95:0.05:1 ratios exhibited smaller J_{sc} values ($\sim$9.47 mA/cm^2) than those of the reference devices. This decrease may be associated to the weak magnetism of these NPs. In low concentrations, the magnetic field generated within the active layer is not strong enough to yield a considerable rate of intersystem crossing. On the other hand, the clustering of NPs enables alternative conducting paths for charge carriers inducing leakage currents. Increasing doping to 0.9:0.1:1 yields a larger magnetic field within the active larger leading to a larger rate of intersystem crossing that overcomes the effect of leakage currents. This suggests that the improvement in J_{sc} values is likely associated with an effective magnetic field generated by the presence of magnetic NPs.

Progress in organic solar cells relies strongly on two features: dissociation of photogenerated excitons into free carriers, and ultrafast electron-hole (e-h) charge separation [40, 41]. Evidently understanding the underlying mechanism is useful for the future rational design of new OSCs with improved efficiency and stability, but unfortunately these phenomena cannot be explained completely by the traditional theories. Classical approaches consider the dependence of exciton dissociation on an increasing electric field in the device, as a coulombically bound e-h pair requires a certain electric field for complete separation [42, 43]. More sophisticated models incorporate explicitly the delocalization of the photogenerated charges by considering their effective masses [40]. Similarly, electron-phonon coupling [41] can strongly influence the process of exciton diffusion and dissociation dynamics in OSCs.

The exciton binding energy in a typical organic semiconductor has two components: the Coulomb energy of the e-h pair and the additional binding energy of the electron-phonon interaction. For the case that the exciton has negligible electron-phonon coupling, the optical absorption edge is coincident with the exciton energy (assuming a direct gap semiconductor), irrespective of the magnitude of the exciton binding energy. However, when the exciton has strong electron-phonon coupling, the optical absorption is no longer coincident with the exciton energy [41, 44]. The AFM and SEM images show a large degree of local disorder introduced by the incorporation of NPs. This disorder causes significant variations in the donor-acceptor interface and, consequently, can influence the

dissociation and collection of photogenerated excitons. Due to the disorder caused by the incorporation of NPs, it is possible that the NP-OSC devices have a strong electron-phonon coupling. Therefore, a more complete interpretation requires that the electron-phonon coupling energy must be taken into account.

Arkhipov *et al.* [45, 46] proposes that heavier carriers have smaller energy of zero-point oscillations and such carriers are localized within on-chain potential wells. Therefore, the field-controlled height of on-chain barriers essentially determines the probability of full dissociation and the field dependence of the free carrier yield becomes stronger with increasing effective mass m_{eff}. The effective mass of holes in P3HT is about $1.8m_e$ and is similar to many inorganic semiconductors [47] such as SnO_2 with $m_{\text{eff}} \approx 1.6m_e$ [48, 49]. Thus, no significant contributions are expected related to the hole effective mass in the NPs.

4.3.5 Lifetime and stability studies

Organic solar cells degrade due to a number of factors such as light exposure [50, 51], high temperatures [52, 53], low resistance to water and oxygen [54], as well as combinations of these factors and others [55]. In this work, lifetime and stability of OSCs with and without the addition of Fe/SnO_2 nanoparticles were measured according to ISOS standards [56] ISOS-L-1 and ISOS-O-2, outlined in Table 4.2.

Table 4.2: ISOS protocols used in this study for lifetime testing of OSCs.

Testing ID	Testing conditions			
	Light source	Temperature	Humidity	Environment
ISOS-L-1	Simulated (1 Sun)	Ambient	Ambient	Light only
ISOS-O-2	Sun light	Ambient	Ambient	Ambient

Source: Own author

4.3.5.1 ISOS-L-1 Test

ISOS-L-1 tests were performed for 70 h on encapsulated ref-OSC and NP-OSC samples according to the conditions described on Table 4.2. The time evolution of photovoltaic parameters normalized to their pre-test values is shown in Fig. 4.9. Relative conversion efficiency η for both devices is shown in part (a). It can observed that the NP-bearing device presented a slightly better stability, reaching T_{80} after 40 h while the sample without NPs reached T_{80} after about 15 h.

Figures 4.9b and 4.9c show the time evolution of relative photovoltaic parameters of ref-OSC and NP-OSC devices, respectively. V_{oc} of both devices remains relatively unchanged during the test, suggesting that the chemical potential and charge transfer energy across the devices did not change significantly.

Values of J_{sc} for both devices follow the time evolution recorded for conversion efficiency, with a steeper drop during the first few hours before reaching a plateau. The time consumed during this initial strong drop is referred to as burn-in time [57], which is a signature of light induced degradation [58–61]. Many factors can be responsible to this burn-in process. Polymer conjugation losses (e. g. chemical degradation of the electron donor in the active layer), decrease of donor/acceptor interface area due to increase of blend domains above the diffusion length of the exciton, and ordering of the polymer chains (e.g. due to chain scission) all contribute to cell degradation as they affect charge transport [62].

As J_{sc} tends to stabilize after some hours, the dominant degradation mechanism is expected to saturate. Street *et al.* [63] and Bhattacharva *et al.* [64] have described analogous drops on J_{sc} due to the creation of mid-gap defect states at the donor/acceptor interface due to prolonged light exposure. Several groups [65–68] described the same behavior attributing this lowering on J_{sc} to fullerene dimerization.

Fill factor values remain almost constant during the test with a slight increase recorded for the NP-OSC device. This improvement in FF for NP-OSC can be an indication that the addition of Fe/SnO_2 nanoparticles turned the device less sensitive to light soaking [69, 70]. The slight increase in FF with time together with the higher initial J_{sc} for the NP-OSC

makes the addition of Fe/SnO_2 nanoparticles on the active layer a promising approach to improve the lifetime of OSCs.

Figure 4.9: ISOS-L-1 test: (a) time evolution of conversion efficiency η of ref-OSC and NP-OSC; (b) time evolution of ref-OSC photovoltaic parameters; and (c) time evolution of NP-OSC photovoltaic parameters. All quantities normalized to their pre-test values.

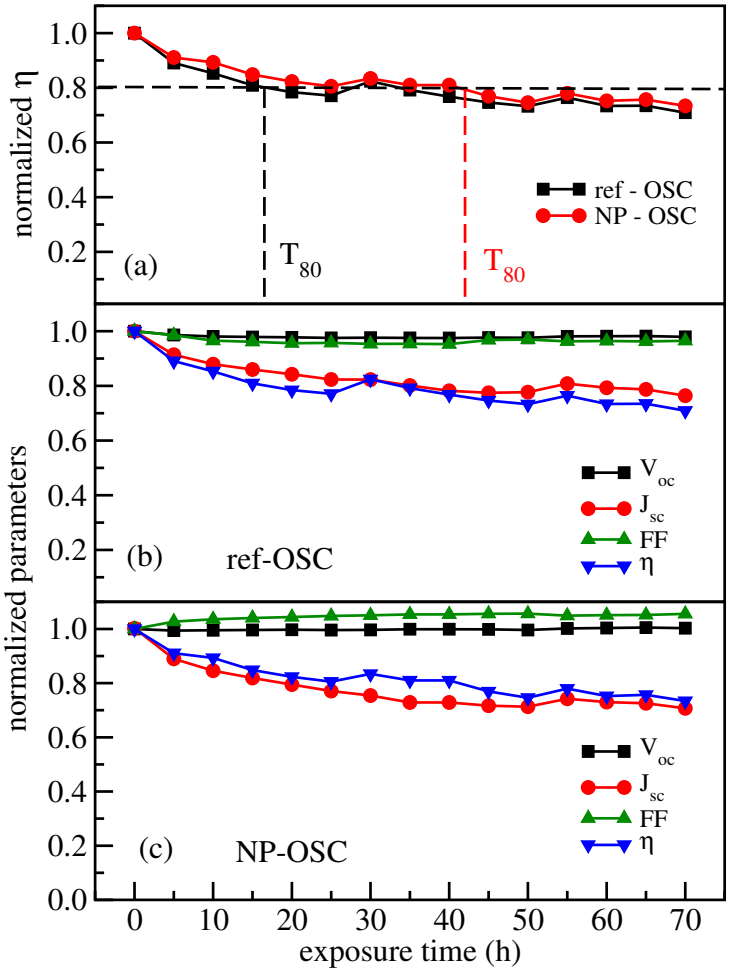

Source: Own author

Figure 4.10 shows a comparison of ref-OSC and NP-OSC normalized IPCE spectra before and after the ISOS-L-1 test. IPCE losses are clear in the 350-450 nm and 550-650 mn ranges and more pronounced for the NP-OSC device. Absorption in the range of 350-450 nm is mostly due to fullerene domains, which is an indication that the fullerene dimerization process was more intense in the NP-bearing OSC. As fullerene does not

absorb light in the 550-650 mn range, these losses must be related with P3HT degradation or oxide opacity in this range.

Figure 4.10: ISOS-L-1 test: normalized IPCE measurements before and after the test for (a) ref-OSC and (b) NP-OSC devices.

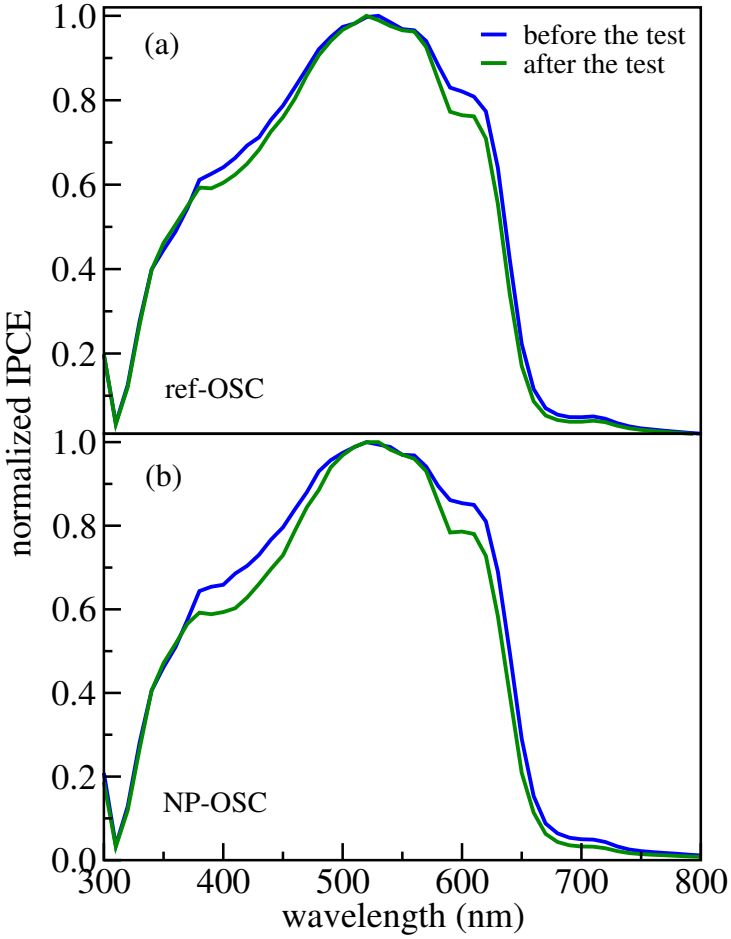

Source: Own author

4.3.5.2 ISOS-O-2 Test

To further evaluate the stability of NP-bearing solar cells, ISOS-O-2 standard tests under realistic conditions described on Table 4.2 were performed. Encapsulated ref-OSC and NP-OSC samples were attached to a solar tracker system and placed on the roof of the Catalan Institute of Nanoscience and Nanotechnology in Barcelona, Spain (41° 30' 8"

latitude and 2° 6' 42" longitude) for 21 days. The cells were characterized periodically by means of J×V measurements under real solar illumination.

Time evolution of conversion efficiency η for both samples is singled out in Fig. 4.11a while time evolution of V_{oc}, J_{sc}, η and FF is shown in Fig. 4.11b (ref-OSC) and Fig. 4.11c (NP-OSC). All parameters were normalized to their pre-test values. The data showed that samples in outdoor conditions degraded similarly to samples submitted to controlled indoor tests, which suggest that the degradation mechanisms were similar, albeit on a different time scale.

Figure 4.11: ISOS-O-2 test: (a) time evolution of conversion efficiency η of ref-OSC and NP-OSC; (b) time evolution of ref-OSC photovoltaic parameters; and (c) time evolution of NP-OSC photovoltaic parameters. All quantities normalized to their pre-test values.

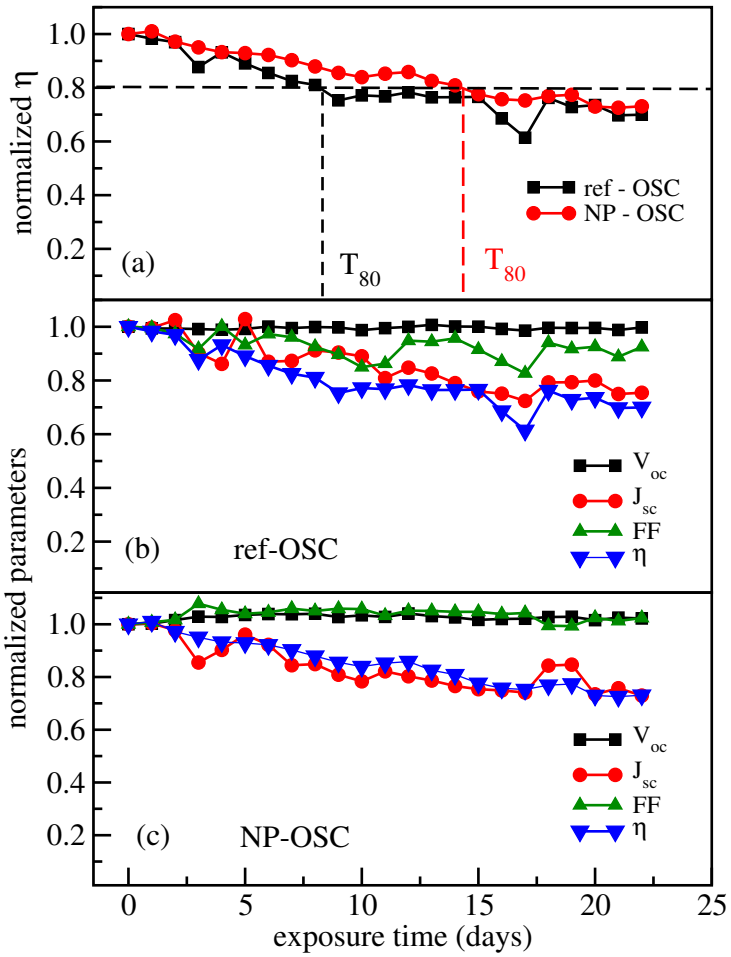

Source: Own author

As observed from the ISOS-L-1 standard indoor test, the NP-OSC device presented a longer T_{80} time than the ref-OSC device (14 days against 8 days). V_{oc} of both devices also remains relatively unchanged during the test. The drop of ref-OSC conversion efficiency follows the decrease in J_{sc} but is also influenced by FF instability. The fill factor of the NP-OSC device, on the other hand, remains unchanged during of the test and η tracks closely the behavior of J_{sc}. A possible explanation for the ref-OSC FF instability is the increase of exciton recombination rate associated by fullerene dimerization. This effect is not observed for the NP-OSC likely due to longer exciton lifetimes.

The NP-OSC device experienced a greater amount of IPCE losses due to outdoor exposure than the reference device, as can be verified in Fig. 4.12. Losses were concentrated on the 350-450 nm range (absorption by fullerene) which is a strong indication of the occurrence of dimerization. Losses also occurred on the 550-650 mn range most likely due to P3HT photodegradation. Despite the more severe relative losses, the NP-OSC device maintained a higher external quantum efficiency throughout the test as can bee seen in Fig. 4.13.

It is important to point out that the IPCE reduction of the NP-bearing device observed in Fig. 4.12 was more severe during the first 10 days as compared to the last 11 days of test. The reference device, on the other hand, experienced an almost linear decrease of IPCE. This result indicates that the presence of NP in the active layer led to faster degradation of the solar cell in the beginning of its lifetime, achieving stabilization before the reference device and maintaining a stronger IPCE after stabilization, which is desired in the long term.

4.4 Conclusion

Bulk heterojunction organic solar cells were built doping the P3HT:PCBM active layer with 10 at.% of Fe/SnO2 magnetic nanoparticles. Devices without NPs in the active layer were also produced to serve as reference. Slightly improved J_{sc}, together with a broader IPCE spectrum, suggests that addition of NPs to the devices contributed to the dissociation of photogenerated excitons into free charge carriers. Measurements of

Figure 4.12: ISOS-O-2 test: normalized IPCE measurements before the test, after 10 days of exposure and after 21 days of exposure (end of test) for (a) ref-OSC and (b) NP-OSC devices.

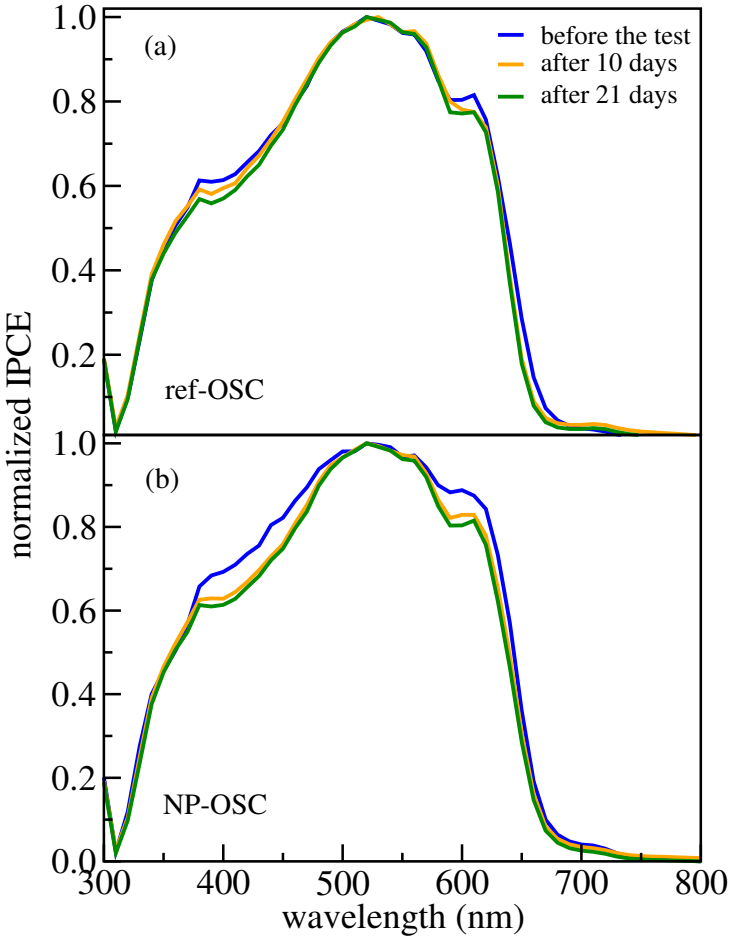

Source: Own author

photocurrent density *vs*. effective bias voltage reinforces this suggestion. The increase of dissociated charge carriers is attributed to the presence of a week effective magnetic field in the active layer. This field increases the rate of intersystem crossing thus increasing the concentration of longer lived triplet excitons [6, 7, 14].

Stability studies following the ISOS-L-1 (indoors) and ISOS-O-2 (outdoors) protocols revealed an improved T_{80} for the NP-bearing devices. Degradation mechanisms were found to be likely the same for both reference and NP-doped cells, being mainly due to J_{sc} losses, which are closely related to PCBM dimerization. NP-OSCs experienced a strong initial drop in J_{sc} which was compensated by small improvements in V_{oc} and FF. It was shown that the presence of NPs in the active layer led to faster degradation of the solar cell in the beginning of its lifetime, nevertheless achieving stabilization before the

Figure 4.13: ISOS-O-2 test: normalized IPCE normalized measurements for ref-OSC and NP-OSC devices (a) before the test, (b) after 10 days of exposure and (c) after 21 days of exposure (end of test).

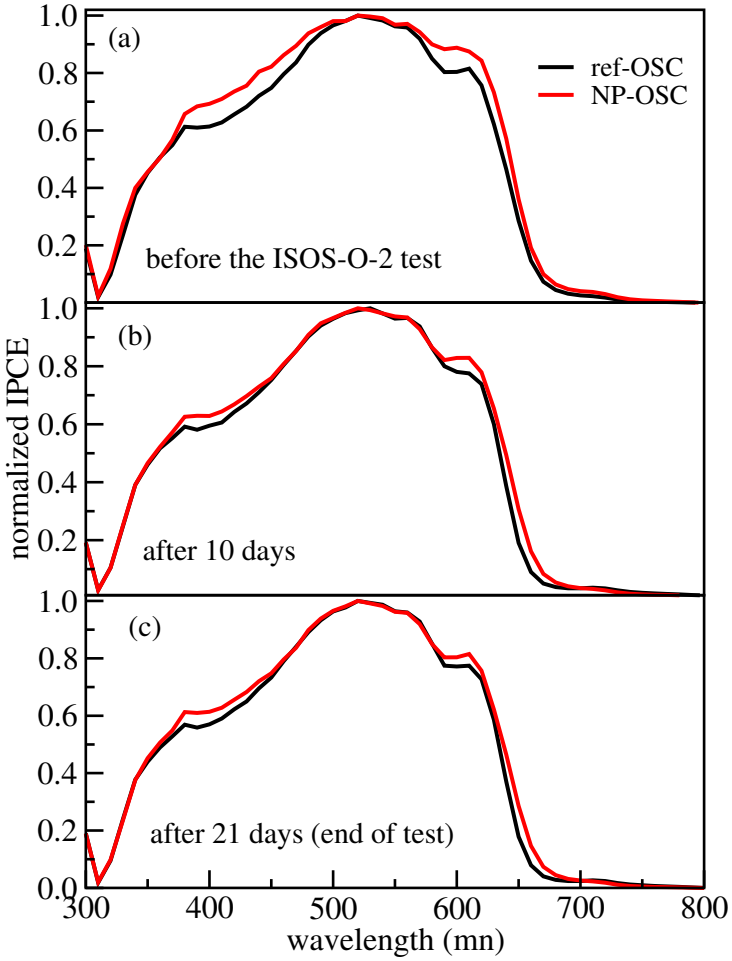

Source: Own author

reference device and maintaining a stronger IPCE after stabilization.

Doping of the active layer of OSCs with magnetic nanoparticles has been successfully used to modify the cells' electrical and optical properties. Improvements have been observed in aspects such as exciton dissociation and stability. The results obtained in this research work provide subsidies that propitiate an understanding of the effective action caused by the doping of the active layer of OSCs with magnetic NPs, thus opening new improvement opportunities by means of the addition of a degree of freedom for spin within the active layer. Using diluted magnetic semiconductor nanoparticles instead of ferromagnetic nanoparticles offers a new path of development for the field. The features shown by the NP-doped devices offer advantages in the long term and, therefore, the present work

represents an evolution as it showed further evidence that addition of magnetic nanoparticles to bulk heterojunction organic solar cells is a promising path to enhanced power conversion efficiency and stability.

4.5 References

[1] ANDERSEN, T. R. et al. Fully roll-to-roll prepared organic solar cells in normal geometry with a sputter-coated aluminium top-electrode. *Sol. Energy Mater. Sol. Cells*, v. 149, p. 103–109, 2016.

[2] KADUWAL, D. et al. Layout flexibility for sheet-to-sheet produced flexible ITO-free organic solar modules with organic functional layers slot die coated under ambient atmospheric conditions. *Sol. Energy Mater. Sol. Cells*, v. 136, p. 200–205, 2015.

[3] KREBS, F. C. et al. Freely available OPV–the fast way to progress. *Energy Technology*, v. 1, p. 378–381, 2013.

[4] HUANG, J. et al. Highly efficient organic solar cells with improved vertical donor–acceptor compositional gradient via an inverted off-center spinning method. *Adv. Mater.*, v. 28, p. 967, 2016.

[5] GONG, X. et al. Investigation of the magnetic nickel nanoparticle on performance improvement of P3HT:PCBM solar cell. *Appl. Phys. A*, v. 122, p. 287, 2016.

[6] WANG, K. et al. Effects of magnetic nanoparticles and external magnetostatic field on the bulk heterojunction polymer solar cells. *Scientific Reports*, v. 5, p. 9265, 2015.

[7] WANG, K. et al. Solution-processed Fe_3O_4 magnetic nanoparticle thin film aligned by an external magnetostatic field as a hole extraction layer for polymer solar cells. *ACS Appl. Mater. Interfaces*, v. 5, p. 10325–10330, 2013.

[8] TÉRAN-ESCOBAR, G. et al. Low-temperature, solution-processed, layered V_2O_5 hydrate as the hole-transport layer for stable organic solar cells. *Energy Environ. Sci.*, v. 6, p. 3088, 2013.

[9] IRWIN, M. D. et al. p-type semiconducting nickel oxide as an efficiency enhancing anode interfacial layer in polymer bulk-heterojunction solar cells. *PNAS*, v. 105, p. 2783–2787, 2008.

[10] HAMMED, W. A. et al. Recent approaches to controlling the nanoscale morphology of polymer-based bulk-heterojunction solar cells. *Energies*, v. 6, p. 5847–5868., 2013.

[11] KIM, Y. S. et al. Effect of solvents on the performance and morphology of polymer photovoltaic devices. *Curr. Appl. Phys.*, v. 10, p. 985–989., 2010.

[12] DANTE, M. et al. Nanoscale charge transport and internal structure of bulk heterojunction conjugated polymer/fullerene solar cells by scanning probe microscopy. *J. Phys. Chem. C*, v. 112, p. 7241 – 7249, 2008.

[13] CHEN, F. C. et al. Morphological study of P3HT:PCBM blend films prepared through solvent annealing for solar cell applications. *Solar Energy Materials & Solar Cells*, v. 94, p. 2426–2430, 2010.

[14] YAO, E.-P. et al. An investigation of organic photovoltaics improvement via extension of the exciton lifetime,. *Phys. Chem. Chem. Phys.*, v. 17, p. 5826, 2015.

[15] MIKHNENKO, O. V. et al. Direct measurement of the triplet exciton diffusion length in organic semiconductors. *Phys. Rev. Lett.*, v. 108, p. 137401, 2012.

[16] SAMIULLAH, M. et al. Diffusion length of triplet excitons in organic semiconductors. *Phys. Rev. B*, v. 82, p. 205211, 2010.

[17] SCULLY, S. R.; MCGEHEE, M. D. Effects of optical interference and energy transfer on exciton diffusion length measurements in organic semiconductors. *J. Appl. Phys.*, v. 100, p. 034907–1, 2006.

[18] KIM, Y.; BRADLEY, D. Bright red emission from single layer polymer light-emitting devices based on blends of regioregular P3HT and F8BT. *Curr. Appl. Phys.*, v. 5, p. 222–226, 2005.

[19] XU, B.; HOLDCROFL, S. Phosphorescence and delayed fluorescence of poly(3-hexylthiophene) films. *Thin Solid Films*, v. 242, p. 174, 1994.

[20] COHEN, A. E. Nanomagnetic control of intersystem crossing. *J. Phys. Chem. A*, v. 113, n. 41, p. 11084–11092, 2009.

[21] SUN, C. J. et al. Enhancement of quantum efficiency of organic light emitting devices by doping magnetic nanoparticles,. *Appl. Phys. Lett.*, v. 90, p. 232110, 2007.

[22] GONZÁLEZ, D. M. et al. Improved power conversion efficiency of P3HT:PCBM organic solar cells by strong spin-orbit coupling-induced delayed fluorescence. *Adv. Energy Mater.*, v. 5, p. 1401770, 2015.

[23] ZHANG, W. et al. Fe_3O_4 nanoparticles induced magnetic field effect on efficiency enhancement P3HT:PCBM bulk heterojunction polymer solar cells. *Sol. Energ. Mat. Sol. C.*, v. 95, p. 2880, 2011.

[24] CHENG, P.; ZHAN, X. Stability of organic solar cells: challenges and strategies. *Chem. Soc. Rev.*, v. 9, p. 2544–2582, 2016.

[25] NARDES, A. M. et al. Conductivity, work function, and environmental stability of PEDOT:PSS thin films treated with sorbitol. *Org. Electron.*, v. 9, p. 727, 2008.

[26] GLEN, T. S. et al. Grain size dependence of degradation of aluminium/calcium cathodes in organic solar cells following exposure to humid air. *Sol. Energy Mater. Sol. Cells*, v. 140, p. 25, 2015.

[27] YU, W. J. et al. Performance improvement of inverted polymer solar cells thermally evaporating nickel oxide as an anode buffer layer. *Sol. Energy Mater. Sol. Cells*, v. 98, p. 212, 2012.

[28] JUNG, J. et al. Highly efficient organic photovoltaic cells with molybdenum oxide buffer layer. *Jpn. J. Appl. Phys.*, v. 49, p. 05EB05, 2010.

[29] KYAW, A. K. K. et al. An inverted organic solar cell employing a sol-gel derived ZnO electron selective layer and thermal evaporated MoO_3 hole selective layer. *Appl. Phys. Lett.*, v. 93, p. 221107, 2008.

[30] HAN, S. et al. Improving performance of organic solar cells using amorphous tungsten oxides as an interfacial buffer layer on transparent anodes. *Org. Electron.*, v. 10, p. 791, 2009.

[31] MORAIS, A. et al. Enhanced photovoltaic performance of inverted hybrid bulk heterojunction solar cells using TiO_2/reduced graphene oxide films as electron transport layers. *J. Photonics Energy*, v. 5, p. 057408, 2015.

[32] LIMA, F. A. S. et al. Flexible ITO-free organic solar cells applying aqueous solution-processed V_2O_5 hole transport layer: An outdoor stability study. *APL Mater.*, v. 4, p. 026104, 2016.

[33] ZILBERBERG, K. et al. Inverted organic solar cells with sol–gel processed high work-function vanadium oxide hole-extraction layers. *Adv. Func. Mater.*, v. 21, p. 4776, 2011.

[34] TOBY, B. H. EXPGUI, a graphical user interface for GSAS. *J. Appl. Crystallogr.*, v. 34, p. 210, 2001.

[35] TORRES, C. E. R. et al. Magnetic behavior of nanoclusters of Fe-doped SnO_2. *Physica B*, v. 389, p. 176, 2007.

[36] WANG, D. H. et al. Solution-processable polymer based photovoltaic devices with concentration graded bilayers made via composition control of a poly(3-hexylthiophene)/[6,6]-phenyl C_{61}-butyric acid methyl ester. *J. Mater. Chem.*, v. 20, p. 4910–4915, 2010.

[37] BLAKESLEY, J. C.; NEHER, D. Relationship between energetic disorder and open-circuit voltage in bulk heterojunction organic solar cells. *Phys. Rev. B*, v. 84, p. 075210, 2011.

[38] ELUMALAI, N. K.; UDDIN, A. Open circuit voltage of organic solar cells: an in-depth review. *Energy Environ. Sci.*, v. 9, p. 391, 2016.

[39] BARTESAGHI, D. et al. Competition between recombination and extraction of free charges determines the fill factor of organic solar cells. *Nat. Commun.*, v. 6, p. 7083, 2015.

[40] SCHWARZ, C. et al. Role of the effective mass and interfacial dipoles on exciton dissociation in organic donor-acceptor solar cells. *Phys. Rev. B*, v. 87, p. 155205, 2013.

[41] YAO, Y. et al. Ultrafast long-range charge separation in organic photovoltaics: Promotion by off-diagonal vibronic couplings and entropy increase. *J. Phys. Chem. Lett.*, v. 7, p. 4830–4835, 2016.

[42] FEW, S. et al. Models of charge pair generation in organic solar cells. *Phys. Chem. Chem. Phys.*, v. 17, p. 2311–2325, 2015.

[43] D'AVINO, G. et al. Charge separation and recombination at polymer-fullerene heterojunctions: Delocalization and hybridization effects. *J. Phys. Chem. Lett.*, v. 7, p. 536–540, 2016.

[44] STREET, R. A. Electronic structure and properties of organic bulk-heterojunction interfaces. *Adv. Mater.*, v. 28, p. 3814–3830, 2016.

[45] ARKHIPOV, V. I. et al. Dopant-assisted charge carrier photogeneration in conjugated polymers. *Chem. Phys. Lett.*, v. 372, p. 886–892, 2003.

[46] ARKHIPOV, V. I. et al. Why is exciton dissociation so efficient at the interface between a conjugated polymer and an electron acceptor? *Appl. Phys. Lett.*, v. 82, p. 4604–4607, 2003.

[47] DAG, S.; WANG, L.-W. Packing structure of poly(3-hexylthiophene) crystal: Ab initio and molecular dynamics studies. *J. Phys. Chem. B*, v. 144, p. 5997–6000, 2010.

[48] MIGLIO, A. et al. Computed electronic and optical properties of SnO_2 under compressive stress. *Opt. Mater.*, v. 38, p. 161–166, 2014.

[49] DOU, M.; PERSSON, C. Comparative study of rutile and anatase SnO_2 and TiO_2: Band-edge structures, dielectric functions, and polaron effects. *J. Appl. Phys.*, v. 113, p. 083703, 2013.

[50] RIVATON, A. et al. Light-induced degradation of the active layer of polymer-based solar cells,. *Polym. Degrad. Stab.*, v. 95, p. 278–284, 2010.

[51] JOHNSON, B. H. et al. Influence of functionalized fullerene structure on polymer photovoltaic degradation. *Sol. Energ. Mater. Sol. Cells*, v. 94, p. 537–541, 2009.

[52] BETTIGNIES, R. de et al. Accelerated lifetime measurements of P3HT:PCBM solar cells. *Synth. Met.*, v. 156, p. 510–513, 2006.

[53] BERTHO, S. et al. Effect of temperature on the morphological and photovoltaic stability of bulk heterojunction polymer: fullerene solar cells. *Sol. Energy Mater. Sol. Cells*, v. 92, p. 753–760, 2008.

[54] KAWANO, K. et al. Degradation of organic solar cells due to air exposure. *Sol. Energy Mater. Sol. Cells*, v. 90, p. 3520–3530, 2006.

[55] SEEMANN, A. et al. Reversible and irreversible degradation of organic solar cell performance by oxygen. *Solar Energy*, v. 85, p. 1238–1249, 2011.

[56] REESE, M. O. et al. Consensus stability testing protocols for organic photovoltaic materials and devices. *Sol. Energy Mater. Sol. Cells*, v. 95, p. 1253–1267, 2011.

[57] PETERS, C. H. et al. The mechanism of burn-in loss in a high efficiency polymer solar cell. *Adv. Mater.*, v. 24, p. 663–668, 2012.

[58] PACIOS, R. et al. Effects of photo-oxidation on the performance of poly[2-methoxy-5-(3',7'-dimethyloctyloxy)-1,4-phenylene vinylene]:[6,6]-phenyl c61-butyric acid methyl ester solar cells. *Adv. Func. Mater.*, v. 16, p. 2117–2126, 2006.

[59] CÓRCOLESA, L. et al. Wavelength influence on the photodegradation of P3HT:PCBM organic solar cells. *Sol. Energy Mater. Sol. Cells*, v. 141, p. 423–428, 2015.

[60] KUMAR, P. et al. Comparing the degradation of organic photovoltaic devices under ISOS testing protocols. *Sol. Energy Mater. Sol. Cells*, v. 149, p. 179–186, 2016.

[61] HEUMUELLER, T. et al. Morphological and electrical control of fullerene dimerization determines organic photovoltaic stability. *Energy Environ. Sci.*, v. 9, p. 247–256, 2016.

[62] GROSSIORD, N. et al. Degradation mechanisms in organic photovoltaic devices. *Org. Electron.*, v. 13, p. 432–456, 2012.

[63] STREET, R. A. et al. Radiation induced recombination centers in organic solar cells. *Phys. Rev. B*, v. 85, p. 205211, 2012.

[64] BHATTACHARYA, J. et al. Photo-induced changes in fundamental properties of organic solar cells. *Appl. Phys. Lett.*, v. 100, p. 193501, 2012.

[65] DISTLER, A. et al. The effect of PCBM dimerization on the performance of bulk heterojunction solar cells. *Adv. Energy Mater.*, v. 4, p. 1300693, 2013.

[66] CLARKE, T. M. et al. Photodegradation in encapsulated silole-based polymer:PCBM solar cells investigated using transient absorption spectroscopy and charge extraction measurements. *Adv. Energy Mater.*, v. 3, p. 1473–1483, 2013.

[67] WANG, N. et al. Photodegradation of small-molecule organic photovoltaics. *Sol. Energ. Mat. Sol. Cells*, v. 125, p. 170–175, 2014.

[68] BURLINGAME, Q. et al. Photochemical origins of burn-in degradation in small molecular weight organic photovoltaic cells. *Energy Environ. Sci.*, v. 8, p. 1005–1010, 2015.

[69] TROST, S. et al. Overcoming the "light-soaking" issue in inverted organic solar cells by the use of Al:ZnO electron extraction layers. *Adv. Energy Mater.*, v. 3, p. 1437–1444, 2013.

[70] SUNDQVIST, A. et al. Origin of the S-shaped jv curve and the light-soaking issue in inverted organic solar cells. *Adv. Energy Mater.*, v. 6, p. 1502265, 2016.

5. ENHANCED EFFICIENCY OF BULK HETEROJUNTION ORGANIC SOLAR CELLS USING COBALT FERRITE NANOPARTICLES

Cobalt ferrite nanoparticles were synthesized by the proteic sol-gel method. Commercial $Fe(NO_3)_3\ 9H_2O$ (iron nitrate nonahydrate) and $Co(NO_3)_2\ 6H_2O$ (cobalt nitrate hexahydrate) powders were used as metal precursors in the production of the ferrite, whereas commercial gelatin (Gelita^{TM}) as organic precursor. Thermogravimetric analysis and differential scanning calorimetry were performed to investigate the thermal behavior of the precursor powders as well as to select the appropriate calcination temperatures for oxide formation. Several calcination temperatures were employed. Structural and magnetic properties of the synthesized materials were studied by X-ray diffraction, transmission Mössbauer microscopy and vibrating sample magnetometer. The results confirmed the formation of nanoparticles with cubic crystal structure (Fd3m) of cobalt ferrite and exhibited average crystallite size between 8 to 20 nm. It was found that their magnetic properties depend on the calcination temperature. These cobalt ferrite nanoparticles were successfully employed in organic solar cells. An investigation on the photovoltaic parameters of bulk heterojunction organic solar cells based on poly(3-hexylthiophene) and [6,6]-phenyl$_{C61}$-butyric acid methyl ester active layer doped with cobalt ferrite nanoparticles was performed. The optimization of the bulk heterojunction through the incorporation of cobalt ferrite nanoparticles resulted in an increased short-circuit current density and fill factor and as a result, enhanced power conversion efficiency.

5.1 Introduction

The power conversion efficiency (η) of organic solar cells (OSC) strongly depends on the phase morphology in the so-called bulk heterojunction (BHJ) [1, 2]. In this structure, two different semiconductors with the offset energy levels form nanometric domains in the bulk [3]. Experimental realization of this is a challenging task. The behavior of the organic semiconductors can be hardly predicted in terms of forming interpenetrating phase-separation in BHJ solar cells, and most of the recent records of η are directly associated with BHJ morphology improvement. Another way to improve OSC performance is to enlarge effective lifetime [4] by doping of the photoactive layer with oxide magnetic nanoparticles, thus attain efficient photogenerated charge carriers' collection [3, 5].

The inclusion of small heavy metal nanoparticles (NPs) in the active layer can have an effect on film morphology, donor-acceptor intermixing scales, and degree of crystallinity, as well as crystal orientation, which in the end has an impact on the conductivity and therefore on the performance of the final device. Thus, a complex interplay between these factors makes the prediction of a potential positive effect of the efficiency of OSCs very difficult. Moreover, a very large number of different small heavy metal NPs are available and could be added to OSCs [3–7].

As mentioned before in this thesis, conversion efficiency improvement has been achieved by introducing small amounts of magnetic NPs (such as spinel ferrites) in cells active layers [3–6].

In general, spinel ferrites are of a great interest in fundamental science, especially for addressing the fundamental relationship between magnetic properties and their crystal chemistry and structure [8, 9]. Technological applications of spinel cobalt ferrite ($CoFe_2O_4$) nanoparticles (NPs) include their potential use as ferrofluids [9], biological treatment agents [10] and photovoltaics cells [3] due to their unusual properties. In addition, $CoFe_2O_4$ possesses excellent chemical stability, good mechanical hardness, and a large positive first order crystalline anisotropy constant, making it a promising candidate for magneto-optical recording media [11].

Control on particle size and shape, ion distribution, and/or structure could allow a fine-tuning of the magnetic properties of ferrites [12]. In this regard, magnetic nanoparticles (MNPs) exhibit strong size-dependent properties that may provide valuable information on estimating the scaling limits of magnetic storage while contributing to the development of high-density data storage devices.

In this chapter, bulk heterostructure organic solar cells with proteic sol-gel $CoFe_2O_4$ NPs doping the active layer were studied. Structural, morphological and magnetic properties of NPs were investigated prior to cells construction. In order to discuss the influence of $CoFe_2O_4$ NPs on the performance of doped BHJ OSCs, we present a study based on the model system poly(3-hexylthiophene) (P3HT) and [6,6]-phenyl$_{C61}$-butyric acid methyl ester (PCBM) solar cells blended with weight concentration of 1 % of $CoFe_2O_4$ NPs.

$CoFe_2O_4$ NPs will be referred to throughout in this work when appropriate as CF.

5.2 Experimental procedure

5.2.1 $CoFe_2O_4$ nanoparticles

Nanoparticles synthesis was performed by proteic sol-gel method [13]. Commercial $Fe(NO_3)_3\ 9H_2O$ (iron nitrate nonahydrate) and $Co(NO_3)_2\ 6H_2O$ (cobalt nitrate hexahydrate) powders were used as metal precursors and commercial gelatin (Gelita^{TM}) as organic precursor. The proteic sol-gel method was used as follows: the gelatin was dispersed in distilled water under continuous stirring at room temperature until a uniform gel was obtained. The salts were dissolved in distilled water to make solutions of Co^{2+}/Fe^{3+} at a cobalt-to-iron molar ratio of 1:2. Each solution containing metal ions were added to the gel and maintained under continuous stirring at room temperature for 12 h. The substance formed by the mixture of the nitrates and gelatin was then dried at 150 °C for 12 h to remove excess of water resulting in a solid mass known as the precursor powder.

Thermogravimetric analysis (TG) and differential scanning calorimetry (DSC) were performed in the precursor powder in order to determine the temperature of formation of the oxides. Based on the TG/DSC results, Co^{2+}/Fe^{3+} precursor powder was calcined at 300 and 400 °C for 4 h, under air atmospheric conditions with a heating rate of 5 °C/min.

After calcination, the samples were immersed in H_2O_2 to remove the residual organic matter. Finally, the samples were washed with distilled water and dried at a temperature of 150 °C in air atmosphere for 12 h.

In order to evaluate the thermal stability and magnetic properties of the material produced, the sample calcined at 400 °C was submitted to a thermal treatment at 600 °C in air atmosphere for 2 h. Samples calcined at 300, 400 °C and treated at 600 °C are referred to throughout this work as 300, 400 and TT600, respectively. Samples were characterized by X-ray diffraction, Mössbauer spectroscopy and vibration sample magnetometry.

TGA and DSC were simultaneously performed using a NETZSCH STA 449F3 Jupiter thermal analysis equipment. Measurements were performed under air synthetic flow with heating hate of 5 °C/min.

X-ray diffraction (XRD) patterns of powdered nanoparticles were collected at room temperature using a X-Pert PRO MPD Panalytical diffractometer operating with a Kα-Co source (λ = 1.788 Å) at 40 kV and 40 mA. The data were collected in a range of 10 °–100 ° in 2θ and the pattens were Rietveld refined using the program GSAS [14].

Magnetization measurements of powdered nanoparticles were carried out at room temperature using a Microsense EV9 model vibrating sample magnetometer (VSM) with maximum field of 21 kOe. Room temperature Mössbauer spectra were measured in transmission mode using a ^{57}Co(Rh) radioactive source mounted on a velocity driver operating in sinusoidal mode. The data were evaluated by least square fitting to series of discrete Lorentzian shaped subspectra by means of the software package Normos. Isomer shifts (δ) are quoted with respect to α-Fe.

5.2.2 Active layer

P3HT:PCBM and P3HT:CF:PCBM film samples were produced with the purpose of to evaluate their morphology and optical and electrical properties. The blends were prepared via spin coating on a glass transparent substrate ITO. Films were characterized by atomic force microscopy (AFM), conductive atomic force microscopy (C-AFM) and ultraviolet-visible spectroscopy (UV-vis).

AFM and C-AFM measurements were performed in air under ambient conditions using a Asylum Research scanning probe microscope. Images were collected in tapping mode using a Nanoworld (model Arrow CONTPt) Pt-coated Si probe with a spring constant of 0.2 N/m. UV-vis spectroscopy was carried out at room temperature using a UV 2600 Shimadzu spectrophotometer coupled to an integrating sphere ISR 2600 Plus.

5.2.3 Solar cell fabrication

Two types of solar cell devices were prepared with inverted configuration and tested in air under ambient conditions: reference devices (ref-OSC) with configuration ITO/Ag/ITO/ETL/P3HT:PCBM/PEDOT:PSS/Ag and nanoparticle-bearing devices (CF-OSC) with configuration ITO/Ag/ITO/ETL/P3HT:CF:PCBM/PEDOT:PSS/Ag (see Fig. 5.1). In this research work the CF used were those obtained by the calcination process at 400 °C. The devices were built with an area of 0.55 cm^2.

Figure 5.1: Schematic overview of the manufactured devices.

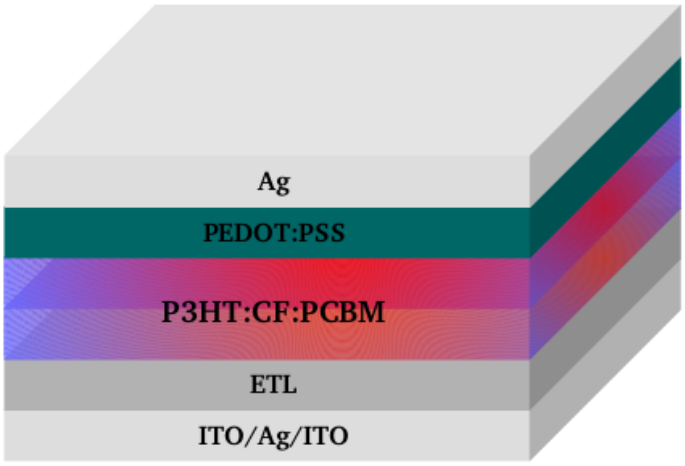

Source: Own author.

The flexible substrate is composed of a sheet of polyethylene (PET) coated with an indium-doped tin oxide/silver/indium-doped tin oxide (ITO/Ag/ITO) multilayer (10 Ω/□),

which is called IMI. The layers are very thin to provide transparency, conductivity and flexibility. A 8 nm thick electron transport layer (ETL) was deposited by blade coating (for reasons of confidentiality this material will not be described in this work).

The bulk heterojunction blend of ref-OSCs was comprised of a 1:0.8 molar mixture of P3HT:PCBM dispersed in o-xylene:tetralin (7:1) while that of CF-OSC was comprised of a molar 0.99:0.01:08 mixture of P3HT:CF:PCBM. The nanoparticles were suspended in o-xylene:tetralin (1 mg/ml) and mixed to the P3HT:PCBM blend to achieve the desired concentration. Blends were blade coated to deposit a 200 nm-thick P3HT:PCBM and P3HT:CF:PCBM films.

A 100-nm thick poly(3,4-ethylenedioxythiophene)-poly(styrenesulfonate) (PEDOT:PSS) hole transport layer (HTL) was deposited without any treatment. Finally, a 100 nm-thick Ag back metal electrode was deposited by thermal evaporation. A set of ten ref-OSC and CF-OSC devices were prepared for the tests of efficiency.

Solar simulations were performed on a Wacon WXS-156S-10 model equipped with an AM1.5 filter (100 mW/cm^2, AM1.5G). A calibrated Si/BK7 photodiode from PV measurements was also applied for calibration before each measurement.

5.3 Results and discussion

5.3.1 $CoFe_2O_4$ nanoparticles

Thermal analysis was performed in order to study the thermal decomposition of the materials and to select the appropriate temperatures of cobalt ferrite formation. Figure 5.2 shows TGA/DSC curves obtained from the precursor powder and $CoFe_2O_4$ samples calcined at 300, 400 °C before and after thermal treatment.

The thermal behavior of the precursor powder may be divided into two stages as indicated in Fig. 5.2a. The first thermal event at a temperature below 190 °C is attributed to the loss of water molecules. The second one occurs in the 190–320 °C range and can be attributed to the thermal degradation of gelatin chains. This reaction is characterized by an exothermic peak at about 280 °C in the DSC scan and is responsible for the loss of about 23 % of the sample mass. In this stage formation and crystallization of

corresponding metal oxides take place. This result is in agreement with those obtained in other works [8, 15]. From the thermal analysis of the samples 300, 400 and TT600, the DSC shows no endo or exothermic processes and the TGA shows no mass loss, confirming that all organic matter has been eliminated during the calcination process.

Figure 5.2: TG/DSC curves from Co^{2+}/Fe^{3+} precursor powders, 300, 400 and TT600 samples.

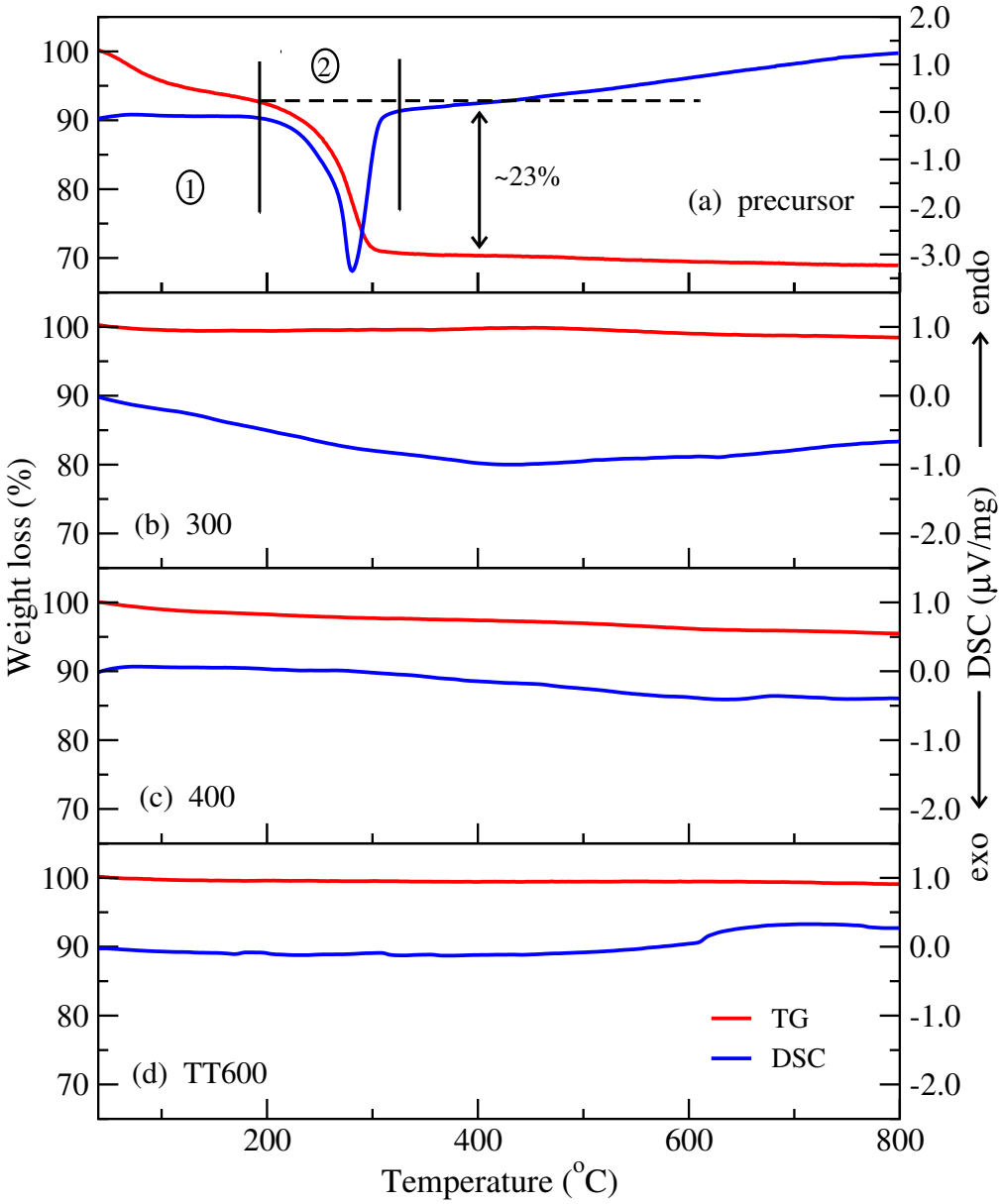

Source: Own author.

Figure 5.3 shows X-ray diffraction patterns of $CoFe_2O_4$ samples. All diffractograms show peaks that match the ICSD-84611 reference pattern relative to the cubic crystal structure (Fd3m) of $CoFe_2O_4$ (bars in the figure). No other crystalline phase was found.

Figure 5.3: X-ray diffraction patterns of $CoFe_2O_4$ samples. Dots and solid lines are the experimental data and best fit respectively. Bars represent the ICSD-64811 standard pattern.

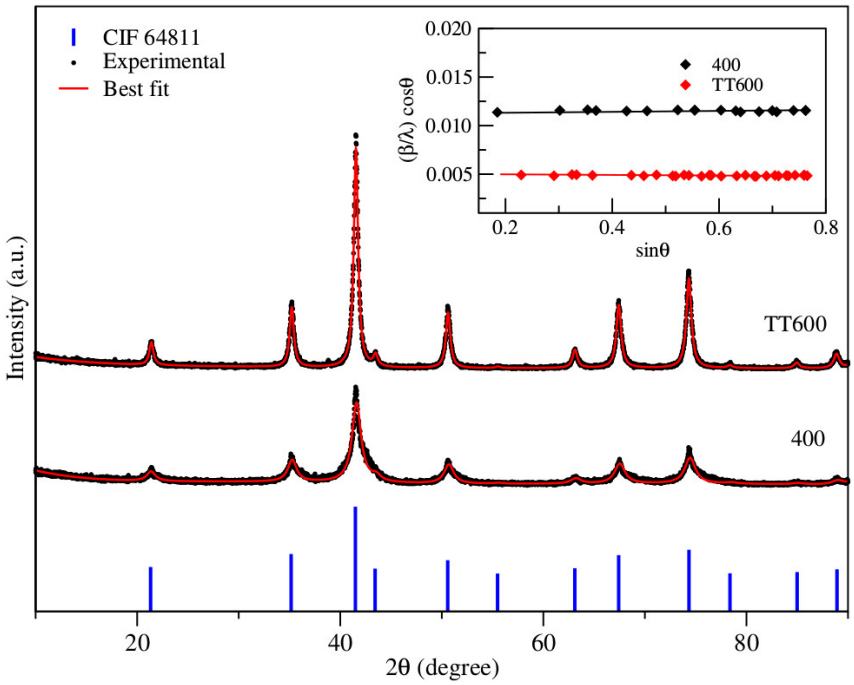

Source: Own author.

The patterns were Rietveld refined and the best fits are shown as solid red lines. Williamson-Hall curves [16] are shown in the inset of Fig. 5.3. Table 5.1 shows lattice parameter, unit cell volume, and crystallite average size as calculated by the Scherrer formula (D_S) and corrected by the Williamson-Hall method (D_{WH}) after compensating for residual microstrain (ϵ). Lattice parameters are virtually the same for all samples. All samples showed crystallite size in the nanometer range (6 to 20 nm) with negligible levels of microstrain. The thermal treatment led to an increase of particle size from 8.7 (sample 400) to about 20 nm (sample TT600). However, the homogeneity of the material was conserved with thermal treatment evidenced by straight Williamson-Hall curves.

Table 5.1: Lattice parameters, unit cell volume, average crystallite size and microstrain of $CoFe_2O_4$ samples 400 and TT600.

Temp. (°C)	$a = b = c$ (Å)	V (Å^3)	D_S (nm)	D_{WH} (nm)	ϵ (%)
400	8.378	588.2	5.78	8.7	0.0009
TT600	8.383	589.2	13.4	20	-0.045

Source: Own author.

Figure 5.4 shows room temperature Mössbauer of the nanoparticles samples 300, 400 and TT600 while Table 5.2 shows hyperfine parameters obtained from best fits to the date. Spectra of samples 300 and 400 show a superposition of a sextet and a doublet, while that of sample TT600 shows only the sextet. Doublets were fitted with a crystalline site while sextets were fitted with hyperfine magnetic field distributions.

The appearance of a doublet in addition to the expected sextet pattern [12, 17, 18] in the spectra of samples 300 and 400 suggests that presence of superparamagnetic and ferrimagnetic interactions in these samples. Superparamagnetism is characteristic of small crystallites, wherein, the magnetization is not fixed in any of the easy axes. It is a consequence of fluctuating magnetic spins about the easy axes of magnetization in the absence of a magnetic field [12]. The doublet is absent from the spectrum of sample TT600 due to its larges average crystallite size. An increase in crystallite size cause a reduction of magnetic spins fluctuating, thereby an easy axes of magnetization is produced.

Table 5.2: Hiperfine parameters obtained from fits to Mössbauer spectra of samples $CoFe_2O_4$ samples. The hiperfine parameters are: δ–isomer shift; δ–quadrupole splitting; Bhf–average hyperfine magnetic field. δ and Δ in mm/s, Bhf in T and area in %. Uncentainties of δ and Δ values smaller than 0.005 mm/s, Bhf value smaller than 0.5 T and of area value smaller than 0.05 %.

sample	sextet				doublet			
	δ	Δ	Bhf	area	δ	Δ	Bhf	area
300	0.31	0.033	50.0	68.4	0.33	0.72	**	31.6
400	0.31	0.014	49.0	67.0	0.33	0.78	**	33.0
TT600	0.30	0.016	48.0	100.0	**	**	**	**

Source: Own author.

Figure 5.4: Mössbauer spectrum of $CoFe_2O_4$ samples.

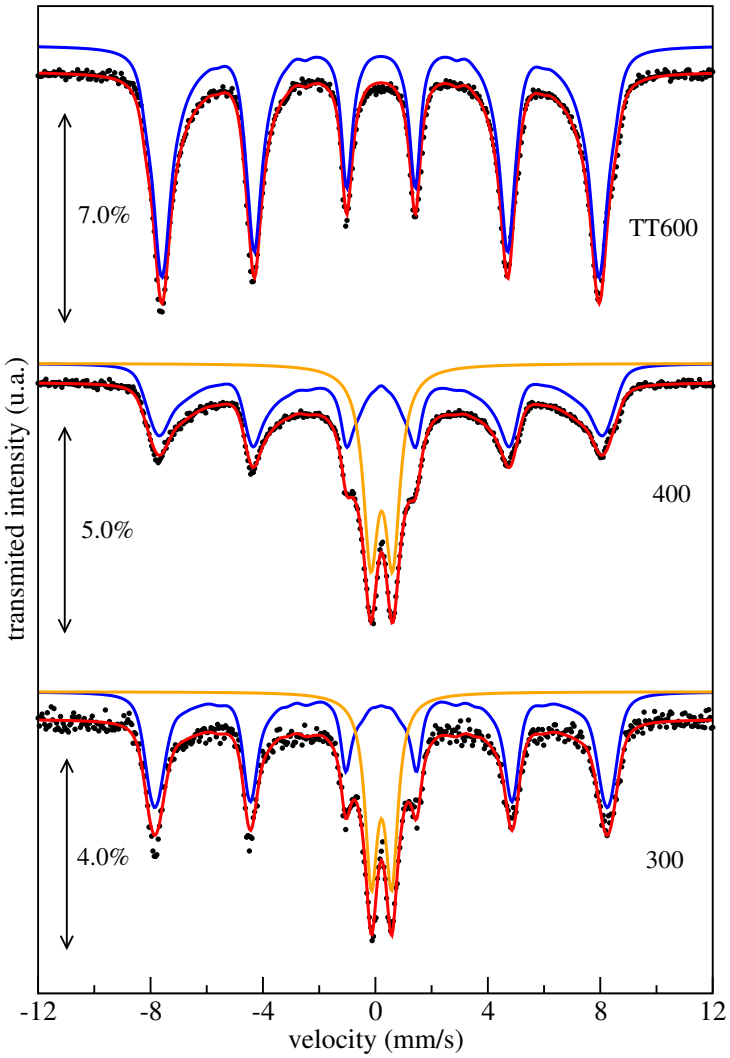

Source: Own author

It is known that the blocking temperature of the ferromagnetic interactions is proportional to the particle size [12, 18]. Therefore, reduction of particle size, and consequently the reduction of the ferromagnetic blocking temperature, implies in the weakening of the ferromagnetic interactions causing a broadening in the sextet lines and also a reduction in the hyperfine magnetic field. Further reduction of the particle size, leading to the limit of blocking the ferromagnetic interactions, causes a collapse in the sextet therefore forming a broad lined singlet. Particles with size below the blocking limit give rise to a superparamagnetic doublet [17].

In nanostructured magnetic materials, interactions between nanoparticles often play an important role. Long-range magnetic dipole interactions can have a strong influence on

the magnetic dynamics in samples containing ferromagnetic or ferrimagnetic nanoparticles [19]. Magnetic properties of magnetic nanoparticles such as remanent magnetization (M_r), saturation magnetization (M_s), squareness (M_r/M_s) and coercive field (H_c) are affected by cationic distribution in the sites, surface area and density. Moreover, the strength of interactions between nanoparticles is very sensitive to the method of sample preparation.

Hysteresis loops taken at room temperature for all samples $CoFe_2O_4$ are shown in the Fig. 5.5 while the corresponding magnetic parameters are reported in Table 5.3. All samples exhibited a typical ferromagnetic behavior at room temperature. It can be observed an increase in M_s and a decrease in H_c for the thermally treated sample (TT600) when compared to samples without thermal treatment. Comparing the samples 300 and 400, the saturation magnetization values of the calcined samples increases with increasing particle size, which may be attributed to the surface effects in these nanoparticles. But the values of the H_c have no similar effect.

Figure 5.5: Room temperature hysteresis loop of a $CoFe_2O_4$ samples.

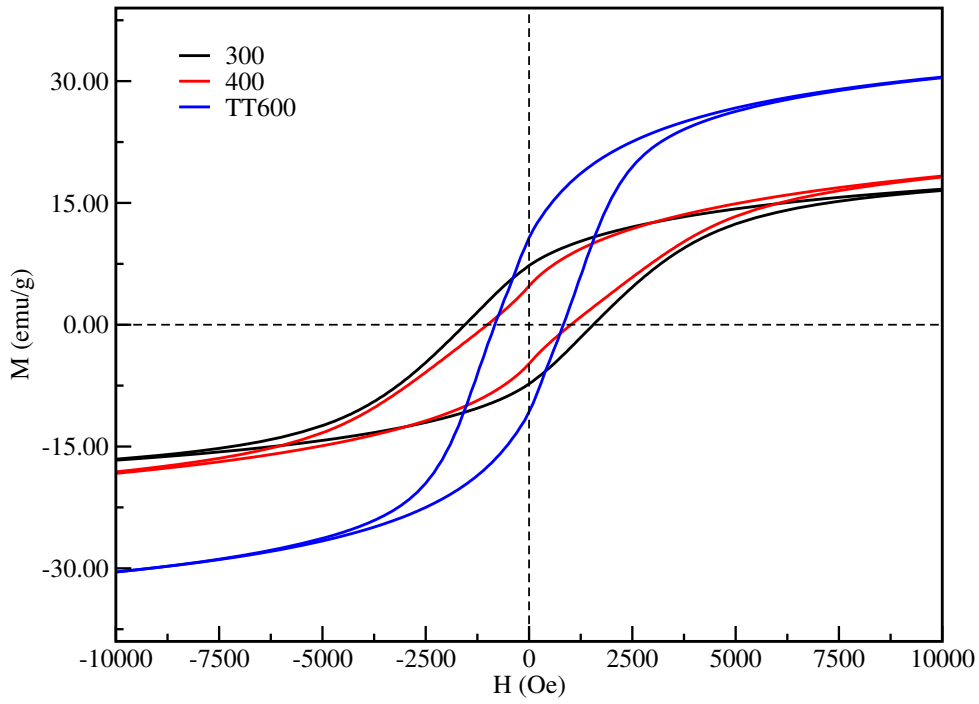

Source: Own author.

The magnetic interactions in nanoparticles are unstable and disordered, thus the magnetic moment cannot be easily kept to be consistent with the external field. Furthermore, the surface of the nanoparticles seems to be composed of some distorted or slanted spins that repel the core spins to align the field direction. Consequently, the saturation magnetization increases for larger sizes and decrease for smaller sizes [20]. The variation in the value of the H_c with particle size can be explained on the basis of domain structure, critical size, and the anisotropy of the crystal [21]

Table 5.3: Magnetic properties values of $CoFe_2O_4$ samples.

sample	H_c (Oe)	M_r (emu/g)	M_s (emu/g)	M_r/M_s
300	1552	7.30	18.90	0.386
400	1012	4.80	21.60	0.222
TT600	830	10.67	33.30	0.320

Source: Own author.

5.3.2 Films characterization

Figure 5.6 shows UV-vis absorption spectra of the P3HT:PCBM blend (ref-OSC film) and doping with 1 % and 2 % of $CoFe_2O_4$ NPs (CF-OSC films). In both cases it was observed that doping of the P3HT:TCBM active layer did not significantly affect the absorption spectra.

Figure 5.7 shows AFM morphology and height images as well as C-AFM current images of the active layer of a ref-OSC and a CF-OSC film. It can be observed on the AFM surface topography images – parts (a), (b), (d) and (e) – that the addition of nanoparticles in this ratio do not affect the morphology and homogeneity of the film, suggesting that the nanoparticles are homogeneously distributed within the film, without the formation of agglomerates.

Current AFM images – parts (c) and (f) – was used to examine conductivity variations in the P3HT:PCBM pristine and doped blends. A high work function Pt-coated Si probe

was used in all measurements. The high electron injection barrier between the Pt-coated Si tip and the P3HT:PCBM blend blocks electron injection which allows hole transport only within P3HT [22, 23]. Therefore, bright and dark regions are attributed to P3HT-rich and PCBM-rich domains, respectively. In both cases, it was observed a homogeneous distribution in the current images, suggesting that the nanoparticles are not contributing significantly to eventual variations of currents through the active layer.

Figure 5.6: UV–Vis absorbance spectra of ref-OSC and CF-OSC films.

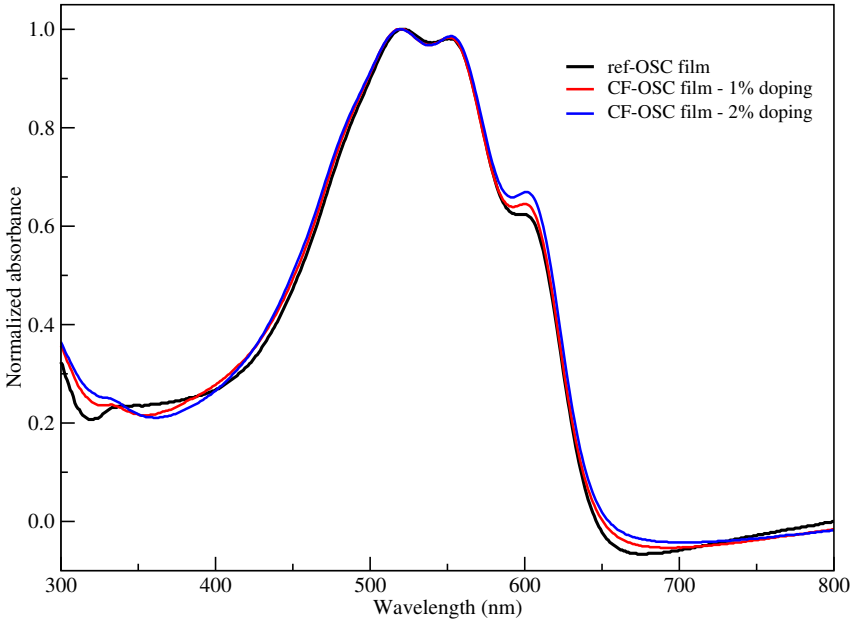

Source: Own author

Figure 5.7: (a) AFM morphology image, (b) height images of the surface morphology and (c) C-AFM current images of a ref-OSC film; (d) AFM morphology image, (e) height images of the surface morphology and (f) C-AFM current images of a CF-OSC film.

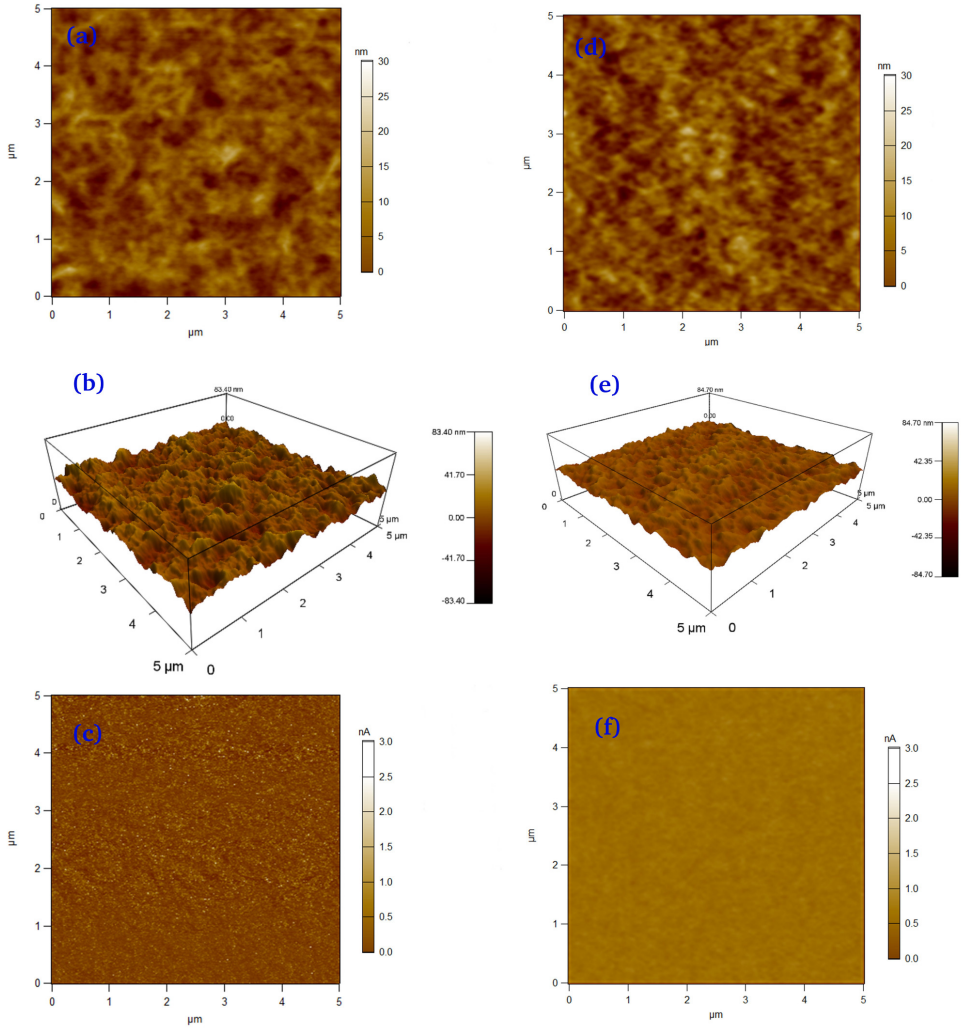

Source: Own author

5.3.3 Solar cell characterization

Figure 5.8 shows a typical $J \times V$ curve for ref-OSC and CF-OSC cells with the best performance. The photovoltaic parameters and resistances values of each set of cells are summarized in Table 5.4. It can be seen that the photovoltaic parameters of the cells were very close to the average values of each set of devices, ensuring good reproducibility of the results. The values for the best devices, as well as the average values to each set of devices are plotted in the Fig. 5.9.

With the exception of V_{oc}, cell with doped active layers presented a slight, albeit noteworthy, improvement of η, J_{sc} and FF values when compared to reference devices.

Moreover, it was observed a slight decrease in the values of the R_s and an increase in the values of the R_{sh}.

Figure 5.8: J×V curves of the best ref-OSC and CF-OSC cells. Under simulated AM 1.5 solar illumination at 100 mW/cm^2.

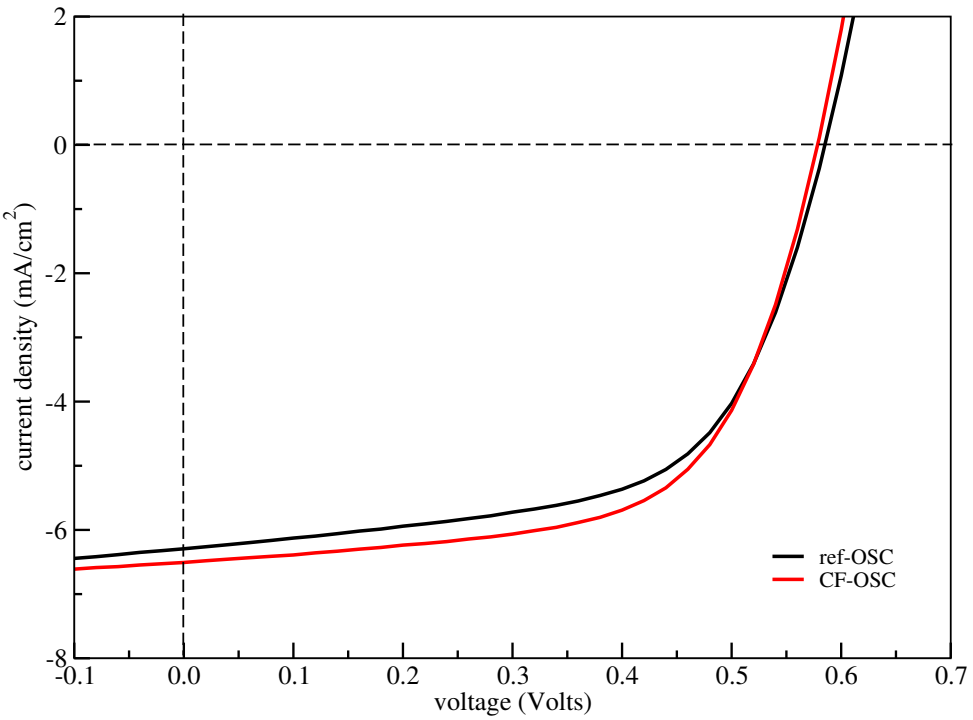

Source: Own author

For BHJ of an organic photovoltaic device, V_{oc} mainly depends on the energy difference between the lowest unoccupied molecular orbital of acceptor and the highest occupied molecular orbital of the donor [24]. A slight blending of CF is not likely to change the energy level distribution of the organic BHJ and hence the virtually unchanged V_{oc}.

The devices reinforced with CF showed a slightly improved J_{sc} with average value increasing from 5.80 to 6.12 mA/cm^2. This suggests that the addition of CF contributes to the dissociation of photogenerated excitons into free charge carriers resulting in an enlarged short-circuit current density.

Figure 5.9: Comparison of best and average values of photovoltaic parameters and resistances for each set of devices.

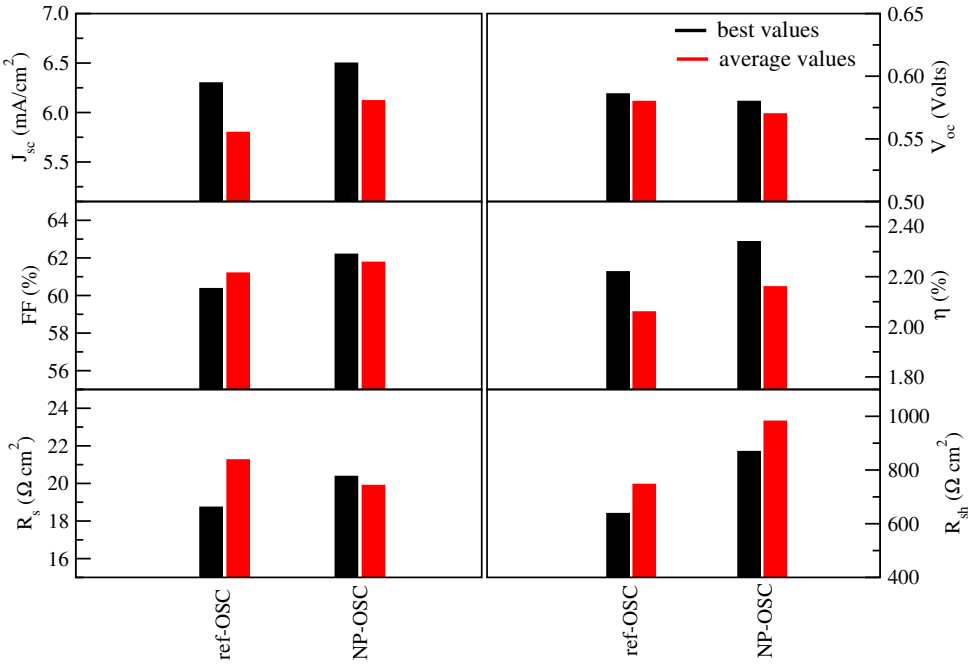

Source: Own author

The FF is a critical parameter that can reflect dynamic transport of the photocurrent in organic solar cells. On this regard, much effort has been done to investigate the fundamental Physics behind the FF [25–27]. For example, it was reported that the FF is mainly determined by the quality of the polymer-cathode interface, while the space charge effect is only secondary in organic solar cells [27]. However, there are reports that the imbalance of electron and hole mobilities plays an important role on controlling the FF [28] and the charge recombination processes at high light intensities for organic solar cells can limit the FF and the power conversion efficiency [26].

In a simple equivalent circuit model, it is pointed out that the FF is determined by both series and parallel resistances [29]. However, under device-operating condition, the series and parallel resistances become a function of bulk and interfacial transport of photogenerated carriers. Clearly, understanding the effects of dynamic transport on the FF is an important issue to optimize the device performance [26].

Therefore, in addition to the increase in the J_{sc}, the addition of CF to the active layer of CSOs can generate mechanisms that provide an improvement in the collection

of photogenerated charge carriers. This is evidenced by the improvement of the FF, reduction of the R_s and increase of the R_{sh}. These parameters were responsible for the improved performance of the CF-bearing device.

One of the possible explanations to the improvement of η can be associated with the presence of a coercive electric field produced by the interactions between CF, which could assist the built-in electric field in the collection of the charge carriers [5, 7, 30]. Another possible explanation is based on spin-orbit coupling which increases the efficiency of the exciton intersystem crossing process in the device, and thus extends exciton lifetime [3, 4, 6].

Table 5.4: Photovoltaic parameters and resistance values of ref-OSC and CF-OSC devices.

Device	J_{sc} (mA/cm^2)	V_{oc} (V)	FF (%)	η (%)	R_s (Ω cm^2)	R_{sh} (Ω cm^2)
			ref-OSC			
D1	5.88	0.580	62.50	2.13	21.88	953.50
D2	5.68	0.570	62.12	2.02	21.56	950.70
D3	5.55	0.570	61.78	1.95	21.37	962.40
D4	5.50	0.579	61.62	1.96	23.47	798.70
D5	5.76	0.576	61.33	2.03	22.16	857.00
D6	6.30	0.586	60.37	2.22	18.74	638.40
D7	5.87	0.585	60.36	2.07	19.48	703.20
D8	5.65	0.587	61.41	2.04	20.92	782.60
D9	5.93	0.588	60.16	2.09	19.67	628.80
D10	5.94	0.579	60.36	2.08	23.34	767.80
avg	**5.80±0.23**	**0.58±0.01**	**61.20±0.83**	**2.06±0.08**	**21.26±1.6**	**747±125**
			CF-OSC			
D1	6.08	0.578	62.30	2.20	21.35	928.30
D2	6.50	0.580	62.20	2.34	20.38	869.30
D3	6.30	0.576	62.06	2.25	20.72	1057.40
D4	6.00	0.570	58.85	2.00	21.13	702.00
D5	6.81	0.572	61.94	2.06	21.30	994.00
D6	6.29	0.568	62.20	2.22	18.80	1104.00
D7	6.07	0.567	62.71	2.15	18.96	1154.00
D8	6.40	0.567	62.15	2.25	18.17	971.30
D9	5.93	0.566	61.32	2.06	19.87	1077.40
D9	5.88	0.562	61.95	2.05	18.36	962.70
avg	**6.12±0.23**	**0.57±0.01**	**61.77±1.0**	**2.16±0.11**	**19.9±1.2**	**982±130**

Source: Own author

5.4 Conclusion

Thermal analysis suggested $CoFe_2O_4$ formation at temperatures between 190–320 °C. XRD results for all samples showed the presence of a single cubic $CoFe_2O_4$ nanostructured phase (crystallite size in the range 8 to 20 nm with negligible levels of microstrain). Mössbauer spectroscopy and magnetic measurements showed that $CoFe_2O_4$ nanoparticles with lower average crystallite sizes (calcined at temperatures of 300 and 400 °C) it is composed of superparamagnetic and ferromagnetic nanoparticles at room temperature. Bulk heterojunction organic solar cells were built doping the P3HT:PCBM active layer with 1 wt. % of CF. Devices without CF in the active layer were also produced to serve as reference.

OSCs doped with CF showed an improvement of the photovoltaic parameters J_{sc} and FF in relation to the reference devices. The increase in these parameters contributed significantly to the increase in η. The results obtained in this research work represents an evolution in the production of nanoparticles by an alternative sol-gel process and provide subsidies that propitiate an understanding of the effective action caused by the doping of the active layer of OSCs with CF, thus opening new improvement opportunities by means of the addition of a degree of freedom for spin within the active layer. The features shown by the CF-doped devices offer advantages, therefore, the present work represents an evolution as it showed further evidence that addition of magnetic nanoparticles to bulk heterojunction organic solar cells is a promising path to enhanced power conversion efficiency.

5.5 References

[1] BLOKING, J. T. et al. Comparing the device physics and morphology of polymer solar cells employing fullerenes and non-fullerene acceptors. *Adv. Energy Mater.*, v. 4, p. 1301426, 2014.

[2] HUANG, J. et al. Highly efficient organic solar cells with improved vertical donor–acceptor compositional gradient via an inverted off-center spinning method. *Adv.*

Mater., v. 28, p. 967, 2016.

[3] KOVALENKO, A. et al. Towards improved efficiency of bulk-heterojunction solar cells using various spinel ferrite magnetic nanoparticles. *Organic Electronics*, v. 39, p. 118–126, 2016.

[4] GONZÁLEZ, D. M. et al. Improved power conversion efficiency of P3HT:PCBM organic solar cells by strong spin-orbit coupling-induced delayed fluorescence. *Adv. Energy Mater.*, v. 5, p. 1401770, 2015.

[5] WANG, K. et al. Effects of magnetic nanoparticles and external magnetostatic field on the bulk heterojunction polymer solar cells. *Scientific Reports*, v. 5, p. 9265, 2015.

[6] PEREIRA, M. S. et al. Application of Fe-doped SnO_2 nanoparticles in organic solar cells with enhanced stability. *Opt. Mater.*, v. 64, p. 548–556, 2017.

[7] GONG, X. et al. Investigation of the magnetic nickel nanoparticle on performance improvement of P3HT:PCBM solar cell. *Appl. Phys. A*, v. 122, p. 287, 2016.

[8] HAJALILOU, A. et al. Fabrication of spherical $CoFe_2O_4$ nanoparticles via sol–gel and hydrothermal methods and investigation of their magnetorheological characteristics. *RSC Adv.*, v. 6, p. 89510, 2016.

[9] KAMALI, S. et al. Magnetization and stability study of a cobalt-ferrite-based ferrofluid. *J. Magn.Magn. Mater.*, v. 404, p. 143–147, 2016.

[10] KANAGESAN, S. et al. Synthesis, characterization and in vitro evaluation of manganese ferrite ($MnFe_2O_4$) nanoparticles for their biocompatibility with murine breast cancer cells (4T1). *Molecules*, v. 21, p. 312, 2016.

[11] ROYER, F. et al. Trends in colloid and interface science XVII: Progress in colloid and polymer science. In: _____. [S.l.]: Springer Berlin Heidelberg, 2004. v. 126, cap. Magneto-optical properties of $CoFe_2O_4$ ferrofluids. Influence of the nanoparticle size distribution, p. 155–158.

[12] RAJENDRAN, M. et al. Magnetic properties of nanocrystalline $CoFe_2O_4$ powders prepared at room temperature: variation with crystallite size. *J. Magn. Magn. Mater.*, v. 232, p. 71–83, 2001.

[13] MENESES, C. T. et al. A simple route to the synthesis of high-quality NiO nanoparticles. *J. Nano. Res.*, v. 9, p. 501–505, 2007.

[14] TOBY, B. H. EXPGUI, a graphical user interface for GSAS. *J. Appl. Crystallogr.*, v. 34, p. 210, 2001.

[15] SINGH, R. K. et al. Thermal, structural, magnetic and photoluminescence studies on cobalt ferrite nanoparticles obtained by citrate precursor method. *J. Therm. Anal. Calorim.*, v. 110, p. 573–580, 2012.

[16] WILLIAMSON, G. K.; HALL, W. H. X-ray line broadening from filed aluminium and wolfram. *Acta Metallurgica*, v. 1, p. 22, 1953.

[17] NOGUEIRA, N. A. S. et al. X-ray diffraction and mossbauer studies on superparamagnetic nickel ferrite ($NiFe_2O_4$) obtained by the proteic sol-gel method. *Mater. Chem. Phys.*, v. 163, p. 402–406, 2015.

[18] BABIĆ-STOJIĆ, B. et al. Magnetic and structural studies of $CoFe_2O_4$ nanoparticles suspended in an organic liquid. *J. Nanomater.*, v. 2013, p. 9 pages, 2013.

[19] MORUP, S. et al. Magnetic interactions between nanoparticles. *Beilstein J. Nanotechnol.*, v. 1, p. 182–190, 2010.

[20] NASERI, M. G. et al. Simple synthesis and characterization of cobalt ferrite nanoparticles by a thermal treatment method. *J. Nanomater.*, v. 2010, p. 8 pages, 2010.

[21] QU, Y. et al. The effect of reaction temperature on the particle size, structure and magnetic properties of coprecipitated $CoFe_2O_4$ nanoparticles. *Mater. Lett.*, v. 60, p. 3548–3552, 2006.

[22] CHEN, F. C. et al. Morphological study of P3HT:PCBM blend films prepared through solvent annealing for solar cell applications. *Solar Energy Materials & Solar Cells*, v. 94, p. 2426–2430, 2010.

[23] DANTE, M. et al. Nanoscale charge transport and internal structure of bulk heterojunction conjugated polymer/fullerene solar cells by scanning probe microscopy. *J. Phys. Chem. C*, v. 112, p. 7241 – 7249, 2008.

[24] GUO, X. et al. Polymer solar cells with enhanced fill factors. *Nature Photonics*, v. 7, p. 825, 2013.

[25] BARTESAGHI, D. et al. Competition between recombination and extraction of free charges determines the fill factor of organic solar cells. *Nat. Commun.*, v. 6, p. 7083, 2015.

[26] WU, L. et al. Origin of the fill factor loss in bulk-heterojunction organic solar cells. *Appl. Phys. Lett.*, v. 104, p. 153903, 2014.

[27] GUPTA, D. et al. Fill factor in organic solar cells. *Sol. Energy Mater. Sol. Cells*, v. 94, p. 1309–1313, 2010.

[28] TRESS, W. et al. Correlation of absorption profile and fill factor in organic solar cells: The role of mobility imbalance. *Adv. Energy Mater.*, v. 3, p. 631–638, 2013.

[29] QI, B.; WANG, J. Fill factor in organic solar cells. *Phys. Chem. Chem. Phys.*, v. 15, p. 8972, 2013.

[30] ZHANG, W. et al. Fe_3O_4 nanoparticles induced magnetic field effect on efficiency enhancement P3HT:PCBM bulk heterojunction polymer solar cells. *Sol. Energ. Mat. Sol. C.*, v. 95, p. 2880, 2011.

6. CONCLUSIONS AND FUTURE WORK

This work explored the production and characterization of nanostructured semiconductor oxides SnO_2, Fe/SnO_2 and $CoFe_2O_2$ by the low-cost methods proteic sol-gel and mechanical alloying as well as their application in third generation solar cells.

6.1 Conclusions

SnO_2, $CoFe_2O_2$ and Fe/SnO_2 nanoparticles were successfully synthesized using proteic sol-gel and mechanical alloying. Nanostructured SnO_2 was successfully applied as photoanode in DSSCs, while $CoFe_2O_2$ and Fe/SnO_2 was successfully applied as reinforcement of the active layer in OSCs.

SnO_2 nanoparticles showed the presence of a single rutile SnO_2 nanostructured phase (crystallite size in the range 8 to 20 nm). Furthermore, thermal treatment of these samples showed that this material has high thermal stability. Their transparency to visible light points to a promising material to be used as photoaned in DSSCs. DSSCs built with this material presented photovoltaic parameters consistent with results obtained from similar cells and reported in the literature. The present work represents an evolution in the production of nanoparticles by an alternative sol-gel process and represents a promising path to applications in emerging technologies.

Fe/SnO_2 nanoparticles showed only peaks correspond to the rutile-type tetragonal structure of SnO_2. Magnetic measurements indicated that the sample is ferromagnetic at room temperature. Bulk heterojunction organic solar cells were built doping the P3HT:PCBM active layer with 10 wt.% of SnO_2 magnetic nanoparticles. Devices constructed with the addition of Fe/SnO_2 in active layer showed an improvement in some photovoltaic parameters. Improved J_{sc}, together with a broader IPCE spectrum, suggests that addition of NPs to the devices contributed to the dissociation of photogenerated

excitons into free charge carriers. The increase of dissociated charge carriers is attributed to the presence of a week effective magnetic field in the active layer. Doping of the active layer of OSCs with magnetic nanoparticles has been successfully used to modify the cells' electrical and optical properties. Another relevant parameter in OSCs is the stability and lifetime of the devices. Stability studies revealed that doping of the active layer of OSCs have been contributed to an improvement in stability.

$CoFe_2O_4$ NPs showed the presence of a single cubic $CoFe_2O_4$ nanostructured phase (crystallite size in the range 8 to 20 nm). Mössbauer and magnetic measurements revealed that this material exhibits ferromagnetic and paramagnetic behavior at room temperature. Bulk heterojunction organic solar cells were built doping the P3HT:PCBM active layer with 1 wt.% of $CoFe_2O_4$ NPs. OSCs doped with NPs showed an improvement of the photovoltaic parameters J_{sc} and FF in relation to the reference devices. The increase in these parameters contributed significantly to the increase in η. The results obtained until now in this research work provide subsidies that reinforce the success in the investment of the application of magnetic nanoparticles to bulk heterojunction organic solar cells as to be a promising path to enhanced power conversion efficiency.

6.2 Future work

This is a work still in process of development, mainly in relation to the application of magnetic nanoparticles in CSOs. It has potential to be explored on several fronts as such:

- an in-depth study on the role of NPs in the generation, dissociation and collection of charge carriers in OSCs, and consequently the improvement observed in the photovoltaic parameters;
- to evaluate the stability of OSCs doped with $CoFe_2O_4$ NPs with respect to the stability of the reference devices;
- to perform tests using magnetic nanoparticles that exhibit magnetic behavior different of those used in this work;

- to broaden the application of magnetic nanoparticles in OSCs with different materials composing the interfacial layers of the device.